Ministry of Higher Education and Scientific research

Al-Iraqia University

Engineering College

Electrical Engineering Department

Drone Based Thermal Inspection of Power Transmission Lines

A Project Submitted to the Department of Electrical Engineering in Partial Fulfilment for the Requirements of the Degree of B.Sc. in Electrical Engineering

BY

Hussein Faris Saeed

Ahmed Riyadh Maatoq

Zulfiqar Ahmed Mzhr

Mustafa Karim Lazim

SUPERVISOR

Asst. Prof. Dr. Baraa Munqith Albaker

2022-2023

DECLARATION

We hereby declare that this project report is based on our original work except for citations and quotations, which have been duly acknowledged.

Signature :	_____	Signature	: _____
Name :	_____	Name	:_____
Date :	_____	Date	: _____

Signature :	_____	Signature:	_____
Name :	_____	Name :	_____
Date :	_____	Date :	_____

APPROVAL FOR SUBMISSION

I certify that this project report entitled **"Drone Based Thermal Inspection of Power Transmission Lines"** was prepared by "**Hussein Faris Saeed, Ahmed Riyadh Maatoq, Zulfiqar Ahmed Mzhr, and Mustafa Karim Lazim"** has met the required standard for submission in partial fulfilment of the requirements for the award of Bachelor of **Electrical Engineering** at Al-Iraqia University .

Approved by,

Signature : _____

Supervisor : Asst. Prof. Dr. Baraa Munqith Albaker

Date : _____

Specially dedicated to my family

Life is a journey filled with lots of backroads, pit stops and destinations along the way. The one thing that never changes in our journey, and we can always count on, is our families. They are always here with us. They love us unconditionally and they never judge us for who we are or the choices we make, and they always, always support whatever it is we are doing in life, even if it is not what they'd prefer for us or themselves.

Our families have showed us what the true meaning of life really is and what makes the journey worth it in the end.

Thank you for being our rock, inspiration, biggest support system and our number one fans. We can't wait to see where the road takes us next, hand in hand, moving forward together. We love you guys, forever and a day, to the moon and back.

ACKNOWLEDGEMENTS

In the name of Allah, the most gracious and merciful, we start our project and we are thankful to Allah for helping us to complete this project and giving us the power and determination to do it faithfully and honestly. It has been a great opportunity to gain lots of experience in this real-time project, followed by the knowledge of how to actually design and analyse real projects.

For that, We want to thank all the people who made it possible for students like us. Thanks to the dean of the college for the help in allowing us to complete this project.

we would like to express our deepest gratitude to our graduation project supervisor Asst. Prof. Dr. Baraa Munqith Albaker for his enthusiasm, patience, insightful comments, helpful information, practical advice, and unceasing ideas that have helped us tremendously at all times in our research and writing of this thesis.

Without his support and guidance, this project would not have been possible.

Moreover, it is our duty to thank all the examination committee members for their generous discussions and encouragement.

At last, we would like to thank all the people who helped, supported, and encouraged us to successfully finish the graduation project, especially my family. Thanks for all your encouragement.

ABSTRACT

Classical thermal inspections of electric power transmission lines are costly and complex. In addition to that, the risks threatening the lives of maintenance workers. The idea of this project is to design and develop a quadcopter integrated with suitable thermal sensor that serve as a real-time mobile monitoring station to monitor multiple thermal inspection of electric power transmission lines. A quadcopter configuration was adopted and its avionics including autopilot controller, Electronic Speed Controllers (ESCs), Global Positioning System (GPS), servo motors were integrated onboard the Unmanned Aerial Vehicle (UAV). Many calibrations were next conducted to ensure correct flight response of the UAV to commands set by a ground pilot. AMG8833 thermal sensor was used and installed onboard the UAV to record thermal readings of a power transmission line and sends a one-dimensional signal of the thermal readings to a ground station to visualize the temperature profile in real-time manner. Several test scenarios were carried out and the results showed the successful flight operations and correct measurement of thermal reading values. As a result, the proposed system provides a suitable remote thermal profile measurement tool that is low cost, accurate, operate in real-time and can effectively use to protect maintenance works from the danger of electric power transmission lines.

TABLE OF CONTENTS

LIST OF SYMBOLS / ABBREVIATIONS

BS	Base station
CNN	Convolutional Neural Network Architecture.
Ed	Real-time line segment detection by Edge Drawing
ESC	Electronic Speed Controller
GPS	Global positioning system
IoT	Internet of things
IMU	Inertial measurement units
Lipo	Lithium Polymer
LSD	Linear-time Line Segment Detector
LIDAR	Light detection and ranging
RF	Radio Frequency
UAVs	Unmanned aerial vehicles
YOLO. Yolov3	You Only Look Once, Version 3

LIST OF FIGURES.

Chapter One

Introduction

Unmanned aerial vehicles (UAVs), also known as drones, is an aircraft without any human pilot, crew, or passengers on board. UAVs were originally developed through the twentieth century for military missions too "dull, dirty or dangerous"[1] for humans, and civilian services due to their enhanced stability and endurance in several operations. As control technologies improved and costs fell, their use expanded to many non-military applications. Applications of UAVs are expanding exceptionally due to their advanced use in the internet of things (IoT), 5G and B5G.

UAVs have been used in a variety of applications over the last decade, including object detection and tracking, public security, traffic surveillance, military operations, exploration of hidden or hazardous areas, indoor or outdoor navigation, atmospheric sensing, post-disaster operations, healthcare, data sharing, infrastructure management, emergency and crisis management, freight transportation, wildfire monitoring and logistics [1].

UAVs can be remotely piloted, whereby control commands are provided from a ground base station (BS) through a remote control. The UAVs are also capable of performing the control operations on board through autopilot and different sensors, including global positioning system (GPS) and inertial measurement units (IMU).

UAVs have many advantages including quick and simple deployment, scalability and flexibility, self-organization, cost effectiveness, and high manoeuvrability. To carry a variety of payloads, such as communication devices, navigational aids, sensors, and cameras, UAVs come in a wide range of configurations, sizes, weights, ranges, and performance traits. UAVs can be divided into various categories based on features like configuration, engine type, weight, range, and size.

There are several crucial factors limiting the performance of UAVs. Some of these factors are limited battery endurance, restricted mobility, limited autonomy, and limited flight time. Limited flight time is due to various factors including sensor

accuracy, harsh atmospheric conditions, fixed-wing size and battery endurance. UAVs have several vulnerabilities that increase the rate of being exposed to malicious attacks. Several studies are devoted to assess UAVs vulnerabilities, attacks, threats and have suggested viable solutions to overcome these challenges, such as using high quality devices including batteries, wing, geometry, manufacturing materials and motors etc. Some studies have reported optimization algorithms to find shortest route for UAVs to reach their intended destination.

1.1 Background

Power line maintenance for electric utility companies is expensive, dangerous, and time consuming. Electric utility companies must spend a lot of money, time, and safety on power line maintenance. The primary technique for finding faults is called thermal hot-spot recognition, which looks for high-impedance regions on power lines also known as "hot-spots" or "problem areas" using a thermal camera. The thermal camera can see these high-impedance regions because they produce more heat than the adjacent machinery.

Additionally, these regions show that the power line has a fault. Although it can be difficult and time-consuming, using a thermal camera to keep an eye on the power lines from the ground is frequently practical. Furthermore, when power lines are above difficult terrain, this approach is useless.

Utility companies can take advantage of the newest technologies as drones become more common. The system would save money by not using helicopters and utilize drone technology effectively. This design will be able to upload all of the data to a back-end database for upcoming analysis, unlike earlier power line monitoring systems. Utility companies will be able to review the results and locations of all of their noted problem areas as a result.

Future detection techniques could then be developed using the database of these noted problem areas. They will be able to immediately dispatch crews to high priority fault sites thanks to the front-end software's ability to communicate with the utility

companies' servers. By putting this design into practice, crews would be able to evaluate issues farther away, making the workplace safer for employees.

Many high-voltage fixtures are installed in challenging-to-reach places. Additionally, the electrical system in large transformer stations is spread out over a sizable area, making it very challenging to reach certain components. Inspections conducted from the air have long been used to improve maintenance in these complex situations.

People must currently climb the electric transmission lines in order to perform thermal inspections, which increases their risk of falling or receiving an electric shock. Additionally, this procedure is slow, takes a long time to complete, and could produce inaccurate readings.

So the issue is how to enable a remotely controlled aerial tool to access heights and precisely inspect the transmission line's thermal profile in real time.

1.2 Aim and Objectives

The aim of this project is to develop a quadcopter that is equipped with on board GPS sensor to record UAV's position and thermal sensor to read temperature profile of the electric power transmission lines. In addition, on board telemetry communication to send required information to a ground station. This is to remotely monitor position information and thermal profile of the transmission lines in timely manner. Accordingly, the work objectives are:

- To select and integrate suitable UAV frame, controller, sensors and actuators
- To calibrate and tune quadcopter parameters and perform flight tests to make it ready for a given operation.
- To install a thermal sensor with necessary communication equipment onboard UAV to measure the temperature profile of electric power transmission lines.

1.3 Literature Review

Unmanned aerial vehicles (UAVs) are now crucial tools for inspecting power transmission lines. Aerial images with information about power equipment can be efficiently obtained by cameras installed on the platforms. However, the majority of the inspection systems in use today cannot detect transmission line components automatically in real time. In order to accurately detect and locate power equipment in real time, an automatic transmission line inspection system combining UAV remote sensing with thermal sensor technology is developed in this project .The system consists of a binocular visual perception module, an embedded industrial computer, a UAV module, and a control and observation module. Insulators are chosen as the detection targets because they are both essential parts of power transmission lines and components that are prone to failure.

1.3.1 A Drone Based Transmission Line Components Inspection System with Deep Learning Technique

A real-time aerial power line inspection system was developed by the authors of project in [14] that aims to detect power line components such as insulators, splitters, damper-weights, power lines, and then analyse these transmission line components for potential defects. Figure (1.1) shows their developed inspection system.

A system for automatically detecting transmission line components and flaws is suggested. Using an embedded CNN-based components detector, the suggested system can identify nine different types of transmission line components from videos captured by a drone. It is demonstrated that the modified YOLO V3 approach outperforms the baseline model in terms of detection performance. The proposed power line detection algorithm allows the system to detect electrical power lines as well. In comparison to the LSD and ED lines methods, the proposed power line algorithm outperforms them on the test dataset in terms of both speed and accuracy. A defect detection system then scans the power line components for any potential flaws after they have been identified. The performance of the proposed defect detectors

suggests that handcrafted approaches can be used to detect some of the types of defects in situations where the availability of a large number of defected samples is not viable.

The proposed drone-based system is accelerated by an NVIDIA's Jetson TX2 GPU and uses OpenCV, CUDA, and cudNN libraries along with Darknet's CNN framework. The proposed system is tested on a large, unbiased, unconstrained evaluation dataset of transmission line components images.

Overall, their proposed inspection system offers ease of implementation and scalability, as well as an economical advantage over the manual inspection counterpart [14].

The system pipeline presented in their work provides a guide to future research, which includes pushing existing CNN models to learn transmission line components and formalizing for the detection of additional types of component defects. The drone is currently operated by a human operator, but future modifications will be made to make it autonomous by creating a collaboration between power line detection, transmission tower detection, collision avoidance sensors, and directional actuators [15].

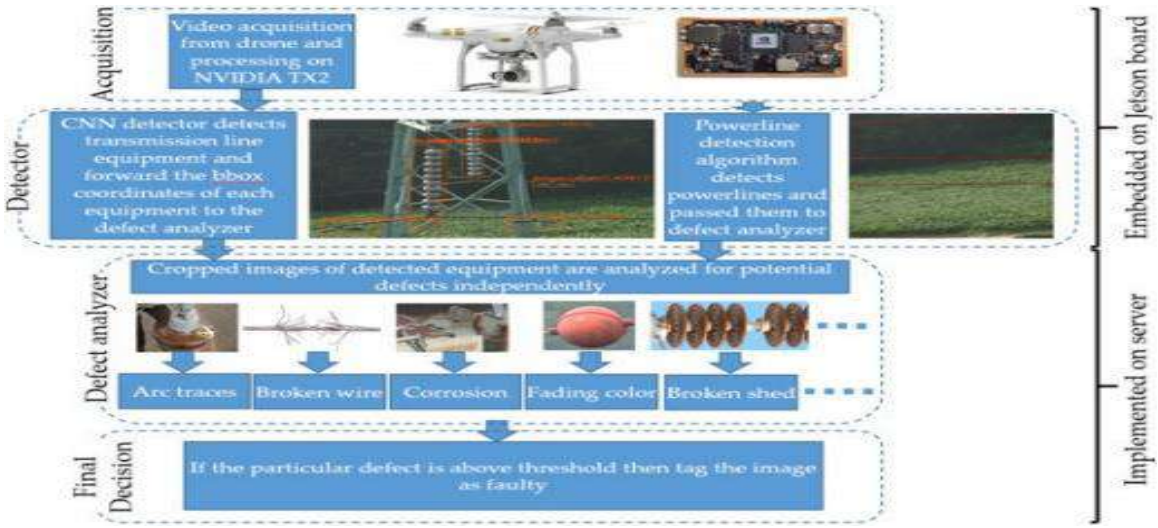

Figure (1.1) Developed transmission line inspection system in [14]

1.3.2 Automatic system for checking overhead power lines using an unmanned aerial vehicle

A UAV and an infrared camera was used in [16] in order to detect bad conductivity and hotspots in the power lines, transformers and electrical substations, as depicted in Figure (1.2).

Authors of research in [16] designed and developed a new fully automatic aerial inspection system for overhead power line inspection by Unmanned Aerial Vehicle (UAV). The main goal of the system is to process consecutive images together with the telemetry data sent from the autopilot to identify online areas of vegetation, trees and buildings close to power lines and to calculate the distance between power lines and the vegetation, trees and buildings. Additionally, the system processes the images captured by the infrared camera to detect bad conductivity and hotspots in the power lines, transformers and electrical substations. The system response times are constants of one second for calculating distance measurement and down to 0.3 seconds for detecting hotspots. The results show 3D information obtained through processing of consecutive frames of the HD images together with the telemetry data sent by autopilot.

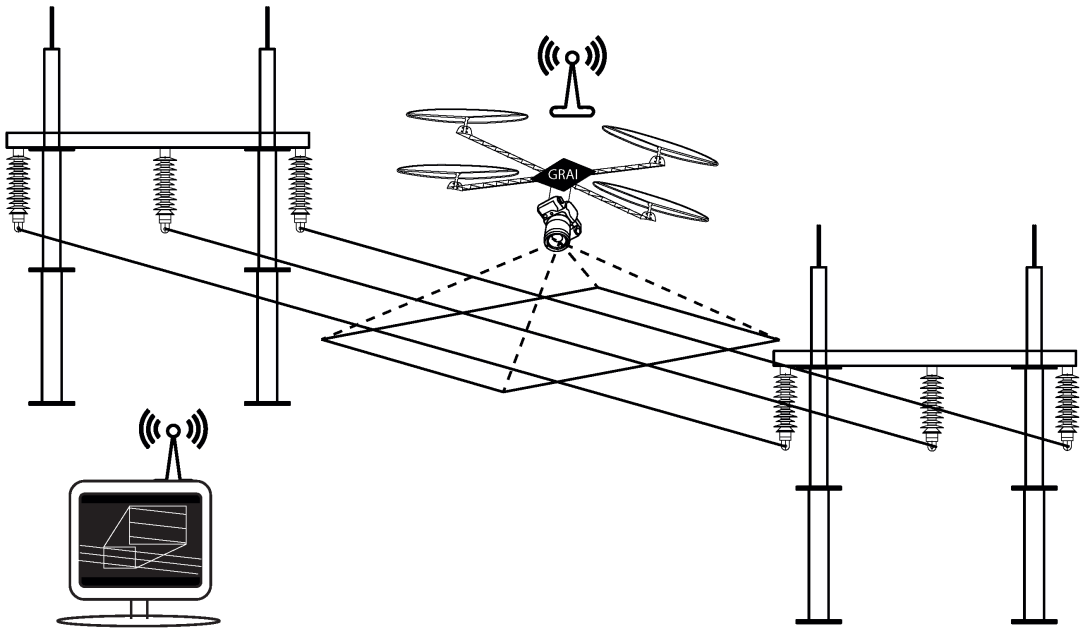

Figure (1.2) Inspection system developed in [16] for overhead power line inspection

1.3.3 Vehicles for power line inspection: a collaborative platform and communications approach.

Authors of the research in [17] proposed a multi-platform UAV system and multi-model communication system for highly efficient power line inspection tasks in China (See Figure (1.3)). Different UAVs cooperatively serve as long-distance imaging.

A new paradigm of power line inspection by using cooperative UAVs. The details of UAV functionality and communication systems are introduced and discussed. Our practical experience shows that by this cooperative operation the time taken for inspection can be greatly reduced and the efficiency can be improved tremendously. The feasibility and superiority of UAV inspection is demonstrated. The further work may include the optimization of UAV configuration in crew team.

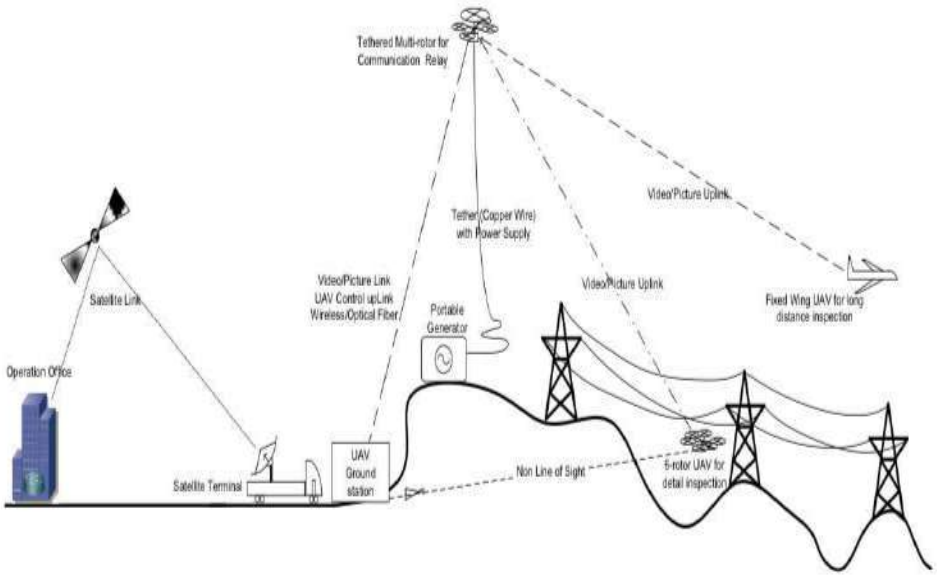

Figure (1.3) Cooperative UAVs for thermal inspection [17]

1.3.4 Real-time detection and spatial localization of insulators for scanning drones based on microscopic vision

The work in [18] presented the development of an automatic transmission line inspection system incorporating UAV remote sensing with binocular visual perception

technology is developed to accurately detect and locate power equipment in real time (See Figure (1.18)).

An automatic transmission line inspection system incorporating UAV remote sensing with binocular vision perception technology is developed to accurately detect and locate power equipment in real time. The system consists of a UAV module, embedded industrial computer, binocular visual perception module, and control and observation module. A novel insulator detection approach is proposed based on RGB-D saliency detection and structural feature searching for aerial images captured by a UAV power transmission line inspection system. On the basis of insulator detection results, a real-time object spatial localization method is proposed that combines binocular stereo vision and GPS. Experimental results have shown that the system meets the robustness and accuracy requirements of insulator detection and spatial localization in practical engineering. Further research will focus on the implementation of the insulator defect detection, the expansion of the system's hardware, and the implementation of visual servo control of UAV.

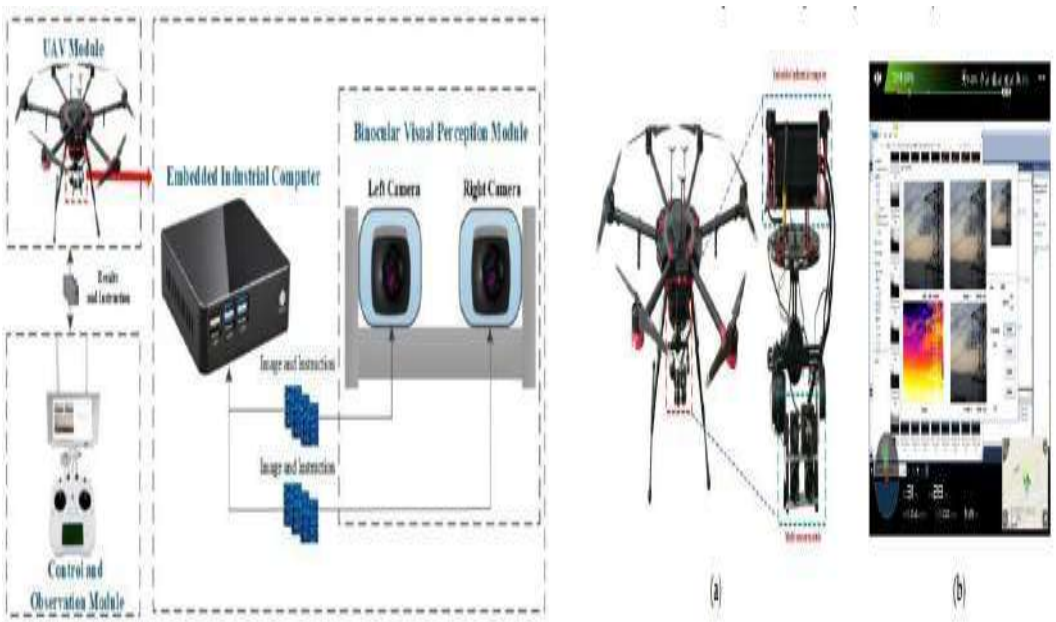

Figure (1.4) Automatic transmission line inspection system presented in [18]

1.3.5 Real-time power line corridor inspection by edge computing of uav lidar data

The work addressed in [19] presents an innovative power line corridor inspection approach using UAV LiDAR edge computing and real-time 4G transmission, as presented in Figure (1.5).

Five common types of power tower point clouds are manually categorized and divided into their component parts. The "Tovos Age Agent" is a deep learning AI agent that is trained using supervised deep learning on sample data sets in a 3D CNN framework. Using semantic feature constraints, laser points of power line corridors are simultaneously categorized into Ground, Vegetation, Tower, Cable, and Building types. In order to identify potential risks, the spatial and topological relationships between Cable points and other types are analyzed in accordance with industry standards.[19]

All potential risks are compiled into reports that adhere to industry standards and sent over a 4G data link to a central server. Tests on 1000 KV power line LiDAR data demonstrate the method's potential.

A real-time power line corridor inspection approach is being implemented using edge-computing devices and methods. LiDAR data acquisition and analysis is executed during UAV LiDAR flight, and risk assessment reports are transmitted to a central server via 4G network. Future work [20] attempted to transmit all the original data, such as LiDAR sensor data and IMU data, directly to a background server via 5G network, so that computation processes can be applied faster.

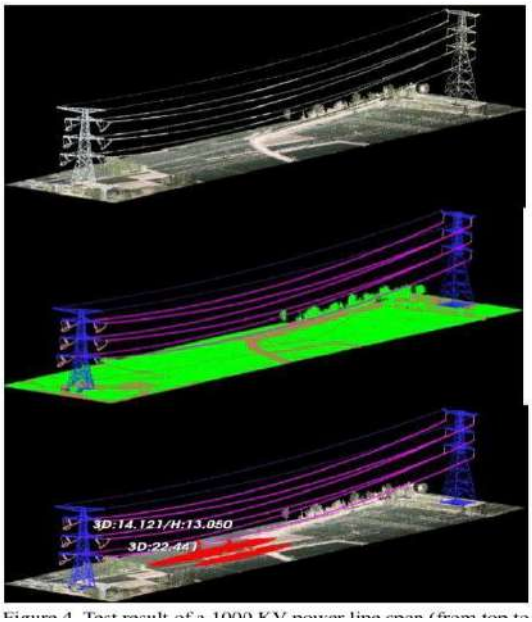

system.

Figure (1.5) Power line corridor inspection approach using UAV LiDAR edge computing [19]

Chapter Two

Methodology

This chapter presents the component selection, overall system architecture and function and the development of the remote-controlled UAV system. The methodology emphasizes the quadcopter integration, integration of the sensor. Figure (2.1) illustrates the work methodology flowchart carried out in this project.

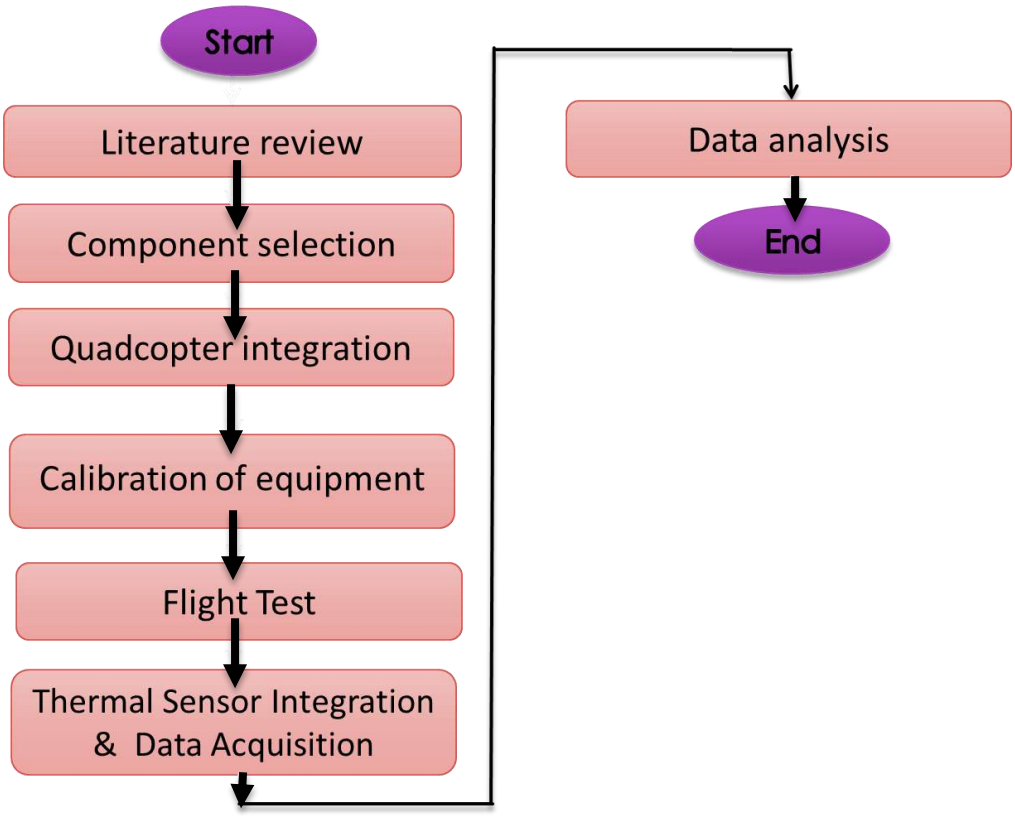

Figure (2.1) Work methodology flowchart

2.1 System Functional Overview

The proposed UAV-based inspection thermal system consists of sensors, a global positioning system (GPS) module, a microcontroller, a rfch12 communication module, and batteries. The thermal sensor was used to measure the temperature of power transmission lines. The GPS module was used to provide longitude and latitude to estimate the current location of the monitoring unit, as well as time and data. The

microcontroller organized the operation of sensor and other devices. The rfch12 module transmitted the reported data, including time, and the temperature of power transmission lines, to the ground station. The thermal sensor and the other module were connected to the microcontroller. The system was mounted on a quadcopter which was also designed and developed within this project. A couple of rechargeable batteries were used to power the monitoring system. Figure (2.1) depicts the schematic diagram of the developed thermal monitoring system.

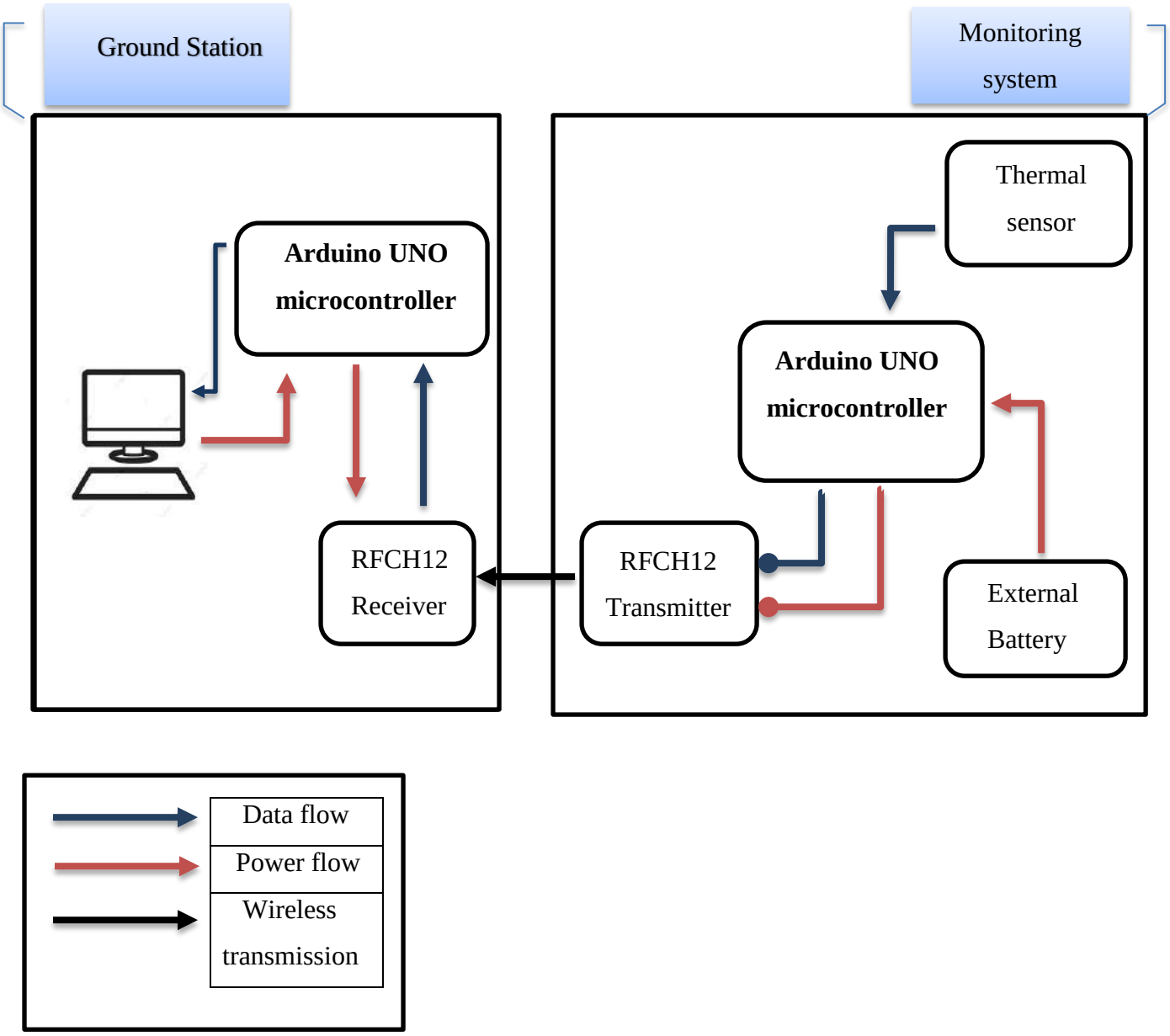

Figure (2.2): schematic diagram of the monitoring system.

Figure (2.3) shows the aerial and ground station segments that are used to monitor thermal profile of transition lines. While the user manually controls the UAV to reach to a dedicated location, the thermal sensor probe send temperature data to a ground station that receives the data, and the data is transformed into a more detailed format to display on laptop.

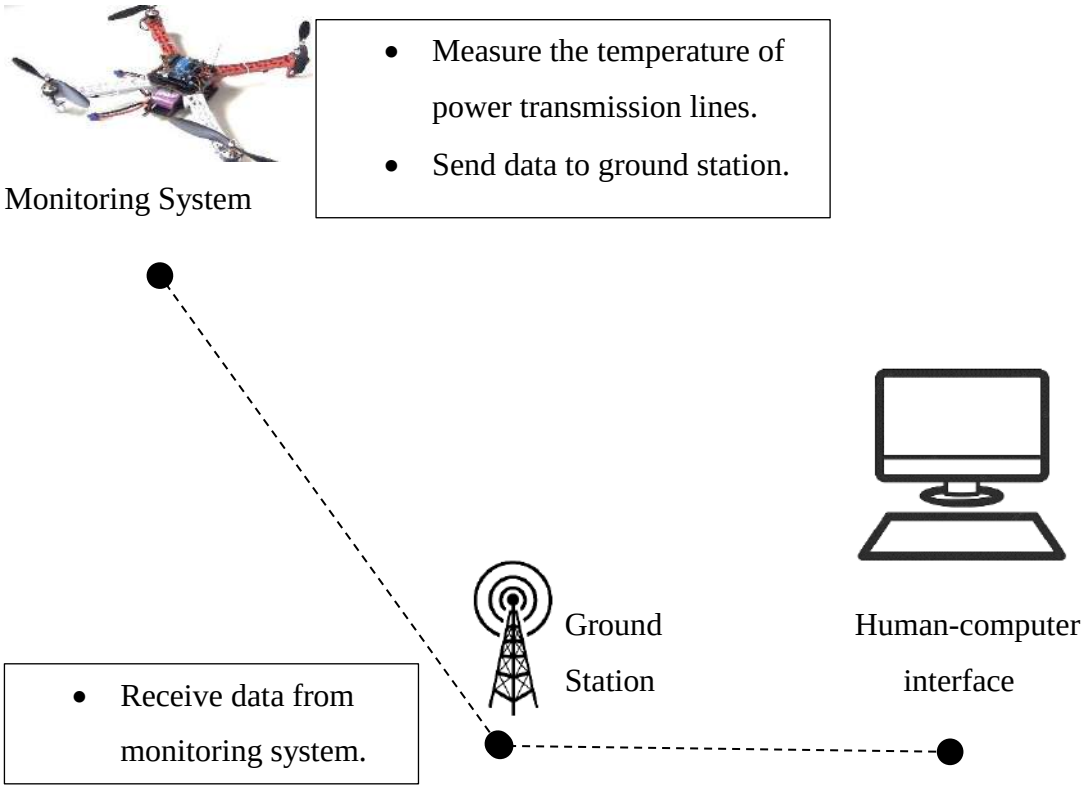

Figure (2.3): Functionality of the monitoring system

2.2 Component Selection of the UAV

The proposed UAV platform consist of frame, Electronics Speed controllers, brushless DC motor, propellers, remote controller, flight controller, battery, GPS, as shown in Figure (2.4). Each component is presented in detail in the following subsection.

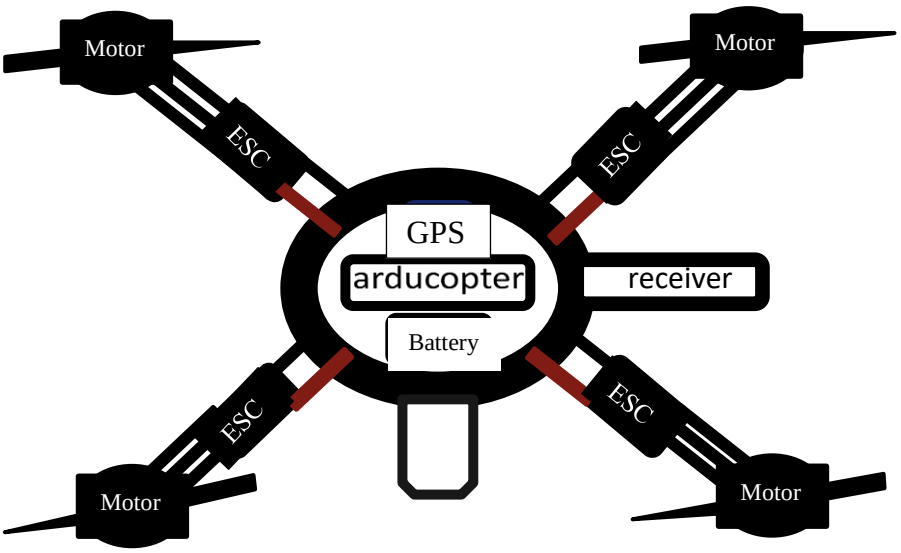

Figure (2.4) Basic block diagram of developed UAV

1- Frame:

by chose the quad frame because it's been demonstrated that four is the optimal number for balancing price, performance, stability, and flying time. A quadcopter is a multi-rotor drone with 4 motors attached

- Frame width: 450mm
- Frame height: 55mm
- Frame Weight: 282g
- Take-off Weight: 800g ~ 1200g
- Motor Mount Bolt Holes: 16/19mm
- Made by advanced engineering material, super strong & smooth.
- High quality and strong ability of anti-fall, lower maintenance cost.
- Recommended Propeller: 10×4.5in;8×4.5in
- Recommended Battery: 3S~4S LiPo
- Recommended Motor: 22x12mm (Stator size)
- Recommended ESC: 20A/30A ESC

Figure (2.5) UAV Frame

2- ESC 30A Brushless Motor Speed Controller

- Input voltage: DC 6-16.8V (2-4S Lixx)
- BEC:5V 2amp

- Running current:30A (Output: Continuous 30A, Burst 40A up to 10 Secs.)
- Size: 36mm (L) * 26mm (W) * 7mm (H).
- Weight: 32g.

Figure (2.6) ESC

Features

1. Safety Arming Feature: Regardless the throttle stick position, the motor will not spin after battery connected.
2. Throttle Calibration: Throttle range can be configured to provide best throttle linearity, fully compatible with all market available transmitters.
3. Full Protection Features: Low voltage cutoff protection / Over-heat protection / Throttle signal lost.

3- Motor: This is a A2212 brushless motor with banana plugs (1000 KV).

Specifications

- KV: 1000
- Maximum Efficiency: 80%
- Current at Maximum Efficiency: 4 to 10 (> 75%)
- Current: 12 A / 60 s
- Current @ 10 V: 0.5 A
- Nr. Cell: 2 to 3 Li-Po
- Shaft Diameter: Φ 3.17 mm
- Internal Resistance: 90 mΩ
- Dimensions: 30 mm x Φ 27.5
- Weight: 47 grams

Figure (2.7) DC brushless Motor

4- Arducoptr microcontroller

Features:

- Arduino Compatible

- 3-axis gyro, accelerometer and magnetometer, along with a high-performance barometer
- Onboard 4 MP Data flash chip for automatic data logging.
- Digital compass powered by Honeywell's HMC5883L-TR chip, now included on the main board.
- Optional off-board GPS, (any TTL level GPS should work, main choice being the uBlox LEA-6H module).
- Invernesses' 6 DoF Accelerometer/Gyro MPU-6000.
- Barometric pressure sensor, MS5611-01BA03, from Measurement Specialties.

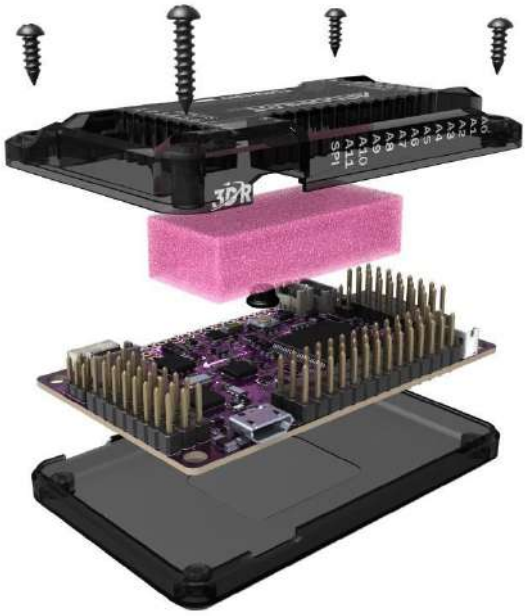

Figure (2.8) Arducopter

- Atmel's ATMEGA2560 and ATMEGA32U-2 chips for processing and USB functions.
- 5Hz GPS Module
- Dimension: Approx. 70.5x45x13.5mm
- Weight: 31g

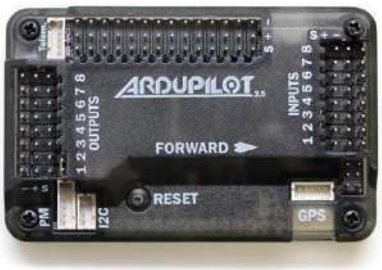

Figure (2.9) Arducoptr microcontroller

5-Propellers:

For FPV drone pilots, both two and three-blade propellers are popular for racing and freestyle flying. Most pilots prefer three-blade propellers as they are a great balance between efficiency and power, they provide more grip in the air due to the extra surface area compared to two-blade

Figure (2.10) UAV's Propellers

6-Battery lipo:

Features:

- High quality, reliable power
- Stable automatic stacking technology enables single-cell capacities of 1550mAh
- Higher capacity than comparable size packs
- Very high C rate. Designed for professional FPV racing
- No memory effect.

Specifications:

- Minimum Capacity: 1550mAh
- Configuration: 6S1P / 22.2V / 6Cells
- Discharge Rate: 130C
- Net Weight(±10g): 242g
- Dimensions:76*38*44mm (L x W x H)
- Charge Plug: JST-XHR
- Discharge Plug: XT60

Figure (2.11) UAV Battery

7-Gps M8:

GPS Chip Parameters:

- Receiver type 72-channel Ublox M8 engine
- GPS/QZSS L1 C/A, GLONASS L10F, BeiDou B1
- Galileo-ready E1B/C (NEO-M8N)

- Nav. update rate1 Single GNSS: up to 18 HZ
- Concurrent GNSS: up to 10 Hz
- Position accuracy: 2.0m CEP
- Acquisition Cold starts: 26 s
- Aided starts: 2 s
- Reacquisition: 1.5 s
- Sensitivity to Tracking & Nav: –167 dBm
- Cold starts: –148 dBm
- Hot starts: –156 dBm
- Crystal (NEO-M8M)
- Operating temperature: –40° C to 85° C
- Storage temperature: –40° C to 105°C
- Supply voltage 1.65 V to 3.6 V

Figure (2.12) Used GPS in the project

8-RC-Remote:

Features & details

- The system is built using highly sensitive low power consumption components, maintaining high receiver sensitivity, while consuming as little as one tenth the power of a standard FM system, dramatically extending battery life.
- Reliable, interference free 2.4GHz AFHDS 2A signal operation.
- 6CH operation. Use only 4 * AA batteries for transmitter. (Not included)
- Quick and extremely stable in performance.

Figure (2.13) RC Controller

2.2.1 Software:

In this project, mission planner software was used for the UAV. It is a ground control station for Plane, Copter and Rover. It is compatible with Windows only. Mission Planner can be used as a configuration utility or as a dynamic control supplement for your autonomous vehicle. Here are just a few things you can do with Mission Planner:

- Load the firmware (the software) into the autopilot board (arducopter) that controls your vehicle.

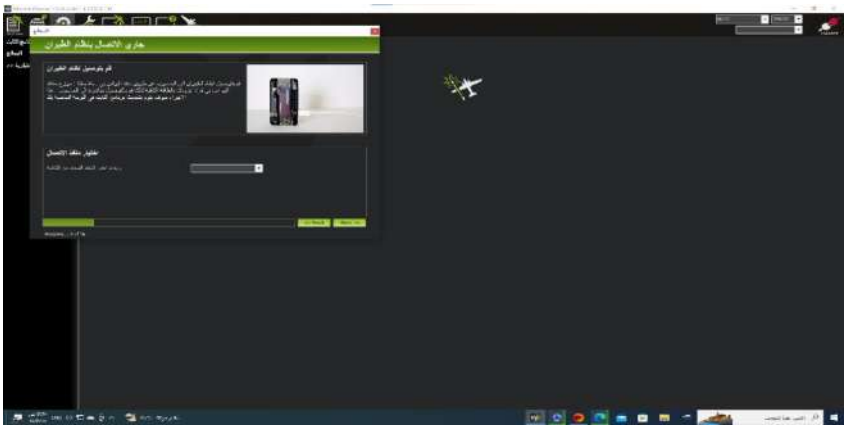

-Setup, configure, and tune your vehicle for optimum performance.

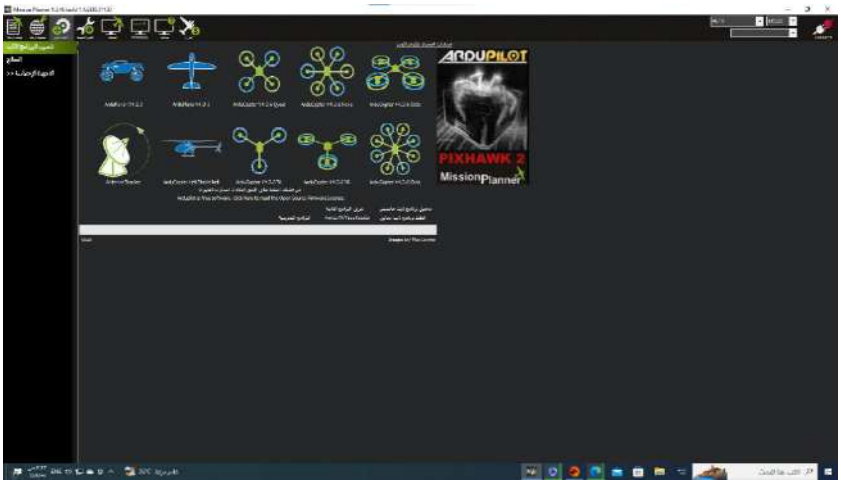

-Plan, save and load autonomous missions into your autopilot with simple point-and-click way-point entry on Google or other maps.

-Download and analyze mission logs created by your autopilot.

-Interface with a PC flight simulator to create a full hardware-in-the-loop UAV simulator.

-With appropriate telemetry hardware you can:

- Monitor your vehicle's status while in operation.
- Record telemetry logs which contain much more information the the on-board autopilot logs.
- View and analyze the telemetry logs.
- Connect Arducopter to the computer.

Figure (2.14): mission planner UAV data monitoring

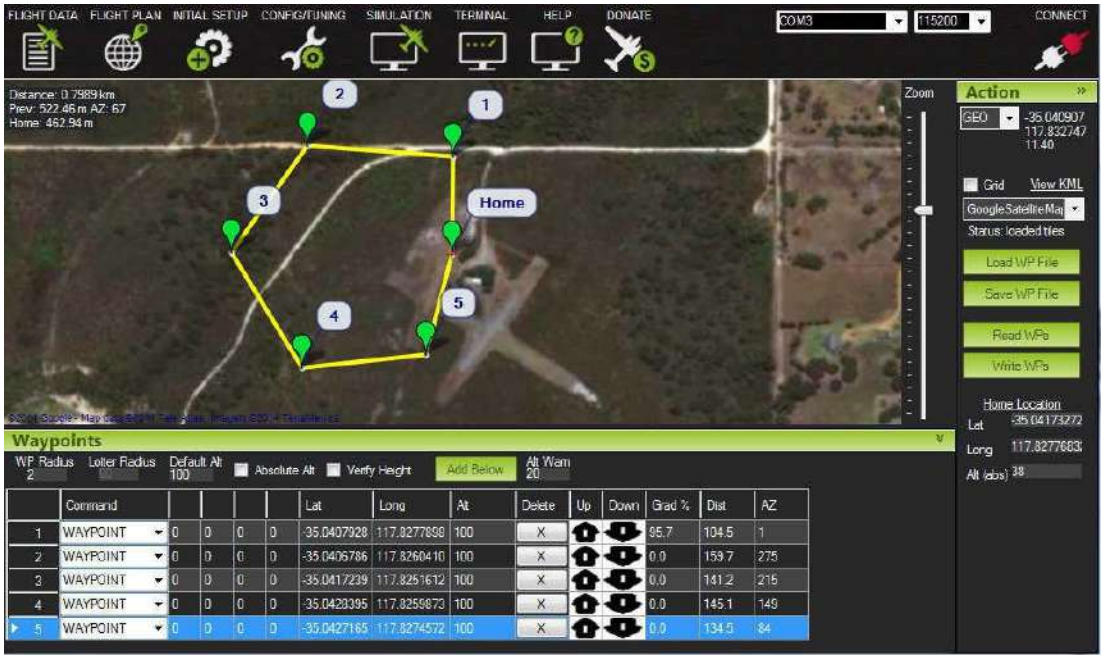

Figure (2.15): Mission planner UAV Waypoints Planning

2.3 Thermal sensor system

2.3.1 Components

The proposed system consists of microcontroller, sensor, communication module,

and batteries.

Each one will be discussed in the following:

- **Microcontroller**

  In this project، an Arduino Uno microcontroller was used in both the thermal sensor system and ground station. It used for sensor control and data collection, data logging, and communication. Arduino UNO is a microcontroller board based on the **ATmega328P**. It has 14 digital input/output pins (of which 6 can be used as PWM outputs), 6 analog inputs, a 16 MHz ceramic resonator, a USB connection, a power jack, an ICSP header and a reset button. It contains everything needed to support the microcontroller; simply connect it to a computer with a USB cable or power it with a AC-to-DC adapter or battery to get started. The Arduino/Genuino Uno has a number of facilities for communicating with a computer, another Arduino/Genuino board, or other microcontrollers. The ATmega328 provides UART TTL (5V) serial communication, which is available on digital pins 0 (RX) and 1 (TX). An ATmega16U2 on the board channels this serial communication over USB and appears as a virtual com port to software on the computer.

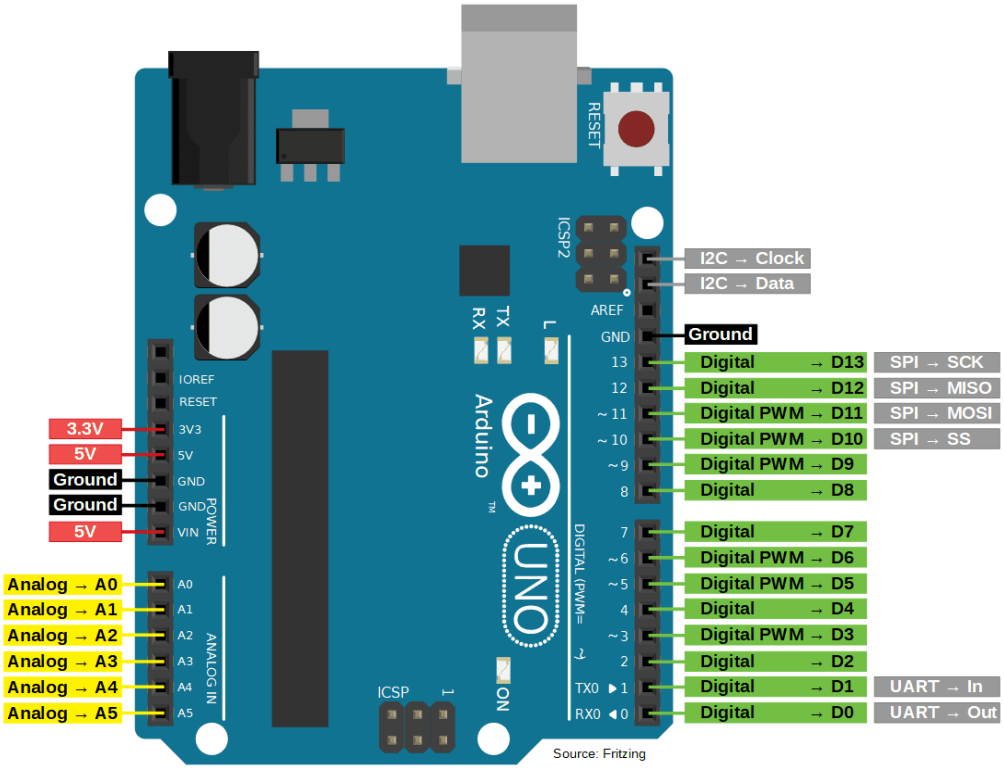

Figure(2.16) Arduino Uno

- **Thermal sensor**

The AMG8833 is the next generation of 8x8 thermal IR sensors from Panasonic, and offers higher performance than it's predecessor the AMG883. The sensor only supports I2C, and has a configurable interrupt pin that can fire when any individual pixel goes above or below a thresholds that you set.

To make it easy to use, we pick & placed it on a breakout board with a 3.3V regulator and level shifting. So you can use it with any 3V or 5V microcontroller or computer.

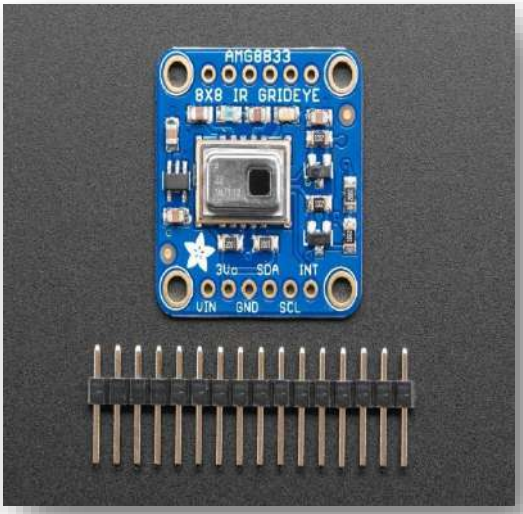

Figure (2.17) Thermal sensor

- **RF HC-12**

The HC-12 is a half-duplex wireless serial communication module with 100 channels in the 433.4-473.0 MHz range that is capable of transmitting up to 1 km. This project will begin by using the HC-12 to create a wireless link between monitoring system and human computer.

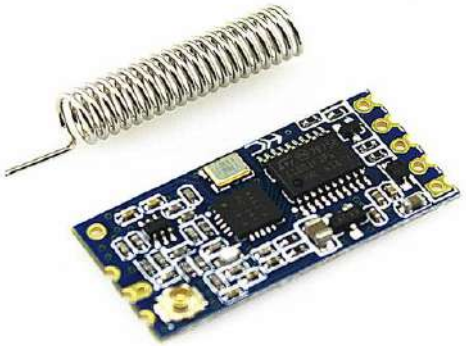

Figure (2.18) RF HC-12 Communication module

- **Lithium-Ion Batteries**

  In this project, couple rechargeable Li-ion 18650 batteries were used to power Up the thermal sensor system. It offers 3000 mAh capacity and high discharge rate. they provided suitable a voltage and current for the system.

Figure (2.19) Battery for thermal monitoring system

2.3.2 Ground station and Human-Computer Interface

In this project, the main purpose of the ground station is to receive thermal data And then transfer these data to laptop. The structure of the ground station is simple, An Rf hc-12 communication module attached to an Arduino UNO board. This setup was coded with Arduino as well. Visual basic environment was used to create a human-computer interface on the laptop, the HCI allows the user to easily monitor, map, and visualize online data.

Chapter Three

Implementation, Results and Discussions

3.1 Implementation

3.1.1 UAV Integration steps

The following steps are carried out in the UAV integration:

Step 1- Constructing the Frame: It includes attaching the four arms with frame board using screws. Also, attaching the landing gear to the frame.

Step 2- Assembling the Motors: It includes attaching the four motors to the four arms also using screws.

Step 3-Mounting the Electronic Speed Controllers (ESCs): It includes soldering the VCC (+) and GND (-) of each ESC to the power distribution board of the frame.

Step 4- Mounting the Receiver: It includes attaching the receiver on the frame board. Also, connecting each channel pin to the PPM encoder input pins.

Step 5- Mounting the Flight Controller (FC): It includes attaching the flight controller with the shock absorber plate on the frame board. Also, connecting the control cable of each ESC to the flight controller based on their order. As well as connecting the PPM encoder output pin to the RC input pin of the flight controller.

Step 6- Mounting the GPS: It includes attaching the GPS module with the folding mount on the frame. Also, connecting its pin to the flight controller GPS and I2C pins.

Step 7-Adding the Battery: It includes attaching the battery to the frame using cable times. And soldering the battery monitor module to the power distribution board.

Step 8- Adding the Propellers: It includes attaching the propellers to motors with respect to its direction. Where each adjacent propeller has different directions, with respect to the direction and order of the motors.

The resultant circuit diagram of the developed quadcopter after UAV integration together with system components wiring and the final developed arial system are depicted in Figures (3.1 to 3.3).

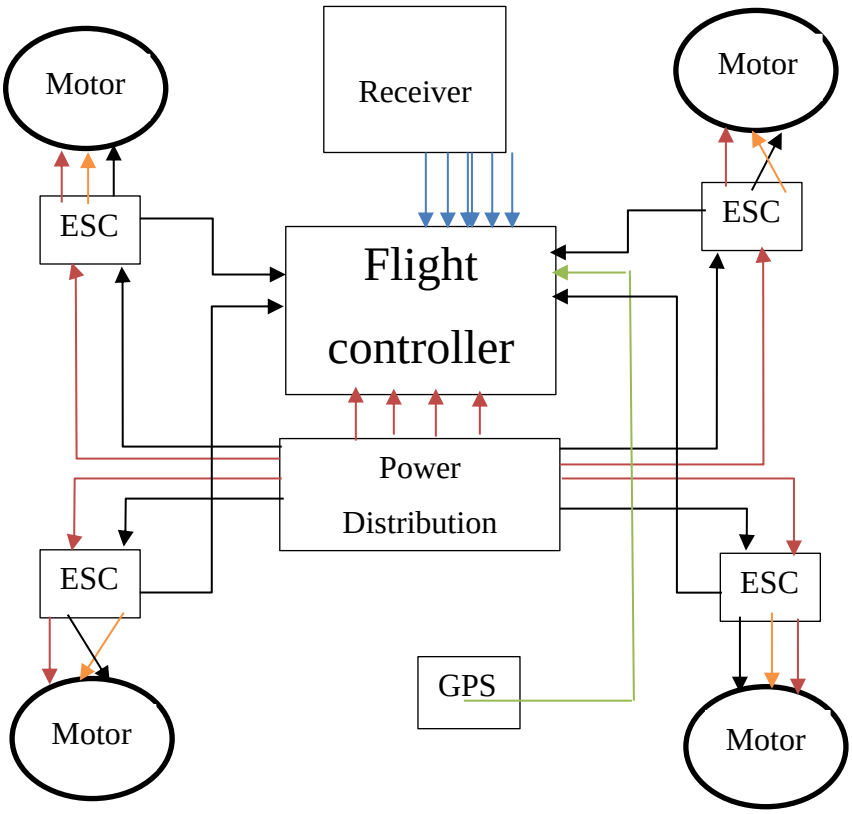

Figure (3.1): Circuit diagram of the quadcopter components wiring

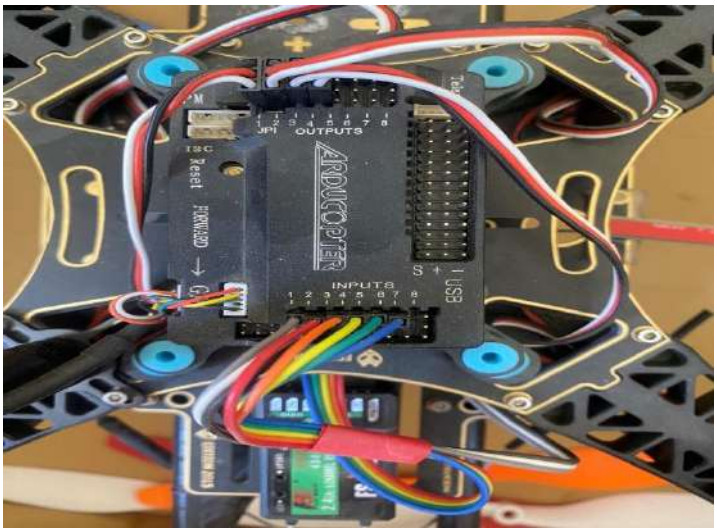

Figure (3.2): quadcopter components wiring

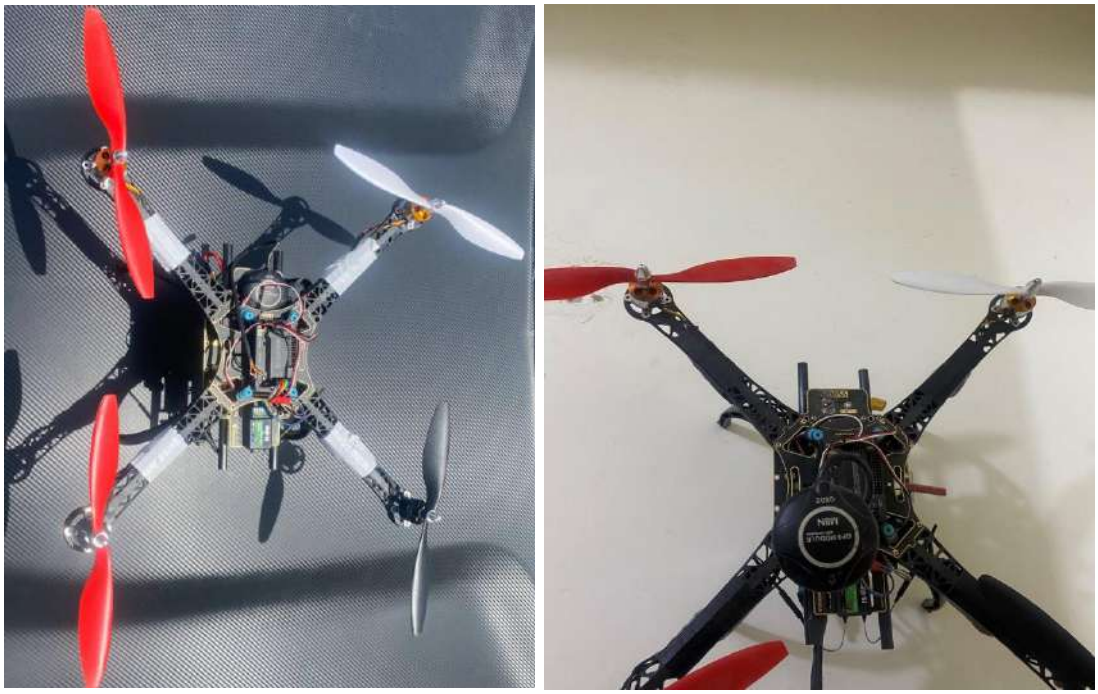

Figure (3.3): quadcopter at final steps of integration.

3.1.2 UAV Calibration

Setting up the UAV software and calibration include the following steps:

Step 1- Uploading Firmware: First, plugging the laptop to the flight controller though USB cable, then open mission planner software. After that, install firmware after choosing the quadcopter shape, as showing in Figure (3.4).

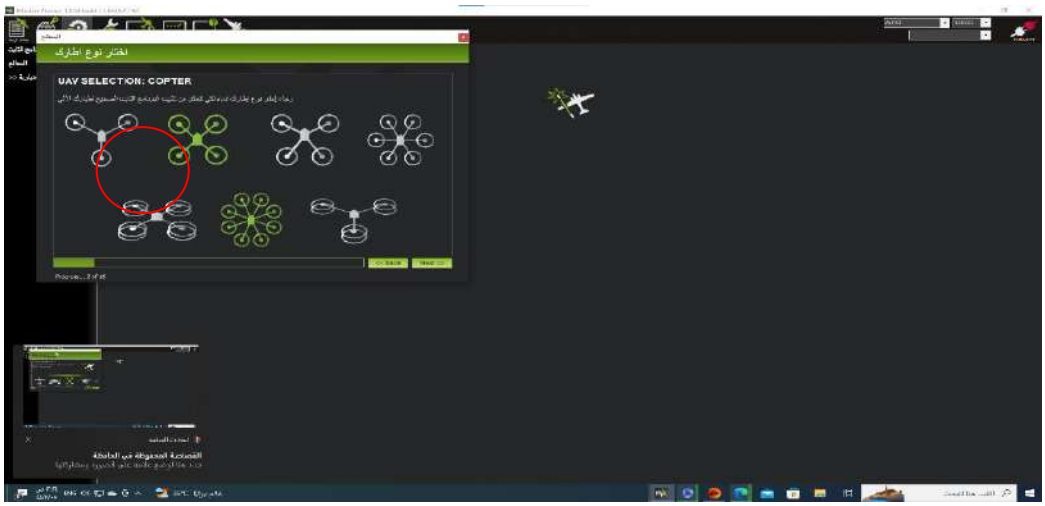

Figure (3.4): Uploading firmware 1

Step 2- Selecting Frame Type: started by choosing the COM port and Baud rate then connect to the flight controller. After that, from mandatory hardware select "Frame Type" as "X" shape (See Figure 3.5).

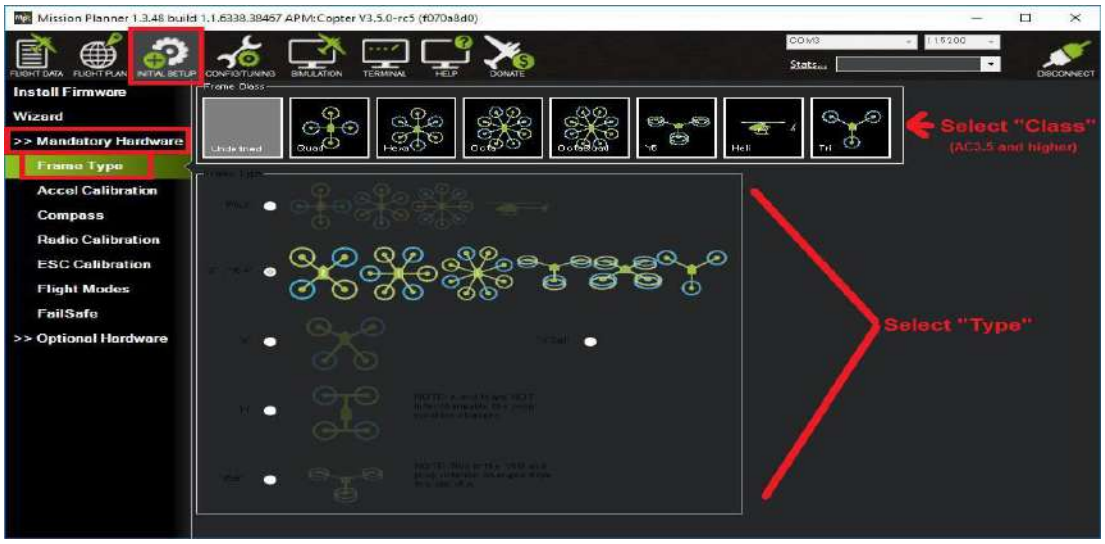

Figure (3.5): selecting Frame

Step 3- Accel Calibration: stated by clicking Accel Calibration while connecting from mandatory hardware. This calibration requires placing the UAV level, left side, right side, nose down, nose up, and back side to be completed.

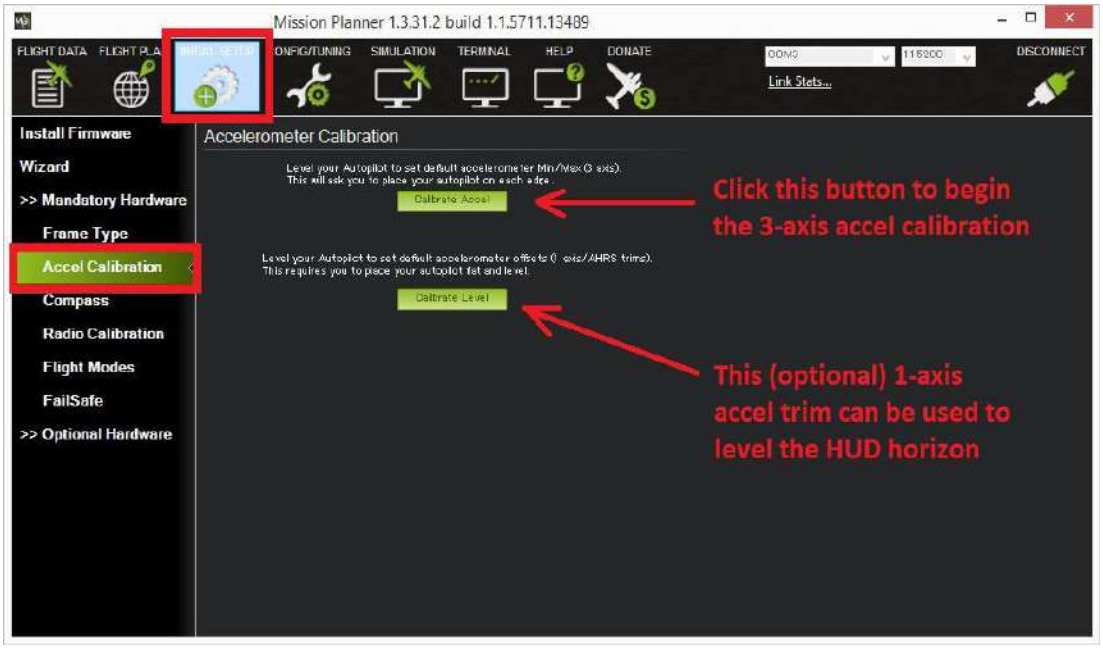

Figure (3.6): Accel Calibration

Step 4- Compass Calibration (See Figure (3.7)): again from mandatory hardware, selecting "Compass". and "On-board Mag Calibration" section's "Start" button. Then, holding the vehicle in the air and rotate it so that each side (front, back, left, right, top and bottom) points down towards the earth for a few seconds in turn. Consider a full 360-degree turn with each turn pointing a different direction of the vehicle to the ground. It will result in 4 full turns plus possibly some additional time and turns to confirm the calibration or retry if it initially does not pass. as the vehicle is rotated the green bars should extend further and further to the right until the calibration completes.

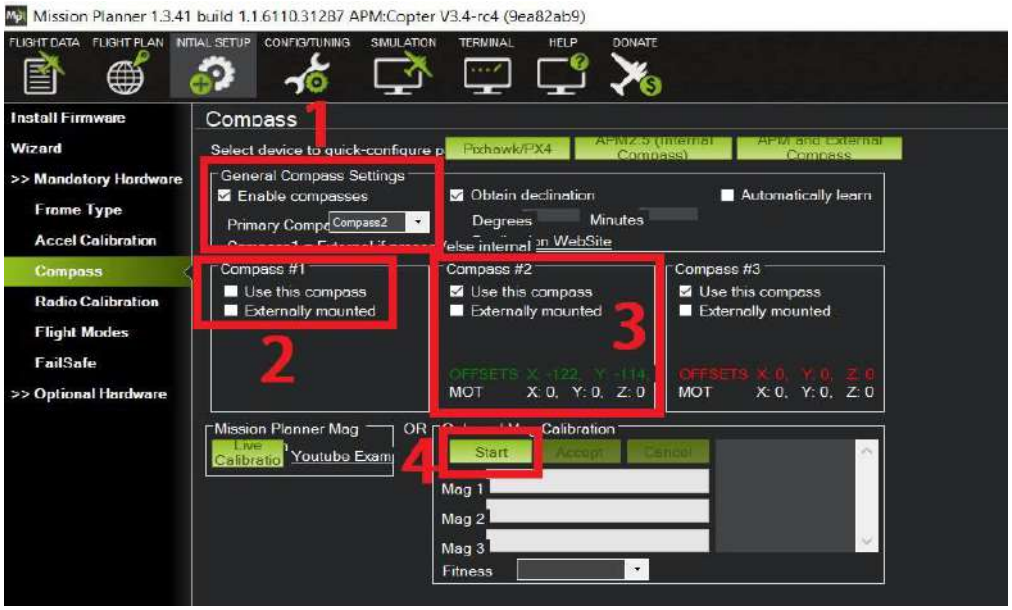

Figure (3.7): compass calibration

Step 5- Radio Calibration: while connecting, from setup and clicking on "Radio Calibration", after that, clicking on "calibrate". Then, moving all sticks and switches to their extreme limit and clicking on done as demonstrated in Figure (3.8)

Figure (3.8) Radio calibration

Step 6- Electronic Speed Controllers Calibration (See Figure (3.9)): while connecting, go to setup and from mandatory hardware click on "ESC Calibration". And click on "Calibrates ESCS". Then unplug the battery and the USB. After that plug the battery again and turn on the Radio Controller with setting the throttle stick up to its maximum position. When the flight controller start flashing "Red, Blue, and Yellow" push the safety switch until the LED displays solid red. When the ESCs complete their musical tone, pull the throttle stick down to its minimum position. Figures (3.10 and 3.11) show successful flying operation and landing of the developed quadcopter.

Figure (3.9): ESCs calibration

Figure (3.10): quadcopter flying successfully

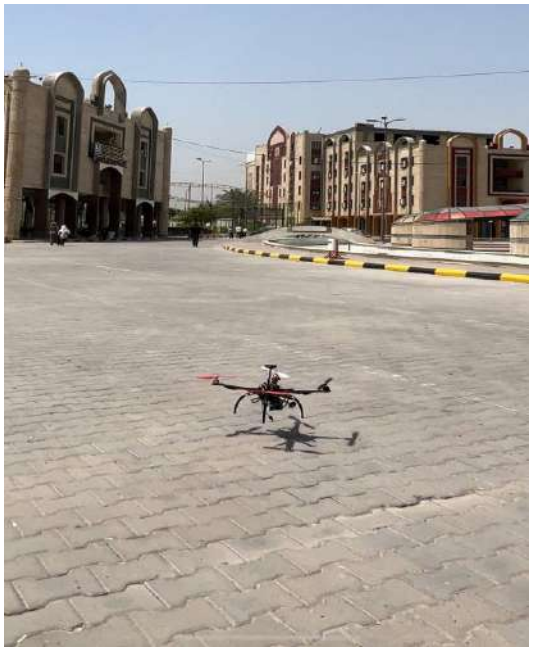

Figure (3.11): quadcopter landing

3.1.3 Thermal sensor system integration

Building the thermal sensor system include connecting the sensor, We use a drone attached to it with a thermal sensor called amg8833 through which it visualizes the fault or the problem in the power transmission line and sends a signal to the receiver on the laptop and the problem appears and we can know how to fix it . The AMG8833 Thermal Sensor is an affordable sensor that can be interfaced with a microcontroller to measure temperatures ranging from 0^0C to

80^0C., the data logger module, the communication module, and connecting the battery to the microcontroller, each step will be explained in the following

Step 1- connecting the thermal sensor (See Figure (3.12)): In this step, connecting the thermal sensor to the Arduino UNO

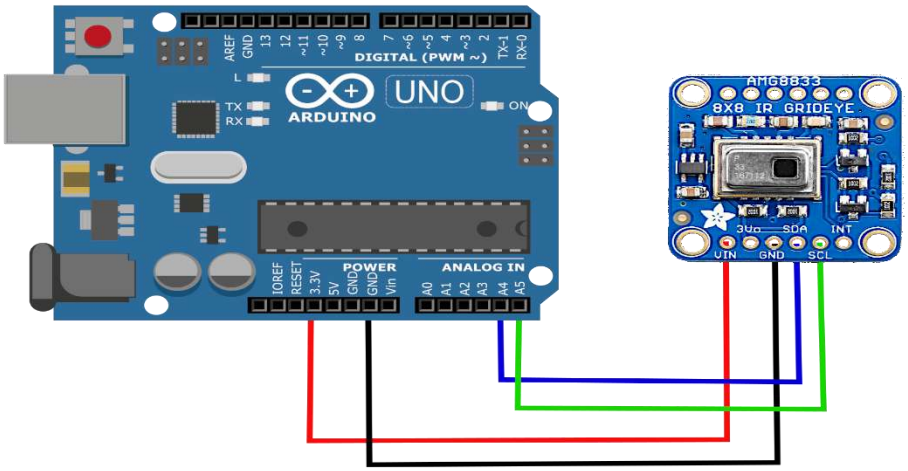

Figure (3.12): connecting the sensor

Step 2- Connecting the communication module (See Figure (3.13)): In this step, RF hc-12 Module is connected to the Arduino UNO.

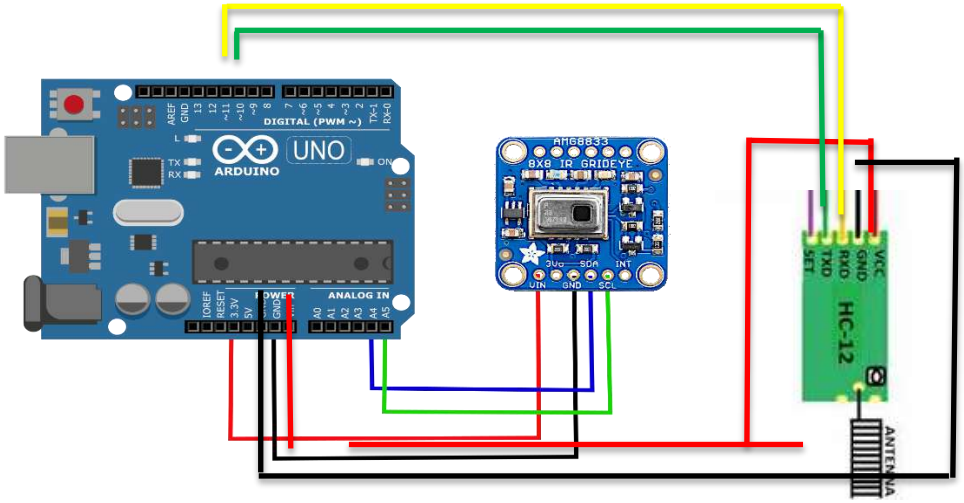

Figure (3.13): connecting the communication module

3.1.4 Ground station system integration

Building the ground station system is simple compared to the system of air pollution, as depicted in Figure (3.14). It's basically include connecting another RF HC-12 communication module to another Arduino UNO. Then programming it to work as a receiver. The ground station is connected to a laptop through serial cable to transfer the received data from the thermal sensor system to the Human-computer Interface. Figures (3.14 and 3.15) show the arial and ground segments.

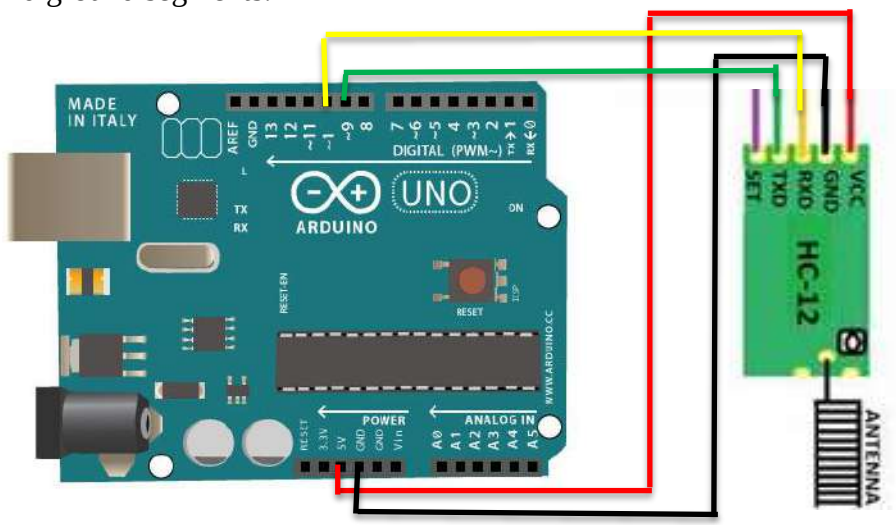

Figure (3.14): Ground station wiring

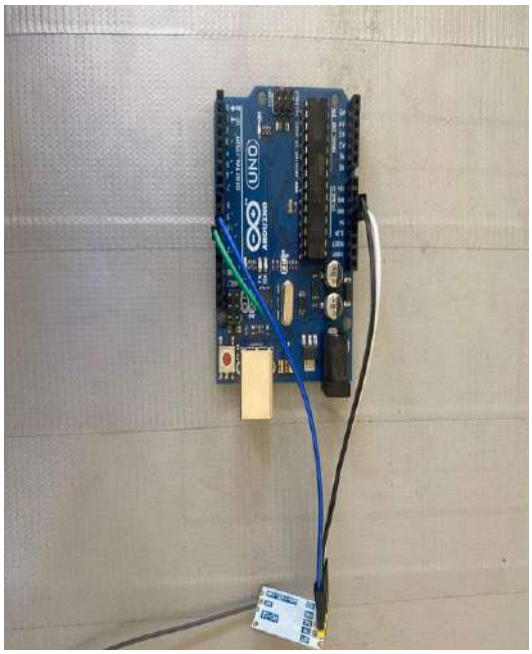

Figure (3.15): Ground station after Integration

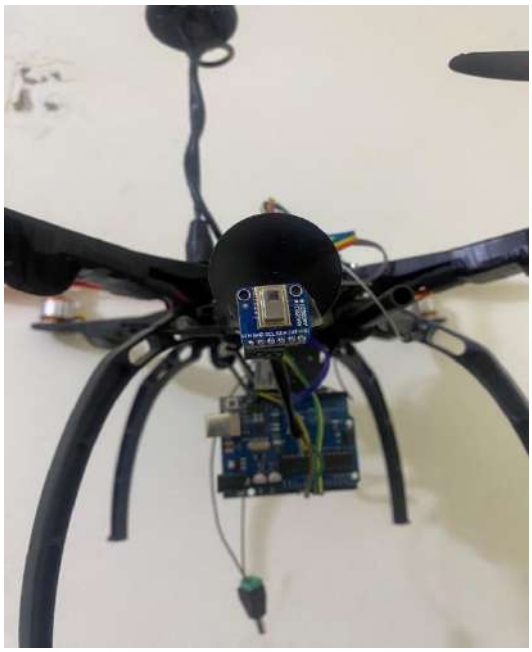

Figure (3.16): Thermal sensor after Integration

3.2 Results and Discussions

After the first experiment, several problems were encountered such as the esc was burned due to the heat generated from high current flow, so another type of ecs was used that could withstand more high currents.

When doing the next experiment on the drone, the propellers were destroyed, so they were replaced with larger propellers. After the second experiment, the motor burned, due to the wrong connection of the propellers, so we changed the direction of the propellers.

When arming the drone, it turns to the other side, due to an error in the accel calibration, so we repeated the accel calibration process more than once.

After addressing the problems that we encountered, we tried again, which showed good results by measuring the temperature with the amg 8833 thermal sensor visualizes the fault or the problem in the power transmission line and sends a signal to the receiver on the laptop and the problem appears and we can know how to fix it.

The amg8833 thermal sensor visualizes the power transmission line and then sends a signal to the receiver on the laptop which shows the power transmission line

The success of the last experiment was free of problems, as the results showed in the program the correct measurements in the power transmission lines, which were signals that appeared on the laptop screen.

The thermal sensor readings showed an average between 34.63 - 35.06. We notice the thermal sensor shows a decrease in temperature when the plane descends and moves away from the source, as presented in Figures (3.17 to 3.20).

Figure (3.17): Initial setup through detect the Heat Source

Figure (3.18): Line sensor of a single heat source

Figure(3.19) Thermal profile showing decrease in temperature when the probe is placed away from the heat source.

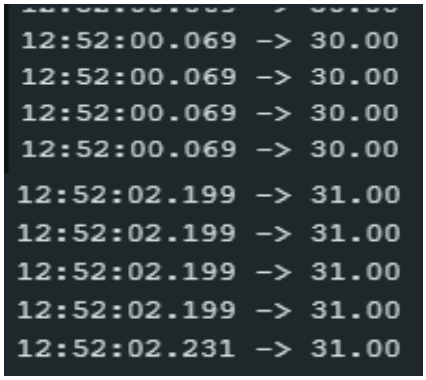

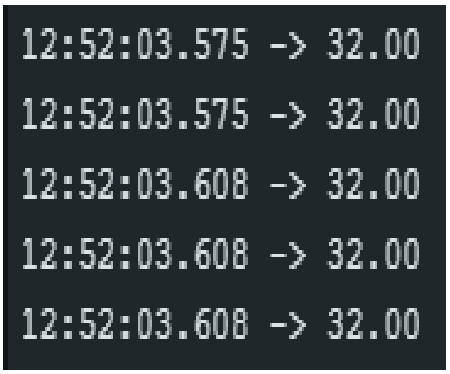

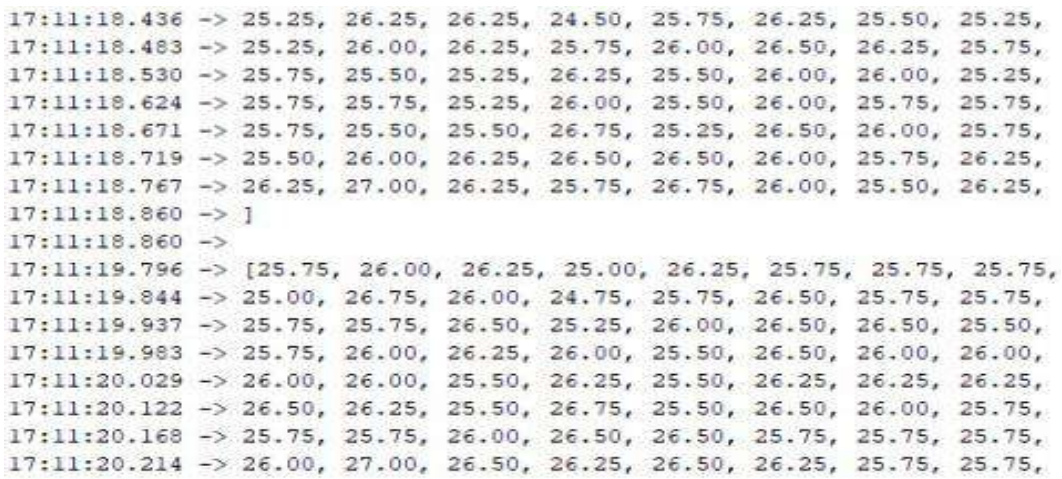

Figure (3.20): thermal sensor readings

The quadcopter represents a complete aviation inspection system that fulfils the aerial requirements and the thermal monitoring system is based on the AMG8833 thermal sensor to measure a temperature and a communication module that is used to transmit the aerial data to the ground station.

The results of this study indicate that it might not accurately represent shape of the heat source, With this specific sensor, the ideal heat signature representation can be created between 35 cm and 50 cm from the target. The Sensor works better when there is only one heat source present. The sensor would report the higher temperature if there were multiple heat sources present and their temperatures varied noticeably. All of this is done to identify the flaw or issue with the Power Transmission Lines.

Inspectors keep an eye on the reading feeds throughout the flight, and a recording of the entire flight is made for later analysis. Drones with cameras can easily control the entire system from a safe distance, so inaccessible terrain and sizable substation areas present no issues. In comparison to manual thermal camera inspections conducted on the ground, not to mention traditional visual inspections, this offers a significant improvement.

To quickly identify and separate the problem from the Power Transmission Lines of heat, it is advised to have an ESC which could withstand more high temperature and thermal sensor with a high frame rate and resolution.

The study was able to demonstrate that the use of AMG8833 thermal sensor is limited to close-range applications, such as those occurring between 35 and 50 cm from the subject. This shows how the AMG8833's make it unsuitable for short-range applications. Utilizing other thermal Sensors with higher resolution for applications that are similar is advised.

Chapter Four

Conclusions and Recommendations for Future Work

4.1 Conclusions

This project presents a low-cost, real-time and effective aerial system for thermal inspections of electric power transmission lines that can be used as a tool to minimize cost of thermal inspection and protect valuable lives of maintenance works that are working in the field of thermal inspection of power transition lines. A quadcopter integrated with AMG8833 thermal sensor was developed that serve as a real-time mobile monitoring station to monitor thermal inspection of electric power transmission lines. A quadcopter configuration was adopted and its avionics including autopilot controller, ESCs, GPS, servo motors were integrated onboard the UAV.

Several test scenarios were carried out and the results showed the successful flight operations and correct measurement of thermal reading values. However, the results of this study indicate that AMG8833 thermal sensor is limited to short-range applications. Also, it might not accurately represent shape of the heat source, with this specific sensor. The heat signature representation can be created within 50 cm from the target. In addition, the Sensor works better when there is only one heat source present. The sensor would report the higher temperature if there were multiple heat sources present and their temperatures varied noticeably. All of this is done to identify the flaw or issue with the Power Transmission Lines. Drones with cameras can easily control the entire system from a safe distance, so inaccessible terrain and sizable substation areas present no issues. In comparison to manual thermal camera inspections conducted on the ground, not to mention traditional visual inspections, this offers a significant improvement.

4.2 Recommendations for Future Works

1. Use the current proposed model to develop a swarm of UAVs that are capable of inspecting and recoding temperature profile of power transmission lines from several points at the same time.

2. Develop the current model to fly autonomously and measure temperature readings on a specific path given by the operator.

3. Improve the user-computer interface of the current proposed system to make it more interactive by adding more operator control features and displaying information of position in 3D and temperature at the same graph.

4. Use another more powerful sensor to inspect thermal profile of the power transmission lines such as thermal imaging and install it onboard with the current developed UAV.

References

1. Tice, Brian P. (Spring 1991). "Unmanned Aerial Vehicles – The Force Multiplier of the 1990s". Airpower Journal. Archived from the original on 24 July 2009. Retrieved 6 June 2013. When used, UAVs should generally perform missions characterized by the three Ds: dull, dirty, and dangerous.
2. Alvarado, Ed (3 May 2021). "237 Ways Drone Applications Revolutionize Business". Drone Industry Insights. Archived from the original on 11 May 2021. Retrieved 11 May 2021.
3. Hu, J.; Niu, H.; Carrasco, J.; Lennox, B.; Arvin, F., "Fault-tolerant cooperative navigation of networked UAV swarms for forest fire monitoring Archived 14 October 2022 at the Wayback Machine" Aerospace Science and Technology, 2022.
4. REMOTE SENSING OF THE ENVIRONMENT USING UNMANNED AERIAL SYSTEMS (UAS). [S.l.]: ELSEVIER - HEALTH SCIENCE. 2023. ISBN 978-0-323-85283-8. OCLC 1329422815. Archived from the original on 27 February 2023. Retrieved 11 January 2023.
5. Kakaletsis, Efstratios; Symeonidis, Charalampos; Tzelepi, Maria; Mademlis, Ioannis; Tefas, Anastasios; Nikolaidis, Nikos; Pitas, Ioannis (2021). "Computer Vision for Autonomous UAV Flight Safety: An Overview and a Vision-based Safe Landing Pipeline Example". ACM Computing Surveys. New York, NY: ACM. 54 (9): 1–37. doi:10.1145/3472288. S2CID 241273504. Archived from the original on 12 July 2022. Retrieved 12 July 2022.
6. Alli, B. O. Fundamental principles of occupational health and safety / Benjamin O. Alli;International Labour Office – Geneva: ILO, 2008, International Labour Office occupational health / occupational safety / hazard / role of ILO / health policy / labour legislation / HIV/AIDS / occupational health service / safety training / developed countries / developing countries , 13.04.2
7. Koparan, Cengiz; Koc, A. Bulent; Privette, Charles V.; Sawyer, Calvin B. (March 2020). "Adaptive Water Sampling Device for Aerial Robots". Drones. 4 (1): 5. doi:10.3390/drones4010005.

8. Koparan, Cengiz; Koc, Ali Bulent; Privette, Charles V.; Sawyer, Calvin B.; Sharp, Julia L. (May 2018). "Evaluation of a UAV-Assisted Autonomous Water Sampling". Water. 10 (5): 655. doi:10.3390/w10050655.
9. Koparan, Cengiz; Koc, Ali Bulent; Privette, Charles V.; Sawyer, Calvin B. (March 2018). "In Situ Water Quality Measurements Using an Unmanned Aerial Vehicle (UAV) System". Water. 10 (3): 264. doi:10.3390/w10030264.
10. Koparan, Cengiz; Koc, Ali Bulent; Privette, Charles V.; Sawyer, Calvin B. (March 2019). "Autonomous In Situ Measurements of Noncontaminant Water Quality Indicators and Sample Collection with a UAV". Water. 11 (3): 604. doi:10.3390/w11030604.
11. "Drones smuggling porn, drugs to inmates around the world". Fox News. 17 April 2017. Archived from the original on 31 August 2018. Retrieved 17 April 2017.
12. Baoyu Xu, Yilin Zhao, Tao Wang & Qingning Chen, Development of power transmission line detection technology based on unmanned aerial vehicle image vision, SN Applied Sciences volume 5, Article number: 72 (2023).
13. Xin Li, Zijian Li, Haizhi Wang, Wanlin Li* Law School, Kunming University of Science and Technology, Kunming, China, Unmanned Aerial Vehicle for Transmission Line Inspection: Status, Standardization, and Perspectives, Sec. Smart Grids, Volume 9 – 2021.
14. Zahid Ali Siddiqui, 2020, A Drone Based Transmission Line Components Inspection System with Deep Learning Technique , Source: Journal of Energies.
15. Linxin Li ,The UAV intelligent inspection of transmission lines , January 2015 ,Huazhong University of Science and Technology , Conference: 2015 International Conference on Advances in Mechanical Engineering and Industrial Informatics
16. J. I. Larrauri, Gorka Sorrosal, Mikel González, Automatic system for overhead power line inspection using an Unmanned Aerial Vehicle — RELIFO project , Published 28 May 2013, Computer Science 2013 International Conference on Unmanned Aircraft Systems (ICUAS)
17. Andrew C. Lee , B.S., United States Military Academy (2003), S.M., Massachusetts Institute of Technology (2012), Analytics-Driven Routing of Inspection Crews and Aerial Sensors for Post-Disaster Damage Assessment, Massachusetts Institute of Technology 2019.

18. Yunpeng Ma 1,Qingwu Li 1,2,*,Lulu Chu 1,Yaqin Zhou 1ORCID andChang Xu 1, Real-Time Detection and Spatial Localization of Insulators for UAV Inspection Based on Binocular Stereo Vision, College of Internet of Things Engineering, Hohai University, Changzhou 213022, China, Remote Sens. 2021, 13(2), 230
19. S. Pu, L. Xie, M. Ji, Y. Zhao, W. Liu, L. Wang, Y. Zhao, F. Yang, and D. Qiu, REAL-TIME POWERLINE CORRIDOR INSPECTION BY EDGE COMPUTING OF UAV LIDAR DATA, 04 Jun 2019
20. Yuchun HuangORCID,Yingli DuORCID andWenxuan Shi, Fast and Accurate Power Line Corridor Survey Using Spatial Line Clustering of Point Cloud , School of Remote Sensing and Information Engineering, Wuhan University, Wuhan 430079, China, Remote Sens. 2021, 13(8), 1571

APPENDIX A: Codes for thermal acquisition and ground station systems

A.1-Arduino code for Ground station system:

```
#include <SoftwareSerial.h>
SoftwareSerial mySerial(10, 11); // RX, TX
String readString;
float temp;

void setup() {
  Serial.begin(9600);
  mySerial.begin(9600);
}
void loop() {
  rece_data();

  Serial.println(temp);
}
  void rece_data()
  {
    ///// sector1
    while (mySerial.available()) {
      delay(10);
      if (mySerial.available() > 0) {
  char c = mySerial.read();  //gets one byte from serial buffer
  readString += c; //makes the string readString
      }
    }
//Serial.println(readString);

    if (readString.length() > 0) {
      //      Serial.println(readString); //see
      temp  = getValue(readString, ':', 0).toInt();
```

```
 }

 readString = "";
  }
String getValue(String data, char separator, int index)
  {
    int found = 0;
    int strindex[] = {0, -1};
    int maxindex = data.length() - 1;
    for (int i = 0; i <= maxindex && found <= index; i++)
    {
      if (data.charAt(i) == separator || i == maxindex)
      { found++;
     strindex[0] = strindex[1] + 1;
     strindex[1] = (1 == maxindex) ? i + 1 : i;
      }
    }
 return found > index ?
 data.substring(strindex[0], strindex[1]) : "";
  }
```

A.2-Arduino code for thermal sensor system

```
#include <SoftwareSerial.h>

SoftwareSerial ss(10,11);

#include <Melopero_AMG8833.h>

Melopero_AMG8833 sensor;
float temp;
String data;
void setup() {
```

```
  Serial.begin(9600);
ss.begin(9600);
 Wire.begin();
  sensor.initI2C();
  // To use Wire1 (I2C-1):
  // Wire1.begin();
  // sensor.initI2C(AMG8833_I2C_ADDRESS_B, Wire1);

  Serial.print("Resetting sensor ... ");
  int statusCode = sensor.resetFlagsAndSettings();
  Serial.println(sensor.getErrorDescription(statusCode));

  Serial.print("Setting FPS ... ");
  statusCode = sensor.setFPSMode(FPS_MODE::FPS_10);
  Serial.println(sensor.getErrorDescription(statusCode));
}

void loop() {
//  Serial.print("Updating thermistor temperature ... ");
  int statusCode = sensor.updateThermistorTemperature();
//  Serial.println(sensor.getErrorDescription(statusCode));
//  Serial.print("Updating pixel matrix ... ");
  statusCode = sensor.updatePixelMatrix();
//  Serial.println(sensor.getErrorDescription(statusCode));
temp=sensor.thermistorTemperature;
  Serial.print("Thermistor temp: ");
  Serial.print(sensor.thermistorTemperature);
  Serial.println("°C");
data=String(temp)+":"+String(0);
  delay(1000);
ss.print(data);
delay(200);
}
```

Ministry of Higher Education and Scientific research
Al-Iraqia University
Engineering College
Electrical Engineering Department

Auto Opening Gate and Vehicle Wireless Identification

A Project Submitted to the Department of Electrical Engineering in Partial Fulfilment for the Requirements of the Degree of B.Sc. Electrical Engineering

BY

Ali Qusay Abdul Majeed Abdullah

Muhammad Ali Farhan Zaid

Farah Hikmat Ali Khalil

Hussein Ali Mohsen Kazem

SUPERVISOR

Dr. Ayad Mahmood

2022-2023

DECLARATION

We hereby declare that this project report is based on our original work except for citations and quotations, which have been duly acknowledged.

Signature : _____

Name : Ali Qusay Abdul Majeed Abdullah

Date : _____

Signature : _____

Name : Muhammad Ali Farhan Zaid

Date : _____

Signature : _____

Name : Farah Hikmat Ali Khalil

Date : _____

Signature : _____

Name : Hussein Ali Mohsen Kazem

Date : _____

APPROVAL FOR SUBMISSION

I certify that this project report entitled **"Auto Opening Gate And Vehicle Wireless Identification"** was prepared by

Ali Qusay Abdul Majeed Abdullah ,Muhammad Ali Farhan Zaid , Farah Hikmat Ali Khalil , Hussein Ali Mohsen Kazem

has met the required standard for submission in partial fulfilment of the requirements for the award of Bachelor of **Electrical Engineering** at Al-Iraqia University .

Approved by,

Signature : _____

Supervisor : Dr. Ayad Mahmood

Date : _____

Abstract

With the rapid advancements in technology, there is a growing demand for automated systems that enhance convenience and security. This project proposes an auto opening gate and vehicle wireless identification system utilizing Arduino, IR sensor, and Bluetooth technology. The primary objective of this system is to provide a seamless and secure entry and exit experience for authorized vehicles, eliminating the need for manual intervention. The system consists of two main components: the vehicle identification module and the gate control module. The vehicle identification module employs an infrared (IR) sensor to detect the presence of a vehicle approaching the gate. The IR sensor detects the heat emitted by the vehicle and triggers the identification process. A unique wireless identifier, such as a Bluetooth beacon or a specific code, is associated with each authorized vehicle.

The Arduino microcontroller is responsible for processing the sensor data and comparing it with the stored wireless identifiers. If a match is found, indicating that the approaching vehicle is authorized, the Arduino sends a signal to the gate control module to initiate the gate-opening mechanism. Additionally, the system can incorporate a display or a voice prompt to provide real-time feedback to the driver. To enhance security, the system can be further integrated with a database of authorized vehicles. This allows for more advanced functionalities such as logging entry and exit times, generating access reports, and remotely managing the authorized vehicle list via a smartphone application.[1]

Chapter One

Introduction

Usage of new generation technologies is becoming an important requirement in these days. These technologies can be used in the security of building or home to reducehuman efforts, personal safety and protect building structure. Many researchers have proposed various methods of security systems. Each of these systems has its own advantages and disadvantages. One of the important security systems in building is door access control.

The door access control is a physical security that ensures the security of a building or home by means limiting access to building or home to specific car. These system control on the opening/closing of the door by receiving a decoded signal from a car, process it by a microcontroller if the code was authorized by the microcontroller then the door open. Waiting until the car entre and then close it. The main remote control technology used in the home is infrared. The signal between IR LED and PIR (Passive Infra-Red) is infrared pulses, which are invisible to the human eye. The sender sends out a pulse of infrared light when a car close from a specific door. The infrared light pulses represent a binary code that corresponds to a certain command, such as (power on). The receiver passes the code to a microcontroller, which decodes it and carries out the command. Using Bluetooth Wireless Technology (BWT) is not just for transfer of data and files only. In recent years, automation is one of the applications of Bluetooth technology. BWT enabled devices operate in 2.4-gigahertz (GHz), that use a technique called frequency hopping to minimize eavesdropping and interference from other networks. With frequency hopping, the data is divided into small pieces called packets. The transmitter and receiver exchange a data packet at one frequency, and then they hop to another frequency to exchange another packet. They repeat this process until all the data is transmitted. BWT devices randomly hop between frequencies up to 1600 times per second. This gives BWT networks a high immunity to interference from other 2.4-GHz devices . With these qualifications of IR and

Bluetooth; we offer a door automation system and car identification based on IR and Bluetooth [1] [2] [3]

Background

Auto Opening Gate and Vehicle Wireless Identification refer to technologies used in modern automated gate systems and vehicle access control. break down these **concepts:**

Auto Opening Gates, also known as automatic gates, are designed to open and close without manual intervention. They are commonly used in residential, commercial, and industrial settings for enhanced security and convenience. These gates can be operated using various mechanisms such as sliding gates, swinging gates, or barrier arm gates.

The auto opening feature can be triggered by different methods, including**:**

Remote Control: Users can open and close the gate using a handheld remote control device.

Proximity Sensors: Sensors detect the presence of a vehicle or person near the gate and automatically initiate the opening process.

Intercom Systems: Intercoms allow visitors to communicate with the property owner or a security guard who can remotely open the gate.

The benefits of vehicle wireless identification systems include:

Increased Security: Only authorized vehicles with valid IR tags can gain access, enhancing control and reducing the risk of unauthorized entry.

Convenience: Drivers do not need to manually present identification or stop at checkpoints, as the identification process is automatic.

Data Collection: The system can log and record information about vehicle entry and exit times, aiding in monitoring and reporting.

These technologies are often integrated to create seamless and secure access control systems, where the auto opening gate is triggered automatically upon successful vehicle wireless identification[4].

1.2 Aims and Objectives

Aims:

To design and implement an automatic gate opening system using Arduino and IR sensor.

To develop a wireless vehicle identification system using Bluetooth technology and Arduino.

To integrate the gate opening system and vehicle identification system for seamless operation.

Chapter Two

Methodology

2.1 System Overview

System can be activated by either using IR Sender/Receiver, Bluetooth through an application by the mobile phone or directly by pressing button on the board. By whatever way the doors are opened, the system automatically turns on the lights and the last stays on even after the door close for further 20 seconds. On another hand, closing the door can be done by IR sensor

On another hand, closing the door can be done by IR Sender/Receiver, Bluetooth device or directly pressing the close button on the board. If no one of previous action is executed, the door is closed automatically after 40 seconds. Neither of the above closing methods can turn off the light. [5]

2.2 Arduino Platform: The research will focus on utilizing the Arduino platform for implementing the auto-opening gate and vehicle wireless identification system. Arduino provides a versatile and cost-effective solution for prototyping and deploying automation projects. The necessary components, such as Arduino boards, motor drivers, sensors, and wireless modules, will be identified based on the requirements of the system [6] [7] .

Figure 1. Arduino UNO [8]

2.3 System Design and Development: Based on the literature review and requirements analysis, a comprehensive system design will be developed. This design will outline the integration of the auto-opening gate mechanism and vehicle wireless identification using Arduino. The design will consider factors such as gate opening/closing mechanisms, obstacle detection, wireless communication protocols, and user authentication [9].

2.4 Arduino Programming: The Arduino programming language, based on C/C++, will be used to develop the software for controlling the gate opening mechanism and vehicle identification. The programming code will incorporate functions for receiving wireless identification signals, processing them, and triggering the gate opening mechanism accordingly. Error handling and security features will also be implemented [8].

2.5 Prototype Development and Testing: A physical prototype of the auto-opening gate system will be built based on the system design. The Arduino components, sensors, and actuators will be assembled according to the specifications. The prototype will undergo rigorous testing to ensure the reliability and accuracy of gate opening/closing, vehicle identification, and overall system performance [10].

2.6 Performance Evaluation: The performance of the auto-opening gate and vehicle wireless identification system will be evaluated based on various metrics, such as response

time, accuracy of vehicle identification, and robustness to external factors (e.g., environmental conditions, interference) [11].

2.6 Arduino IR (Infrared) receiver sensor

It is a component that allows an Arduino board to receive and decode signals from an infrared remote control or other IR sources. It is commonly used in projects involving remote control systems, home automation, robotics, and more.

Here's a basic overview of how an Arduino IR receiver sensor works:

the IR receiver module has three pins: Vcc (power supply, typically connected to 5V on the Arduino), GND (ground, connected to the Arduino's GND pin), and OUT (output, connected to a digital pin on the Arduino).

Library: Download and install the IRremote library for Arduino. This library provides functions and tools to receive and decode IR signals easily [11].

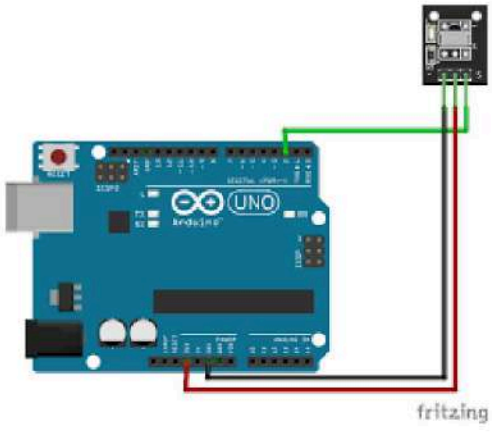

Figure 2. IR (Infrared) receiver sensor [11]

Arduino Programming Recognizing remote codes

```
#include <IRremote.h>

const int receiverPin = 3;  // Input pin for IR receiver

IRrecv irReceiver(receiverPin);

decode_results results;

void setup() {

  Serial.begin(9600);

  irReceiver.enableIRIn();  // Initialize the IR receiver   }

void loop() {

  if (irReceiver.decode(&results)) {

    // Process the received signal

    Serial.println(results.value, HEX);  // Print the received
value in hexadecimal

    irReceiver.resume();  // Enable receiving the next
signal                }}
```

2.2.6 The Arduino Bluetooth HC-06 module

It is a popular Bluetooth module that allows adding wireless communication capabilities to Arduino projects. The HC-06 module acts as a slave device, meaning it can only establish a connection when it receives a connection request from a master device such as a smartphone or computer.

The phone can be connected to Bluetooth via an application, and this allows controlling the opening or closing of the door [12][13].

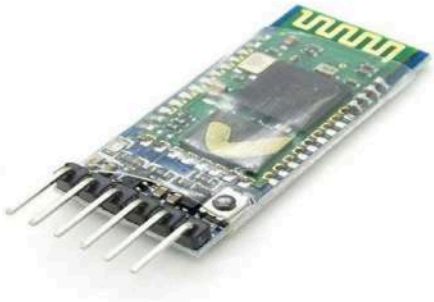

Figure 3. Bluetooth HC-06 module [12]

2.2.7 IR Sensor

It is an electronic device that emits infrared lights to sense some aspect of the surroundings and can be employed to detect the motion of an object. As this is a passive sensor, it can only measure infrared radiation. This sensor is very common in the electronic

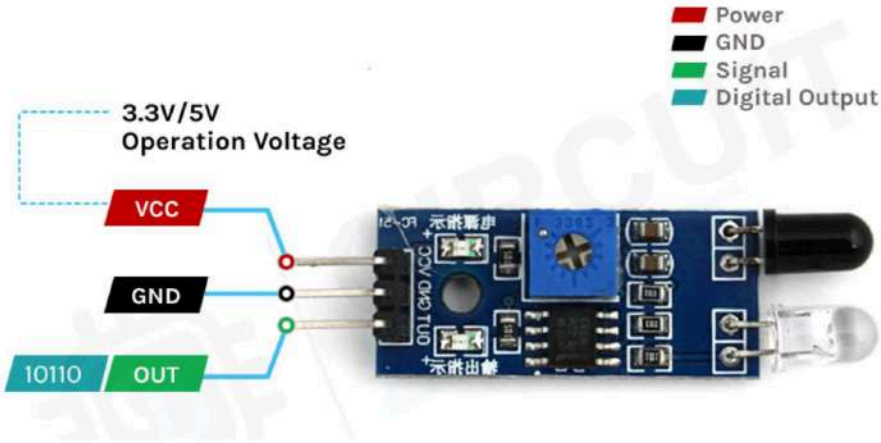

Figure 4. IR sensor [8]

The working of the IR sensor module is very simple, it consists of two main components: the first is the IR transmitter section and the second is the IR receiver section. In the transmitter section, IR led is used and in the receiver section, a photodiode is used to receive infrared signal and after some signal processing and conditioning, you will get the output.

It is used inside the project for the purpose of security . it is placed to detect strange cars that are in front of the door, and when there is a car, the sound and light alarm will work [8].

2.3. Software Lock System

When a car that has ID come in the front of the door that open either by IR sender or Bluetooth, if IR receiver used, then IR LED in a car send a (car ID) signal to IR receiver, the Arduino processed the ID if it is authorized the door open. If an application in mobile phone used to open the door, Arduino also processed the incoming ID from Bluetooth if it is authorized the door open.In the two way of opening the door, a timer count to 40s and close the door , but if the car was in middle of the two doors, then the door do not close until the car moved away from the middle. Also buzzer and light turn on into 60 s. If the emergency case happen and the user want to enter/exit immediately, the user pressed on the open/close button an interrupt happen and the door open/close [5].

When this sensor detects any movement in the garage it will automatically open the light, and then turn off after 60 second from any last order. Also when an obstacle is situated in front of the door it turns on the lights.IR obstacle avoidance Sensor

This sensor is mounted at the border of the left side of the front door used to prevent closing the door while the car in the middle

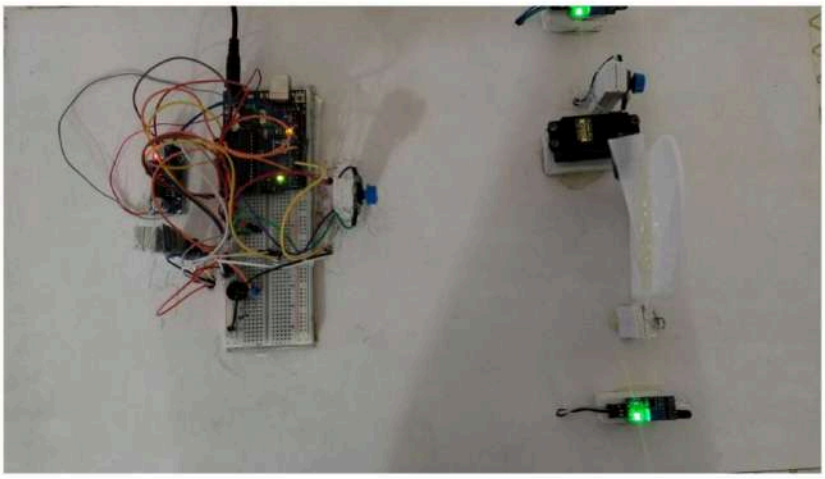

Figure 5: Auto opening gate and vehicle wireless identification

2.3.1 Control Unit

It is using Arduino as the main processing unit shown in Figure 6, and the schematic of the controller shown in Figure 8 below. Used to control the opening and closing of the sliding door. The microcontroller is programmed using the Integrated Development Environment (IDE). The control unit gets the input from the sensing unit, decodes them and then takes the following steps:

- Control the gate opening and closing.
- Generate the timing signal for the system.
- Decode signal that sensed by sensing unit.
- Activate the buzzer and light.

Opening the door by whatever the way; resets a timer system within the Arduino board, and this timer increases with each 500 milliseconds until its counter reaches 40 s where a signal is passed to close the door if not closed manually .Once the counter reaches 60s another order passes to turn off the lights. When closing the door manually [8].

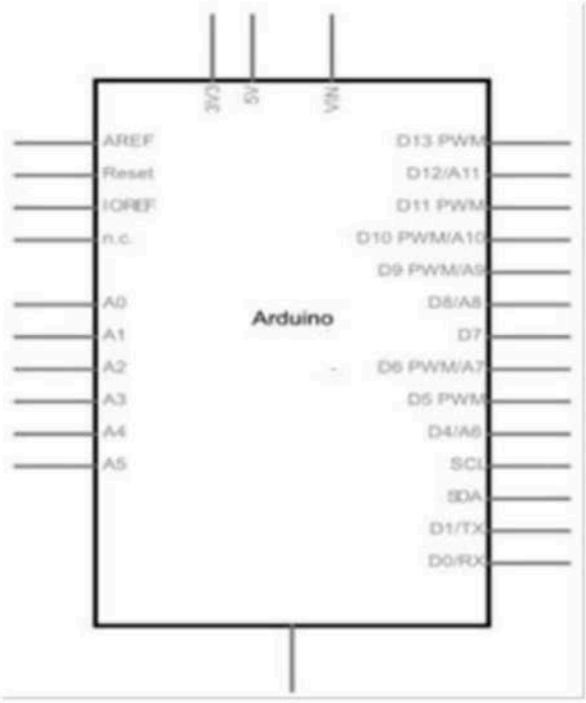

figure 6. The control unit schematic. [8]

only takes 20s second to turn off the lights. There is no way to turn off the lights manually. By pressing any one of the two buttons can interrupt any function in the board and do specific function which is either opening or closing the doors. Through all the steps of the control system, a buzzer signal is used for debugging and for notification, at different length, the buzzer can tell you whether the doors are open, closed, you gave a wrong order, or the doors are closed and waiting for the lights to turn off. There is no buzzer signal when an obstacle is situated between the doors or when the time after the last signal is passed 60 seconds [9].

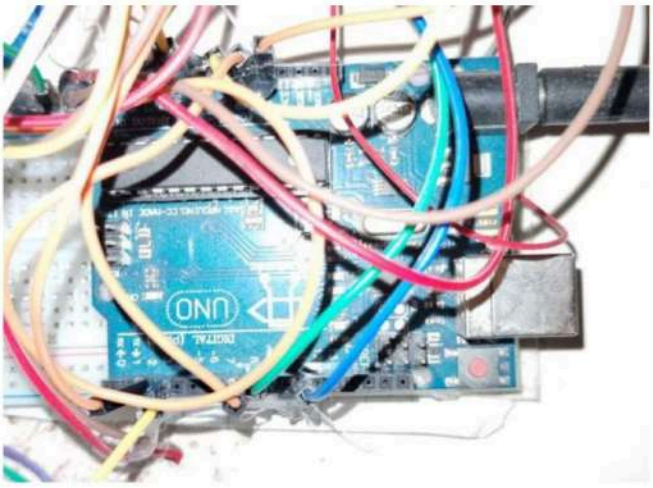

figure 7. Receiving and control circuit

Chapter Three

Results and Discussions

The auto opening gate utilizes sensors and actuators to detect approaching vehicles and open the gate automatically. Various technologies can be employed for this purpose, such as proximity sensors, infrared sensors, or even computer vision systems. These sensors can detect the presence of a vehicle and trigger the gate to open without requiring any manual intervention. This feature offers convenience to vehicle owners by eliminating the need to manually open and close the gate every time they enter or exit the premises.

Time-saving: The automated system reduces waiting time, as the gate opens promptly upon vehicle detection, improving overall efficiency.

Enhanced security: Vehicle wireless identification adds an extra layer of security by ensuring that only authorized vehicles can gain access. This helps prevent unauthorized entry and enhances the overall security of the premises.

Reduced human error: With the automated gate and wireless identification, the reliance on manual operations and input is minimized, reducing the potential for human error in granting or denying access.

Scalability: The system can be easily scaled to accommodate a large number of vehicles, making it suitable for various applications such as residential communities, commercial parking lots, and gated facilities.

Challenges and Considerations:

System Reliability: The auto opening gate and wireless identification system should be designed to operate reliably under different environmental conditions, including varying weather and lighting conditions.

Security Measures: It is essential to implement robust encryption and authentication protocols to prevent unauthorized access to the wireless identification system.

Maintenance and Support: Regular maintenance and technical support should be provided to ensure the smooth operation of the system over time.

Cost: The implementation of an auto opening gate and wireless identification system involves initial costs for equipment, installation, and infrastructure. However, the long-term benefits, such as increased convenience and security, often outweigh the initial investment.

Overall, the integration of auto opening gates with vehicle wireless identification systems offers a seamless and secure access control solution for vehicles. It enhances convenience, improves security, and streamlines the entry and exit process for both residential and commercial applications [12]

This limitation in distance has an important security implication: in the event of a pursuit by criminals the owner's car can open the door while still moving towards it and then close the gate immediately after gaining entry from a close button. Auto-opening gates and vehicle wireless identification systems are commonly used in various settings such as residential complexes, parking lots, and toll booths. These systems provide convenience, security, and efficient traffic flow. In this section, we will discuss the results and implications of such systems.

1-Ease of Access: Auto-opening gates with vehicle wireless identification provide a seamless entry and exit experience for authorized vehicles. When a recognized vehicle approaches the gate, the system automatically identifies it and opens the gate without

requiring any physical interaction from the driver. This feature saves time and effort for both residents and visitors.

2-Improved Security: Vehicle wireless identification systems enhance security by allowing only authorized vehicles to enter the premises. Each authorized vehicle is equipped with a unique identifier, such as a transponder or a tag, which is recognized by the gate system. Unrecognized vehicles are denied entry, reducing the risk of unauthorized access.

3-Traffic Management: Auto-opening gates coupled with vehicle wireless identification help in streamlining traffic flow in busy areas. The system can handle a large volume of vehicles efficiently, minimizing congestion and reducing the time spent at entry and exit points. This is particularly beneficial in parking lots, toll booths, or areas with restricted access.

4-Integration with Security Systems: Auto-opening gate systems can be integrated with other security measures, such as CCTV cameras and access control systems. This integration provides a comprehensive security solution, allowing for monitoring and recording of vehicle movements. In case of any security incidents, the recorded information can aid in investigations.

5-Challenges and Limitations: Despite the benefits, there are a few challenges and limitations to consider. Firstly, there can be occasional technical glitches or failures in the system, resulting in inconvenience for users. Regular maintenance and testing are essential to ensure the system's reliability. Secondly, there is a possibility of fraudulent activities, such as cloning or tampering with vehicle identifiers. Implementing robust encryption and security protocols can help mitigate these risks.

6-Cost Considerations: The installation and maintenance costs of auto-opening gate and vehicle wireless identification systems can vary depending on the complexity of the system and the scale of the implementation. Factors such as the number of gates, the range of the wireless identification system, and integration with existing infrastructure can influence the overall cost. However, the long-term benefits, including enhanced security and improved efficiency, often outweigh the initial investment.

In conclusion, auto-opening gate and vehicle wireless identification systems provide several advantages in terms of convenience, security, and traffic management. These systems are widely used in various applications and contribute to efficient and safe access control. While challenges exist, proper implementation, maintenance, and security measures can help overcome these limitations and maximize the benefits of such systems [6][7][8].

Chapter Four

Conclusion and Recommendations for Future Work

4.1 Conclusion

The system described in this project has been constructed to operate a small door depend on car identification. The systems successfully operate by using infrared ray and Bluetooth wireless technology. Arduino was the main control unit that controlled on the opening/closing door depends on the received signal from sensing unit. The prototype constructed in order to demonstrate the workability of the design. It can be modified to form part of an electronic toll collection and other entry or pass through systems that require much car identifications. A bigger door can still be operated with the control system described but the driver circuitry must use components that can handle more power required to drive the door

Through our study, we have achieved the following key findings:

Auto-opening Gate System: We have successfully designed and implemented an auto-opening gate system that utilizes various sensors and technologies. The system can detect approaching vehicles, verify their identity, and automatically open the gate to grant access.

Security and Reliability: We have implemented robust security measures to ensure that only authorized vehicles can access the gate. This includes secure wireless communication protocols, encrypted identification data, and authentication mechanisms. The system has demonstrated reliable performance in various testing scenarios.

User Experience: The auto-opening gate and wireless identification system offer significant convenience and ease of use for vehicle owners. It eliminates the need to manually present access cards or keys, saving time and effort. The system can be seamlessly integrated into existing gate infrastructure, making it suitable for both residential and commercial applications.[1]

4.2 Recommendations for Future Work:

While our research has provided valuable insights and a functional prototype, there are several areas that could be explored in future work to enhance the system further. Here are some recommendations for future research:

Scalability: Further investigation should be conducted to assess the scalability of the system. This includes evaluating its performance in scenarios with a large number of vehicles, as well as optimizing the system to handle increased traffic efficiently.

Integration with Smart Home Systems: The auto-opening gate system can be integrated with existing smart home systems to provide enhanced functionality. Future research could focus on developing interfaces and protocols for seamless integration, allowing users to control the gate system through voice commands or smartphone applications.

Advanced Security Measures: While our system incorporates several security features, there is always room for improvement. Future work could explore advanced encryption techniques, biometric authentication, or multi-factor authentication methods to further enhance the security of the system.

Environmental Considerations: The system's environmental impact should be taken into account. Future research could focus on optimizing power consumption, exploring alternative energy sources, or incorporating energy-saving features to reduce the system's ecological footprint.

Cost-Effectiveness: Investigate methods to reduce the overall cost of implementing the auto-opening gate and wireless identification system. This could involve exploring alternative technologies, improving manufacturing processes, or evaluating cost-effective alternatives for components without compromising functionality or security.

By addressing these recommendations, future research can contribute to the continuous improvement of auto-opening gate systems and vehicle wireless identification, making them more efficient, secure, and user-friendly. [13]

References

[1] Duhame, D.C. (1984) Home Security and Garage Door Operator System. ed: Google Patents.

[2] Duhame, D.C. (1982) Home Security and Garage Door Operator System. ed: Google Patents.

[3] Petersen, T., Williams, P. and Mills, A. (2001) Analysis of the Value of Home Automation Systems. Facilities

[4] Osadciw, L., Varshney, P. and Veeramachaneni, K. (2002) Improving Personal Identification Accuracy Using Multi Sensor Fusion for Building Access Control Application. In: Proceedings the Fifth International Conference for Information Fusion, 1176-1183.

[5] ADSL (2009) All Data Sheet Library. http://www.alldatasheet.com [7] Bluetooth Wireless Technology Basics.

[6] Al-Jamal, H., & Ayoub, A. (2020). Arduino-based Smart Gate Control System Using RFID Technology. International Journal of Scientific & Engineering Research, 11(3), 1072-1080.

[7] Arduino. (n.d.). Arduino Official Website. Retrieved from https://www.arduino.cc/

[8] Arduino. (n.d.). Retrieved from https://www.arduino.cc/

[9] Smith, J. K. (2018). Automatic Gate Opening Systems: A Review of Recent Developments.

International Journal of Automation and Control Engineering, 7(2), 101-114.

[10] Johnson, D. (2016). Programming Arduino: Getting Started with Sketches. McGraw-Hill Education

[11] IR Sensor Basics and Working. (2020, May 4). Electronics Hub. https://www.electronicshub.org/ir-sensor/

[12] Bluetooth Technology Website. (n.d.). Retrieved from https://www.bluetooth.com/

[13] Arduino Bluetooth Basics: Building an IoT Door Lock. (2018, April 11). Circuit Digest.

https://circuitdigest.com/microcontroller-projects/arduino-bluetooth-basics-building-an-iot-door-lock

AL-IRAQIA UNIVERSITY - COLLEGE OF ENGINEERING-

DEPARTMENT OF ELECTRICAL ENGINEERING

Reliability of generating unit's assessment in presence of p.v systems

Supervised by

Dr. Hussein Jumma

Prepared by

Ameer hassan Mohammed

Ahmed salman sahel

Ali amer shatan

Mardan Khairallah mussa

Project submitted in fulfilment of the requirements for the degree of Bachelor of engineering science

May 2023

ACKNOWLEDGEMENT

In the name of Allah, the most gracious, the most merciful. First, I would like to thank and praise almighty Allah from the depths of my heart, for giving me the opportunity to pursue Bachelor degree study in Al-Iraqia University and providing me with the ability and patience upon facing difficulties during all this time. We offer my sincerest gratitude to my supervisor, Dr. Hussein Jumma, who has guided and supported us with his patience and knowledge throughout our research. We attribute our accomplishment to his encouragement, patience and effort, without him this project would not have been completed. One simply could not wish for a better and friendlier supervisor as he is. His suggestions and advices had helped us in our times of despair when our research was facing some problems. We would like to extend our gratitude to our family members who always support us and pray for us to complete our project. Our appreciation also goes to the Electrical Engineering department, for giving us the opportunity to further our studies.

ABSTRACT

Electricity demand has grown over the past few years and will continue to grow in the future. The increase in electricity demand is mainly due to industrialization and the shift from a conventional to a smart-grid paradigm. The number of microgrids, renewable energy sources, plug-in electric vehicles and energy storage systems have also risen in recent years. As a result, future electricity grids have to be revamped and adapt to increasing load levels. Thus, new complications associated with future electrical power systems and technologies must be considered. PV application offer promising solutions to these issues and can considerably improve the reliability and financial performances of electrical power systems. This project presents PV model in reliability framework of electrical power systems. A PV is widely implemented in electrical power generation due to its considerable impact on system reliability and efficiency. The findings from this project show that the proposed PV model can perform better than original case without this model .The sequential Monte Carlo simulation (MCS) was implemented in this project. IEEE-reliability test system (RTS) has been conducted in this project.

CHAPTER ONE

INTRODUCTION

1.1 Background

The dwindling number of conventional power resources and its environmental impact has motivated a transition to renewable energy sources, such as solar power. In the past few decades, the demand for renewable energy sources has grown steadily partly due to the dwindling fossil fuel supply and the growing energy demand; however, the most important driver of this growth lies in the people's increasing awareness of environmental conservation initiatives [1]. Amongst all possible renewable energy sources, solar power is considered the most advanced and most suitable resource for large-scale electricity generation despite its intermittent nature, which, at the moment, is addressed by using energy storage [2]. Evaluating the reliability of solar power integration into power networks can help decision makers gauge the feasibility of their solar power projects[3]. However, the stochastic and non-stationary nature of solar radiation is difficult to be modeled and can even hinder an accurate evaluation of reliability. A good solar model for accurately assessing solar-power integrated systems should be able to retain the original statistical properties of the sampled solar radiation data. Therefore, this project aims to model an easy-to-use simulating solar radiation.

1.2 Power Systems Reliability

Power system planners attempt to design a reasonable level of reliability at an acceptable initial and running cost. The reliability of power systems is a measure of the overall ability of the system to achieve its basic function. System reliability is divided into two: system adequacy and system security. Adequacy refers to the existence of sufficient facilities to meet the consumer demand. These facilities involve the generators to generate sufficient energy, the associated transmission lines to transmit the required energy to the distribution systems and the distribution networks to transport the energy to customers. Therefore, system adequacy does not include system disturbances. The electric utility industry is obligated to supply efficient and reliable electric services to customers as economically as possible [4]. However, it is unpractical to design and construct fully reliable electrical power systems. Security

relates to the ability of the system to respond to disturbances. HL1 involves the analysis of the generation facility, HL2 considers the analysis of the generation and transmission facilities and HL3 considers the analysis of an additional distribution facility. Only HL1 and HL2 studies are regularly performed given that complete HL3 studies are highly complex because of their large problem scale. Thus, the distribution network is normally analysed individually and separately from the generation and transmission systems. Electrical power reliability is usually calculated in terms of certain reliability indices. These are usually measured to evaluate the level of reliability worth and cost at specific zone in electrical power systems, therefore, it is significant to tabulate these indices as in Appendix A [3]. HLI reliability assessment is defined as generating capacity adequacy evaluation. One of the power system reliability investigation studies is the generating systems adequacy study and it is concerned only with the ability to satisfy customer demand [3]. Generating systems adequacy is the ability of generation systems to provide a sufficient and continuous supply of electricity to the users' demands. The ability of transmission and distribution system to move the supplied energy to the end-user is neglected in HLI assessment. In this study, transmission and distribution systems are not considered and assumed fully reliable. Thus, this project focuses on the HLI assessment. Generating capacity adequacy assessment is usually performed by using two, three and four-state model. In two-state model, all generation units transit only between up and down states regardless of the types of generators. The three-state model takes the partial outage of the large thermal generation units into account. Four-state model is properly used to model peaking and cycling generation units. Expected values based on probabilistic assessment are used to assess the level of adequacy, namely loss of load expectation (LOLE), expected energy not-supplied (EENS), loss of load frequency (LOLF) and loss of load duration (LOLD).

1.2 Problem Statement and Project Gap

The conventional generation systems (i.e. thermal and nuclear) have a high production cost and are unclean. Photovoltaic (PV) systems are clean , silent, free maintenance , efficient and reliable source of energy. The objective of this project is to model PV energy systems in reliability framework by using Matlab and then to assess EENS for each case study. The main aim of this project is to decrease the pollution and

production cost of electricity. Solar energy is one of the most eco-friendly and cheapest source of energy. Solar power can contribute considerably to a sustainable electricity supply of world and to a reduction of CO2 emissions and to enhance reliability of supply if integrated with other techniques. The conventional generation systems (i.e. thermal and nuclear) have a high production cost and are unclean. photovoltaic (PV) systems are clean , silent, free maintenance , efficient and reliable source of energy. Renewable energies (RES) have a high uncertainty and are unpredictable source of energy and to model PV energy systems in reliability.

The scope of the project concentrates exclusively on the generating capacity adequacy (or HLI) assessment incorporating with selected PV models. Probabilistic approach is used by utilising sequential Monte Carlo simulation (MCS) to calculate reliability indices. The system risk model is acquired by combining the generation model with the load model. Thus, risk indices are obtained. Sequential MCS simulates the actual process and the random behaviour of the generation systems in HLI assessment. The reliability indices are obtained by combining the load model with the generation model and then to find power inadequacy in terms of energy amount per each interruption.

1.3 Aim and Objectives

This Project serves to establish power system reliability of hierarchical level 1 (HL1) using MCS technique. The IEEE Reliability Test System (IEEE-RTS) generation model and load model are applied to convolute a system risk model. The project contribution are :-

1. Incorporating PV improves system reliability but the variability of PV power output compromises on PV capacity credit.
2. System adequacy index(EENS) is investigated to show the system reliability performance. Impact on system reliability of generation units , via variation of PV and ES capacities are presented.
3. Actual Iraqi PV irradiance data is incorporated in this study. This analytical technique can help Iraqis energy supplier to evaluate the potential of PV to benefit system reliability and find ways to improve its potentials.

1.4 Project Structure

In accordance with the aforementioned objectives, the project is structured as fouyr chapters, which are summarised as follows: Chapter 1 gives a general overview of the background of the work. Chapter 2 presents literature review. Chapter 3 introduces the methodology. Chapter 4 gives the result and the main conclusions of this project.

CHAPTER TWO

LITERATURE REVIEW

2.1 Introduction

Renewable energy sources (RES) are stochastic in nature, intermittent, unpredictable and uncontrollable. Despite this, they remain crucial sources for a sustainable future grid.

Table 1 Summary of comparison on the PV impact on HL1

Sources	DSM programme	Additive model	Reliability indices	Test system
[5]	DLC, PLS	ESS	LOLE	IEEE-RTS
[6]	DLC, PLS	ESS,RES	EENS	IEEE-RTS
[7]	RTP, PC	Smart metering	LOLE,EENS	IEEE-RTS
[8]	CLP, PC	ESS	LOLE,LOLD, LOLF,EENS	IEEE-RTS
[9]	CLP, PC	UC	VOLL	synthetic systems
[10]	ILs	RES	EENS	IEEE-RTS
[11]	EDRPs	RES and LFU	LOLE,EENS	IEEE-RBTS
[12]	=	DTR, RES	EENS, EFLC,EDLC	IEEE-RTS

From Table 1 , it appears that researchers have adopted a certain basis for scientific research. For example, DLC programmes were frequently used in HL1 reliability assessment since the distribution systems and transmission liens are assumed fully reliable. Since EENS has the longest convergence time among the other reliability indices, it has been used widely in HL1 reliability assessment to determine the reliability performance in term of energy. It should also be noted that LOLE has been considerably used because this index reflects the inadequacy duration. In this regards, IEEE-RTS is extensively used to calculate the well-known reliability indices.

CHAPTER THREE

METHODOLOGY

2.2 Background

The generation systems have 32 generators with a maximum capacity of 3405 MW that is serving 2850 MW of annual peak load. The generating system model of IEEE-RTS consists of 8736 load data points. IEEE-RTS data are shown in Appendix B. IEEE-RTS schematic diagram is shown in Figure 3.1. Sequential MCS is performed due to chronological load model to calculate the reliability indices of the generation systems. MATLAB software is used for system modelling and simulation. The sampling size is 3000 iterations in this study. As it was observed that all the simulations converged at around the 2500th iteration, choosing 3000 iterations provided a conservative approach to ensure an adequate number of simulations has been performed to guarantee convergence. The hourly load profile and generation systems of the IEEE-RTS are adopted [13, 14]. This section gives a data analysis and background of the IEEE-RTS, showing the assumptions in this study, energy supplied and unsupplied, priority order and capacity limits for each type of generation units. Within a day, 1-16 hours are considered on-peak hours, while 17– 24 hours are considered off-peak hours. The probability of start-up failure of peaking and cycling generation units is assumed to be 0.03 [3]. The maximum range of LFU is considered 15% [15]. Each generation unit is of different type, capacity, size and failure rate. Therefore, each generation unit has its own unique operating requirements. Since the loading order of the generating units has a large impact on the system production costs, priority list method is used for minimising production cost [16].

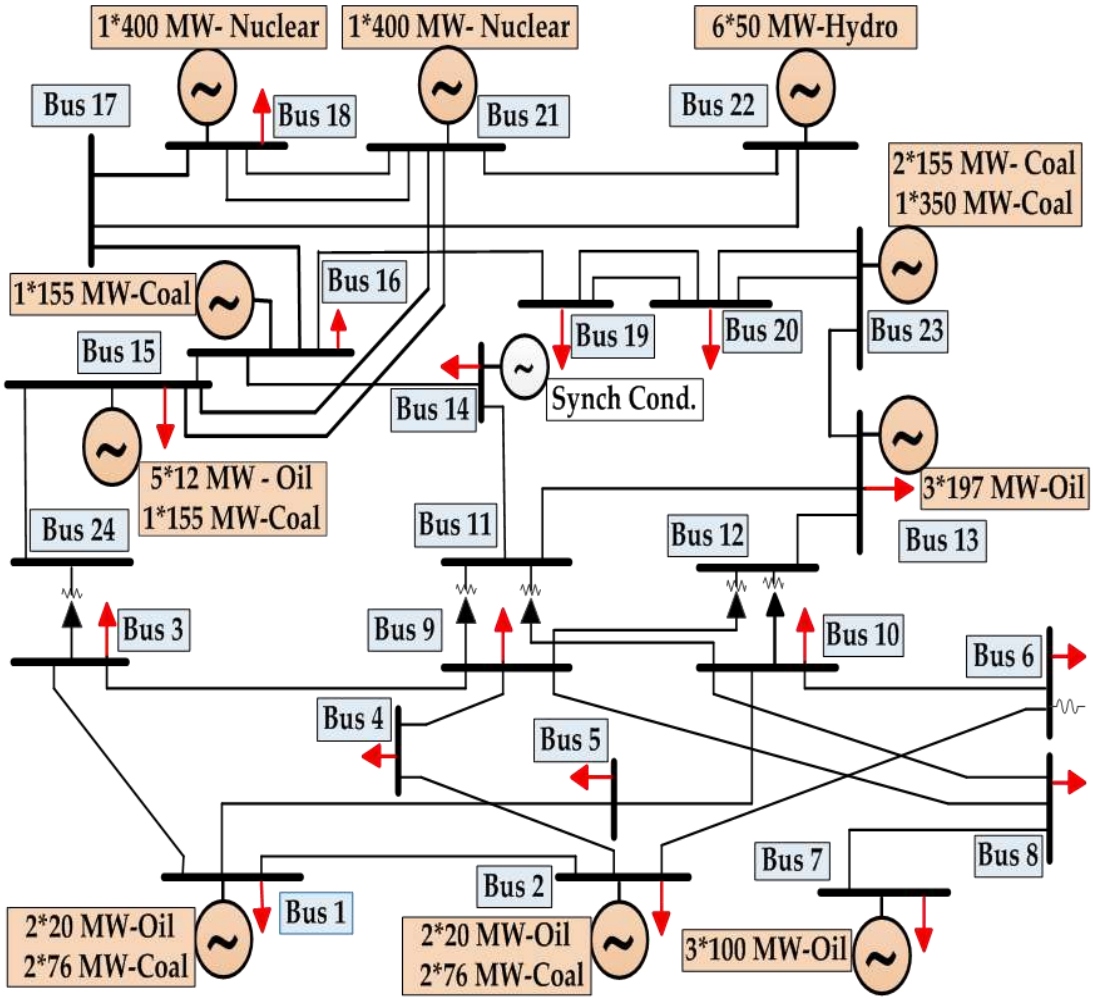

Figure 3.1 IEEE-RTS schematic diagram [13, 14]

2.3 Methodology

The system risk model is acquired by combining the generation model with the load model. Then, risk indices are obtained such as LOLE, EENS, LOLF and LOLD. The analytical method and the simulation method are used to assess risk indices. Sequential MCS is used to assess reliability indices. Sequential MCS simulates the actual process and the random behaviour of the generation systems in HLI assessment. The reliability indices are obtained by combining the load curve with the total available capacity of generation units and then to find power inadequacy in terms of energy, duration, frequency and duration per each interruption. Figure 3.2 shows the combination of the original load curve and the total available capacity of generation units.

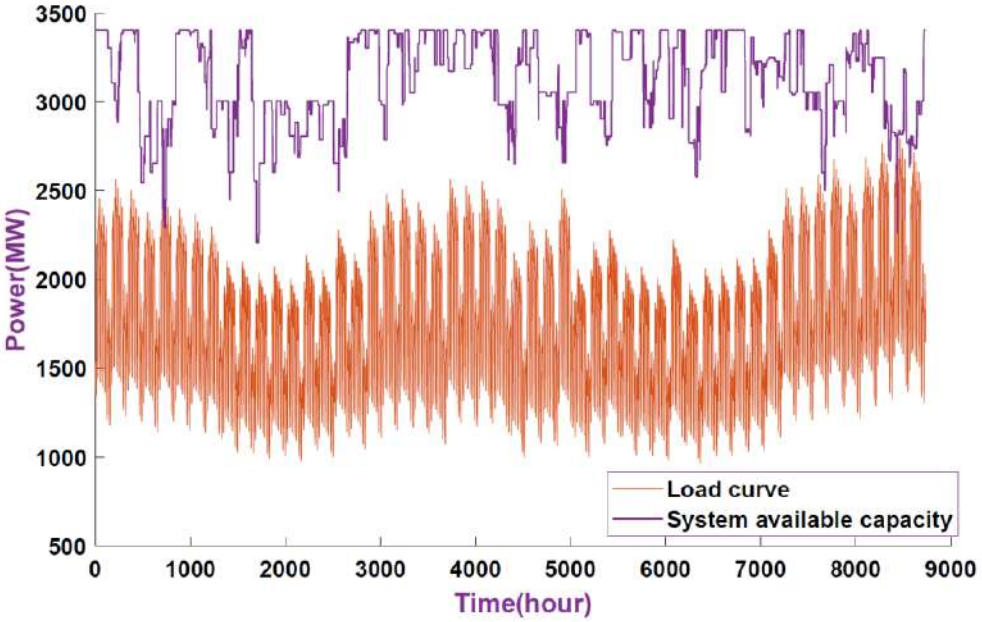

2.4 Model of HLI

The methodologies for generating capacity adequacy assessment to adequacy studies of power systems using an operating consideration has been used . HLI reliability evaluation is the process of total generating systems adequacy assessment to meet the system demand requirement [3, 4] . The main objective of generating capacity adequacy evaluation is to assess the system reserve required to meet the system load. This evaluation is divided into two different aspects called static and operating adequacy evaluation. Static evaluation is the long-term planning requirement to meet the load. Operating capacity evaluation deals with short-term of the capacity requirement to meet the demand [3, 4]. This project deals with static aspects. Generating capacity adequacy assessment involves the generation model, load model. The combination of these two models produces a risk model. Load can be modelled in different ways to depict the demand throughout a specific period. Hourly load data can be modelled chronologically. A chronological load model is obtained from the available hourly data. The load $L(t)$ for hour t can be acquired by this equation [3, 4]:-

$$L(t) = L_w \times L_d \times L_h \tag{3.1}$$

Where L_w is the percentage of the weekly load in terms of the annual peak, L_d is the percentage of the daily load in terms of the weekly peak load and L_h is the percentage of the hourly load in terms of the daily peak. The annual hourly load model is obtained by acquiring 24-hour load profile, daily percentage, weekly percentage and the annual

peak load. This load model is implemented. Figure 3.8 shows the chronological hourly load model for the IEEE-RTS.

2.4.1 Available Capacity of Generation Units Using Monte Carlo Simulation

The major focus of this project is to develop generating system adequacy assessment model for power systems incorporating load shifting technique. Generating system adequacy assessment can be achieved using either a probabilistic or a deterministic approach. Deterministic methods are gradually being changed by probabilistic methods due to their ability to reflect the actual risk of the corresponding systems. Probabilistic approach is used in this project by implementing sequential MCS [3, 4]. Stochastic simulation includes a large number of time dependent random variables. However, this issue has been resolved with the improvements in digital computers. MCS can be generally divided into two approaches, namely, non-sequential and sequential approaches [3, 4]. In non-sequential MCS, the system states are randomly simulated. In sequential MCS, the chronological behaviour of the system is sampled by simulating sequences of system states for several periods. Sequential MCS is used to estimate the risk indices by simulating the random behaviour of the generation units. The sequential MCS method is utilized in this project. Risk model is formed by superimposing the chronological load model on total system available capacity. Operational history for each single generation unit is performed in the form of mean times to repair (MTTR) and generating unit mean times to failure (MTTF). These two parameters are taken as the reciprocal of the repair and failure rates, respectively as shown in Equations (2.3) and (3.3) [3, 4]. Random numbers, which are between 0 and 1, are used in conjunction with MTTR and MTTF to form a state history of each generator. State history of each generator consists of a series of random up-down-up or up-derated-down-up times. The state residence time for each generator is sampled according to a certain probability distribution. In this project , the relevant distributions are assumed to be exponential. Then, the random values of time-to-failure (TTF) and time-to-repair (TTR) are obtained from Equations (4.3) and (5.3) [3, 4].

$$TTF = -MTTF In\ U \quad 3.2$$

$$TTR = -MTTR\ In\ U \quad 3.3$$

$$MTTR = 1/\mu \quad 3.4$$

$$MTTF = 1/\lambda \qquad 3.5$$

Where U is the uniformly distributed random number between [0,1], λ is the failure rate, and μ is the repair rate. The process of assessing the total available capacity of all generation units can be briefly described as follows:

1. Simulate the available capacity for each generation unit by accumulating all operating history of available capacity for each generation units in the form of chronological up-derated-down-up or up-down-up operating cycles as shown in Figures 3.10 and 3.11.
2. Obtain the system available capacity for the simulated year by combining the operating cycles of all the generating units in the system. Figure 3.12 shows the total system available capacity for two units.

2.4.2 Risk Model

The generation and load models are both superimposed to produce the risk model or the system available margin model. A positive margin refers that the supplied energy is adequate to satisfy the system demand. A negative margin denotes that the system generation is insufficient and thus system demand has to be shed. The next step is to calculate appropriate reliability indices that can be used to describe the HLI reliability evaluation of the power system. EENS depicts the average amount of load loss due to generating inadequacy [3]. In each sampled year, e.g. in year *i,* loss of load duration (LLD_i) in hours, the loss of load occurrence (LLO_i), and the energy not supplied (ENS_i) in MWh are obtained from the available margin model. The reliability indices in s sampling years therefore can be calculated using the following equations [3, 4]:

$$EENS = \frac{\sum_{i=1}^{s} ENS_i}{s} \quad \text{(MWh/year)} \qquad 3.6$$

2.4.3 MODELING OF THE SUN POSITION

As a fact, the Earth rotates around the Sun in an elliptical orbit. Figure 1.1 shows the Earth rotation orbit around the Sun. The length of each rotation the Earth makes around the Sun is about 8766 h, which approximately stands for 365.242 days. From the figure, it can be seen that there are some unique points at this orbit. The winter

solstice occurs on December 21, at which the Earth is about 147million km away from the Sun. On the other hand, at the summer solstice, which occurs on June 21, the Earth is about 152million km from the Sun. However, to provide more accurate points, the Earth is closest to the Sun (147million km) on January 2, and this point is called perihelion. The point where the Earth is furthest from the Sun (152million km) is called aphelion and occurs on July 3. For an observer standing at specific point on the Earth, the Sun position can be determined by two main angles, namely, altitude angle (A) and azimuth angle (θ_s), as seen in Figure 1.2

From Figure 1.2 THE ALTITUDE ANGLE IS THE ANGULAR HEIGHT OF THE SUN IN THE SKY MEASURED FROM THE HORIZONTAL. THE ALTITUDE ANGLE CAN BY

$$\mathrm{SIN\,A} = \mathrm{SIN\,L\,SIN\,\Delta} + \mathrm{COS\,L\,COS\,\Delta\,COS\,\Omega} \qquad (3.7)$$

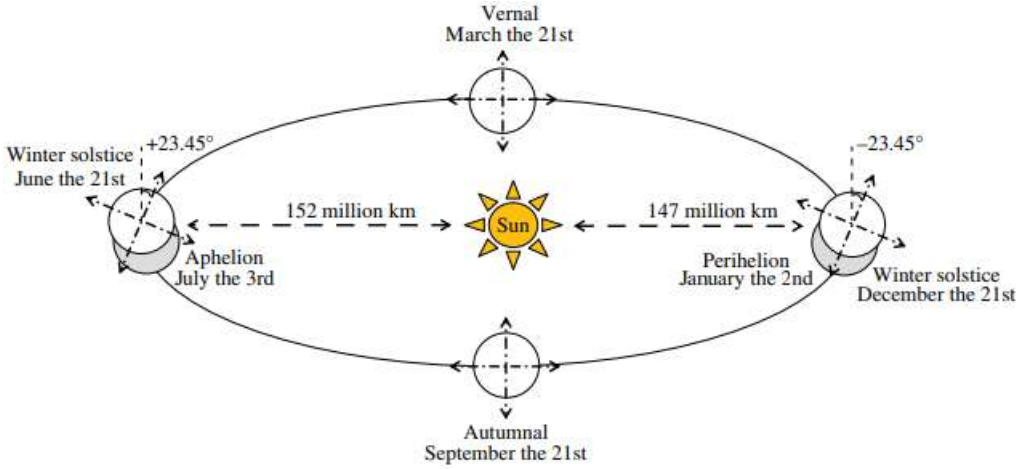

FIGURE 1.1 Earth rotation orbit around the Sun.

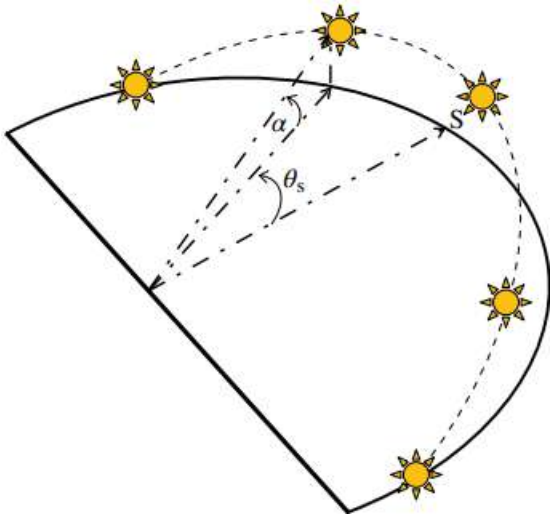

FIGURE 1.2 The Sun's altitude and azimuth angles.

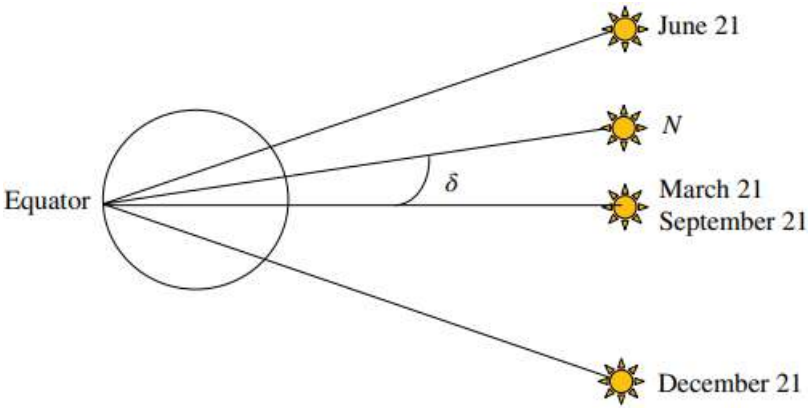

FIGURE 1.3 Solar declination angle.

The angle of declination is the angle between the Earth–Sun vector and the equatorial plane (see Fig. 1.3) and is calculated as follows (results in degree, arguments to tragicomic functions are expected to be in radiant):

$$\sigma_s = 23.45° \sin\left[\frac{2\pi(N-81)}{365}\right] \qquad (3.8)$$

The hour angle, ω, is the angular displacement of the Sun from the local point, and it is given by

$$\omega = 15°(\mathrm{AST} - 12\mathrm{h}) \qquad (3.9)$$

between two successive returns of the Sun to the local meridian. Apparent solar time is given by

$$\mathrm{AST} = \mathrm{LMT} + \mathrm{EoT} \pm 4^\circ /(\mathrm{LSMT} - \mathrm{LOD}) \quad (3.10)$$

The LSMT is a reference meridian used for a particular time zone and is similar to the prime meridian, used for Greenwich Mean Time. LSMT is given by

$$\mathrm{LMST} = 15^\circ T_{\mathrm{GMT}} \quad (3.11)$$

The EoT is the difference between apparent and mean solar times, both taken at a given longitude at the same real instant of time. EoT is given by

$$\mathrm{EoT} = 9.87 \sin(2B) - 7.53 \cos B - 1.5 \sin B \quad (3.12)$$

where B can be calculated by

$$B = \frac{2\pi}{365}(N - 81) \quad (3.13)$$

On the other hand, the azimuth angle as can be seen in Figure 1.2 is an angular displacement of the Sun reference line from the source axis. The azimuth angle can be calculated by

$$\mathrm{SIN}\,\Theta = \frac{\mathrm{COS}\,\Delta\,\mathrm{SIN}\,\Omega}{\mathrm{SIN}\,\mathrm{A}} \quad (3.14)$$

```
%Modeling of PV systems using MATLAB

%Chapter I

%Example 1.1

%------------------------------------------------------------

%date 1/5/2023  (N=120)
```

```
%location Iraq , Baghdad , L =(33.12), LOD = (44.7)

L=33.12 ; %Latitude

LOD=44.7 ; %longitude

N=120;  %Day Number

T_GMT=3;  %Time difference with reference to GMT

LMT_minutes=720;  %LMT in minutes

Ds=23.45*sin((360*(N-81)/365)*(pi/180)); % angle of declination

B=(360*(N-81))/364;   %Equation of Time

EoT=(9.87*sin(2*B*pi/180))-                    (7.53*cos(B*pi/180))-
(1.5*sin(B*pi/180)); % Equation of Time

Lzt= 15* T_GMT; %LMST

if LOD>=0

Ts_correction= (-4*(Lzt-LOD))+EoT; %solar time correction

else

Ts_correction= (4*(Lzt-LOD))+EoT; %solar time correction

end

Ts= LMT_minutes + Ts_correction; %solar time

Hs=(15 *(Ts - (12*60)))/60; %Hour angle degree

sin_Alpha=(sin(L*pi/180)*sin(Ds*pi/180))+(cos(L*pi/180)*cos(Ds*pi/
180)* cos(Hs*pi/180)); %altitude angle

Alpha_i=asind(sin_Alpha)   %altitude angle

Sin_Theta=                    (cos                    (Ds*pi/180)*sin
(Hs*pi/180))./cos(Alpha_i.*pi/180); %Azimuth angle

Theta=asind(Sin_Theta) %Azimuth angle
```

ANS:

Alpha_i =

33.0350

Theta =

-1.3100

The solar day is defined as the duration from sunrise to sunset. Thus, the altitude and azimuth angles are required to be calculated for each hour from sunrise to sunset. The sunrise and sunset hour angles can be considered equal and calculated as

$$\Omega_{SS.SR} = \cos^{-1}(-\tan L \ \tan \Delta) \qquad (3.15)$$

In the meanwhile, the solar time of each hour angle can be calculated by rewriting Equations 1.3 as follows:

$$\frac{\Omega_{SR.SS}}{15^\circ} \pm 12H = AST_{SR.SS} \qquad (3.16)$$

The sign of Equation 1.10 must be minus if we want to calculate the sunrise time, while it must be plus if we are calculating the sunset time. Following that the main parts of the program's structure can be described as follows:

• Insert location coordinates (latitude and longitude) and day number.

• Calculate angle of declination.

• Calculate sunrise and sunset hour angles.

• Calculate AST of the sunrise and sunset.

• Calculate equation of time and LMST.

• Calculate the actual sunrise and sunset times.

• Set for a loop starting from the sunrise and terminating by the sunset with a step size of 5min.

• Calculate the solar time and hour angle at each step.

• Calculate altitude angle at each step.

• Calculate azimuth angle at each step.

• Store the calculated altitude and azimuth angles in arrays.

• Plot the results.

```
%Modeling of PV systems using MATLAB
%-----------------------------------------------------------
%date 1/5/2023  (N=120)
%location Iraq , Baghdad , L =(33.12), LOD = (44.7)
%Actual solar day time 07:11  to 19:22
L=33.12; %altitude
LOD=44.7 ; %longitude
N=120;  %Day Number
T_GMT=3;  %Time difference with reference to GMT
Step=5;
Ds=23.45*sin((360*(N-81)/365)*(pi/180)); % angle of declination
Lzt= 15* T_GMT; %LMST
```

```
  B=(360*(N-81))/364;   %Equation of Time

  EoT=(9.87*sin(2*B*pi/180))-                    (7.53*cos(B*pi/180))-
(1.5*sin(B*pi/180));   %Equation of Time

  if LOD>=0

  Ts_correction= (-4*(Lzt-LOD))+EoT; %solar time correction

  else

  Ts_correction= (4*(Lzt-LOD))+EoT; %solar time correction

  end

  Wsr_ssi=- tan(Ds*pi/180)*tan(L*pi/180);%Sunrise/Sunset hour angle

  Wsrsr_ss=acosd(Wsr_ssi);% Sunrise/Sunset hour angle

  ASTsr=abs((((Wsrsr_ss/15)-12)*60));%Sunrise solar time

  ASTss=(((Wsrsr_ss/15)+12)*60);%Sunset solar time

  Tsr=ASTsr+abs(Ts_correction);  %Sunrise local time

  Tss=ASTss+abs(Ts_correction);   %Sunset local time

  Alpha=[];

  Theta=[];

  for LMT=Tsr:Step:Tss  %for loop for the day time

  Ts= LMT + Ts_correction; % solar time at each step

  Hs=(15 *(Ts - (12*60)))/60; % Hour angle degree at each step

  sin_Alpha=(sin(L*pi/180)*sin(Ds*pi/180))+(cos(L*pi/180)*cos(Ds*pi/
180)* cos(Hs*pi/180)); %altitude angle

  Alpha_i=asind(sin_Alpha) ;  %altitude angle

  Alpha=[Alpha;Alpha_i];%store altitude angle in array
```

```
  Sin_Theta=                    (cos                    (Ds*pi/180)*sin
(Hs*pi/180))./cos(Alpha_i.*pi/180);%Azimuth angle

  Theta_i=asind(Sin_Theta);%Azimuth angle

  Theta=[Theta;Theta_i];% store azimuth angle in array

  end

   Alpha;

   Theta;

  subplot(2,1,1)%plot results

  plot(Alpha)

  subplot(2,1,2)

  plot (Theta, 'red')
```

ans:

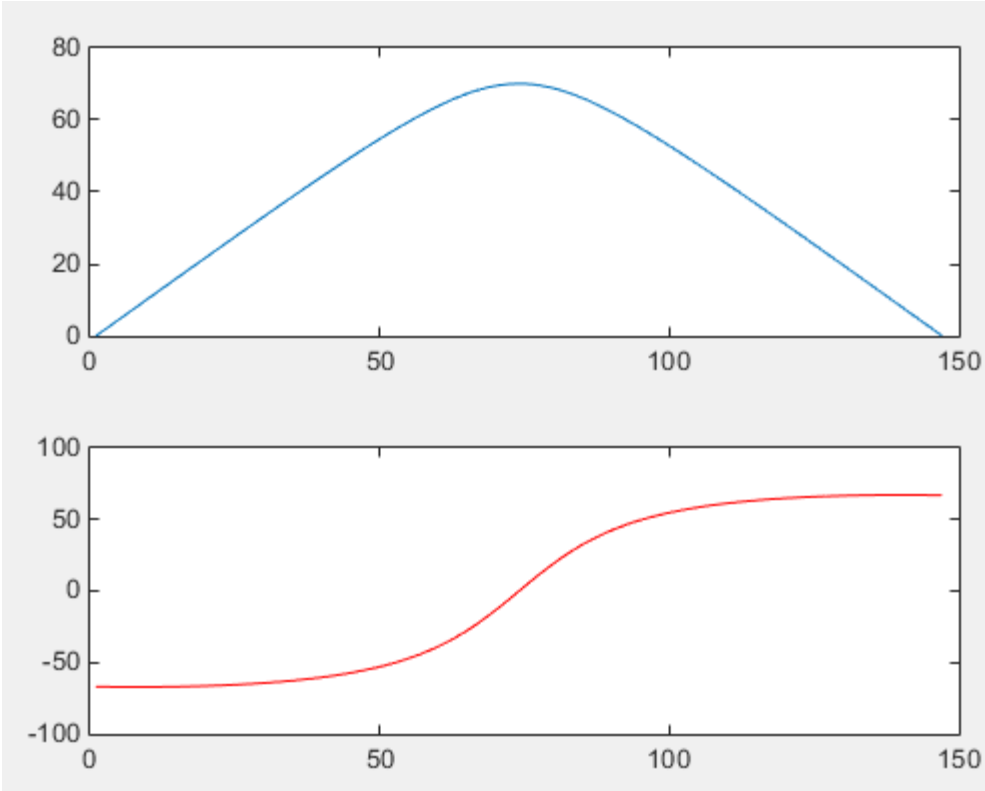

MODELING OF EXTRATERRESTRIAL SOLAR RADIATION

The first step in modelling the solar source is to estimate the emitted radiation from the Sun. As a fact, the radiant energy of any emitting object can be described as a function of its temperature. The usual practice to estimate the radiant energy by an object is to compare it to a blackbody. A blackbody is defined as a perfect emitter and absorber. A perfect absorber can absorb all of the received energy with any reflections, while a perfect emitter emits energy more than any other object. Planck's law describes the wavelengths emitted by a blackbody at a specific temperature as follows:

$$E_{\Lambda} = \frac{3.74\times10^{8}}{\Lambda^{5}\left[\mathrm{EXP}\frac{14.400}{\Lambda T}\right]-1} \qquad (3.17)$$

where E_{Λ} is the total emissive per unit area of blackbody emission rate (W/m^2µm), T is the absolute temperature of the blackbody (K), and λ is the wavelength (µm).

```
T=288;

E_lamda=[];

for lamda=1:1:60;

E_lamda_i= (3.74*10e8)/(lamda^5*(exp(14400/(lamda*T))-1));

E_lamda=[E_lamda; E_lamda_i];

end

E_lamda
```

```
lamda=1:1:60;

plot(lamda,E_lamda)
```

ans:

```
E_lamda                                                                =
```

0.0000	0.0016	0.8893	13.6111	54.3371	115.6376	176.0441	220.7600	245.8069
253.7087	249.1593	236.6960	219.8717	201.1709	182.1978	163.9136	146.8420	
131.2243	117.1275	104.5160	93.2988	83.3581	74.5674	66.8015	59.9425	53.8822
48.5231	43.7788	39.5730	35.8388	32.5179	29.5594	26.9191	24.5584	22.4439
20.5464	18.8407	17.3045	15.9185	14.6660	13.5321	12.5039	11.5700	10.7204
9.9463	9.2399	8.5943	8.0035	7.4620	6.9651	6.5084	6.0882	5.7011
5.3439	5.0141	4.7091	4.4268	4.1651	3.9224	3.6970		

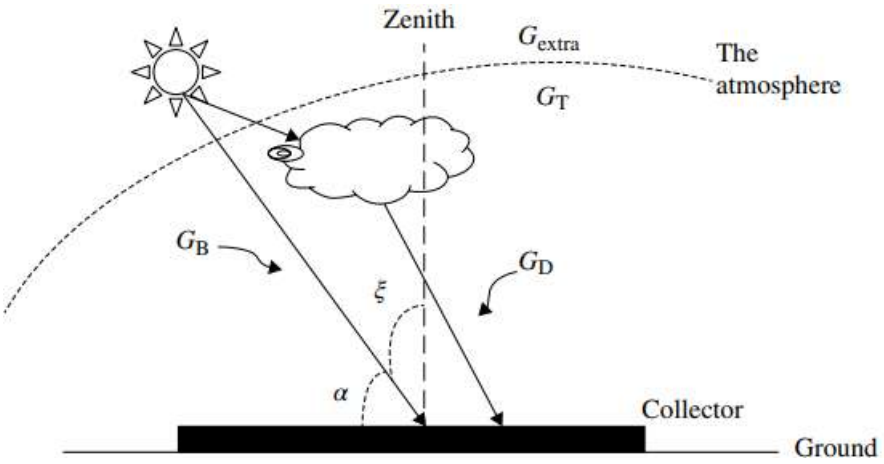

In order to calculate the emitted power between the wavelength value of 20 and 30μm, the shaded area in Figure 1.5 can be calculated as follows:

$$\sum_{\Lambda=20}^{\Lambda=30} E_{\Lambda} = \sum_{\Lambda=20}^{\Lambda=30} \frac{3.74\times10^{8}}{\Lambda^{5}\left[\mathrm{EXP}\frac{14.400}{\Lambda T}\right]-1} \quad (3.18)$$

Solar radiation value outside the atmosphere varies as the Earth orbits the Sun. Therefore, the distance between the Sun and the Earth must be considered in modelling the extra-terrestrial solar radiation. Thus, the extra-terrestrial radiation (G_{EX}) is given by

$$G_{EX} = G_O \left(\frac{R_{AV}}{R}\right)^2 \quad (3.19)$$

where R_{AV} is the mean distance between the Sun and the Earth and R is the instantaneous distance between the Sun and the Earth. The instantaneous distance between the Sun and the Earth depends on the day of the year or day number. In fact there are different approximations for the factor (R_{AV}/R) in the literature. A recommended approximation can be given by

$$\left(\frac{R_{AV}}{R}\right) = 1 + 0.0333 \, COS\left(\frac{2\Pi N}{365}\right) \quad (3.20)$$

By substituting Equation 1.14 in Equation 1.13, the extra-terrestrial solar radiation unit of time falling at a right on square meter of a surface can be given by

$$G_{EX} = G_O \left(1 + 0.0333 \, COS\left(\frac{2\Pi N}{365}\right)\right) \quad (3.21)$$

the extra-terrestrial solar radiation on a horizontal surface located in a specific location (G_{EXH}) can be calculated by

$$G_{EXH} = G_{EX} \, COS \, \Phi \quad (3.22)$$

where ϕ is the solar zenith angle, which is measured from directly overhead to the geometric center of the Sun's disc. The solar zenith angle value is equal to the altitude value, and thus Equation 1.16 can be rewritten as follows:

$$G_{EXH} = G_O \left(1 + 0.0333 \, COS\left(\frac{360N}{365}\right)\right) SIN \, L \, SIN \, \Delta + COS \, L \, COS \, \Delta \, COS \, \Omega \quad (3.23)$$

the total extra terrestrial solar energy (E_{EX}) (Wh/m^2) is calculated as follows:

$$E_{EX} = \int_{T_{SR}}^{T_{SS}} G_{EXH} DT \qquad (3.24)$$

```
%Modeling of PV systems using MATLAB

%-------------------------------------------------------

%date 1/5/2023  (N=120)

%location Iraq , Baghdad , L =(33.12), LOD = (44.7)

%Actual solar day time 07:11  to 19:22

L=33.12; %altitude

LOD=44.7 ; %longitude

N=120;  %Day Number

T_GMT=3;  %Time difference with reference to GMT

Step=60;  %step each hour

Ds=23.45*sin((360*(N-81)/365)*(pi/180)); % angle of declination

B=(360*(N-81))/364;   %Equation of time

EoT=(9.87*sin(2*B*pi/180))-                    (7.53*cos(B*pi/180))-
(1.5*sin(B*pi/180));   %Equation of time

Lzt= 15* T_GMT; %LMST

if LOD>=0

Ts_correction= (-4*(Lzt-LOD))+EoT; %solar time correction

else

Ts_correction= (4*(Lzt-LOD))+EoT; %solar time correction
```

```
end

Wsr_ssi=- tan(Ds*pi/180)*tan(L*pi/180); %Sunrise/Sunset hour angle

Wsrsr_ss=acosd(Wsr_ssi); %Sunrise/Sunset hour angle

ASTsr=abs((((Wsrsr_ss/15)-12)*60)); %Sunrise solar time

ASTss=(((Wsrsr_ss/15)+12)*60); %Sunset solar time Tsr=ASTsr+

abs(Ts_correction) %Actual Sunrise time

Tss=ASTss+abs(Ts_correction) %Actual Sunset time

sin_Alpha=[];

for LMT=Tsr:Step:Tss  %for loop for the day time

Ts= LMT + Ts_correction; %solar time at each step

Hs=(15 *(Ts - (12*60)))/60; %hour angle at each step

sin_Alpha_i=(sin(L*pi/180)*sin(Ds*pi/180))+(cos(L*pi/180)*cos(Ds*p
i/180)* cos(Hs*pi/180));  %altitude angle

sin_Alpha=[sin_Alpha;sin_Alpha_i]; % store altitude angle results

end

LMT=Tsr:Step:Tss

sin_Alpha;

Go=1367;  %solar constant

Gext=Go*(1+(0.0333*cos(360*N/365))); %available Gext

GextH=Gext*sin_Alpha; %Gex on horizontal surface

plot(LMT,GextH) %plot results
```

ANS:

43.578

TSS=

1.1372E+03

LMT =

1.0E+03

0.4316 0.4916 0.5516 0.6116 0.6716 0.7316 0.7916 0.8516 0.9116 0.9716 1.0316 1.0916

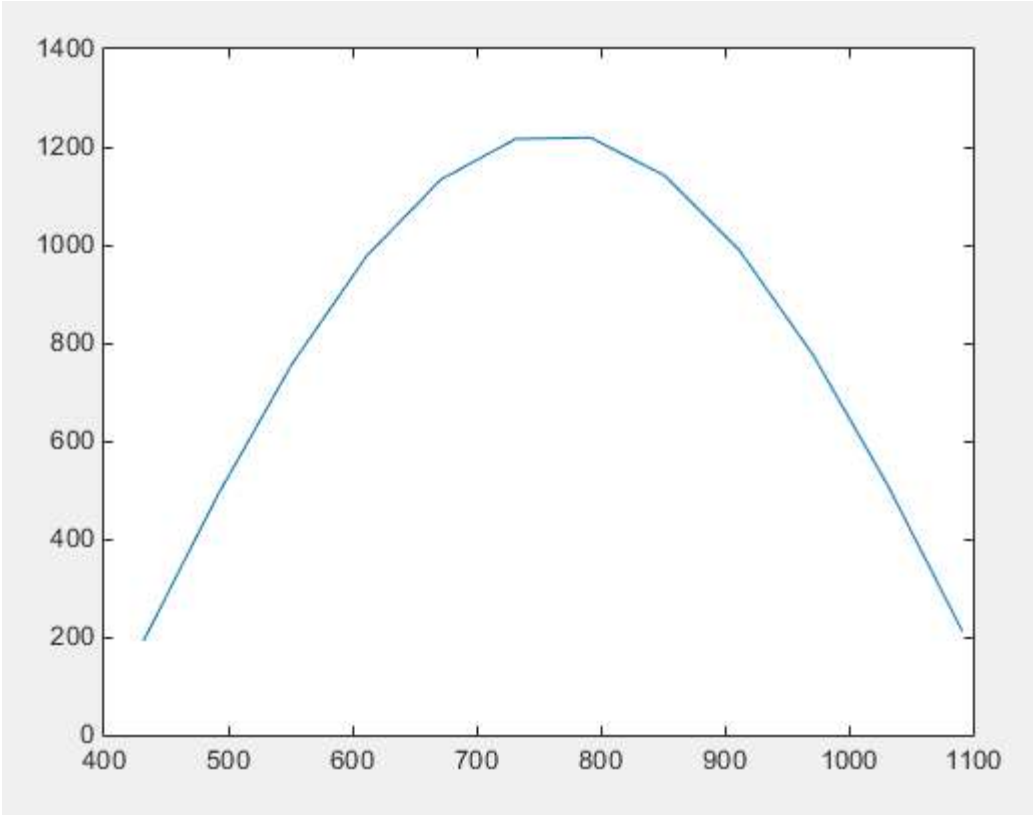

ENERGY FLOW MODELING FOR STAND-ALONE PV POWER SYSTEMS

Modelling of stand-alone PV systems (SAPV) is very important in sizing system's energy sources. Figure 4.1 shows a typical PV system consisting of a PV module/ array, power conditioner such as charge controller or maximum power point tracking

(MPPT) controller, batteries, inverter, and load. In general, a PV array collects energy form the sun and converts it to DC current. The DC current flows through a power conditioner to supply the load through an inverter. The daily output power produced by a PV module/array is given by

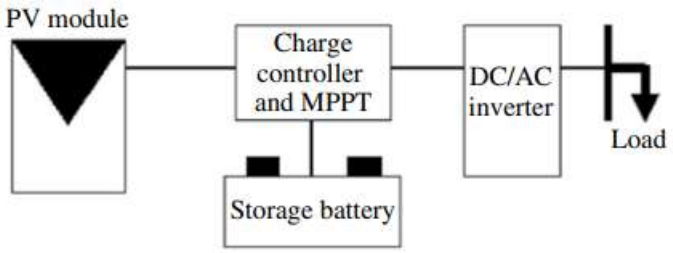

Figure 4.1 Typical PV system components.

Section 2.4. Meanwhile, system's inverter model and battery model are illustrated in Sections 3.3 and 3.4, respectively. The calculation of energy produced by the PV array (E_{PV}) depends on the time step of the weather data used. In other words, if hourly input solar radiation data are given, then the power produced by the PV array,$P_{PV}(t)$, is equal to PV energy production, $E_{PV}(t)$. In contrast, if the input data are daily solar energy, the

$$E_{pv}(t) = P_{pv}(t)S \qquad (3.25)$$

Where S is the day length that can be given by

$$s = \frac{2}{15}\cos^{-1}(-\tan L \tan \delta) \qquad (3.26)$$

where L is the latitude and δ is the angle of declination. Figure 4.2 shows the flowchart for modeling an SAPV. The energy at the front end of an SAPV system or at the load side is given by

$$E_{net}(t) = \sum_{i=1}^{366}\left(E_{pv}(t) - E_L(t)\right) \qquad (3.27)$$

where E_L is the load energy demand. The result of Equation 4.3 is either positive $\left(E_{pv} > E_L\right)$ or negative $\left(E_{pv} > E_L\right)$. If the energy difference is positive, then there is an excess in energy (EE), and if negative, then there will be an energy deficit (ED). The excess energy is stored in batteries in order to be used in times of ED. ED can be

defined as the disability of the PV array to provide full power to the load at a specific time.

Using MATLAB® modelling for a 2.5 kW, 117Ah/12 SAPV system utilizing the data in Source 7. The first step in writing a MATLAB code for an SAPV is to define the source file and the variables such as hourly solar radiation (G), hourly ambient temperature (T), and the hourly load demand (L). In addition to that, some specification of the system needs to be defined such as the capacity of the PV array, the capacity of the storage battery, inverter rated power, the efficiency the PV module, the allowable depth of charge, the charging efficiency, and the discharging efficiency (Routine 2).

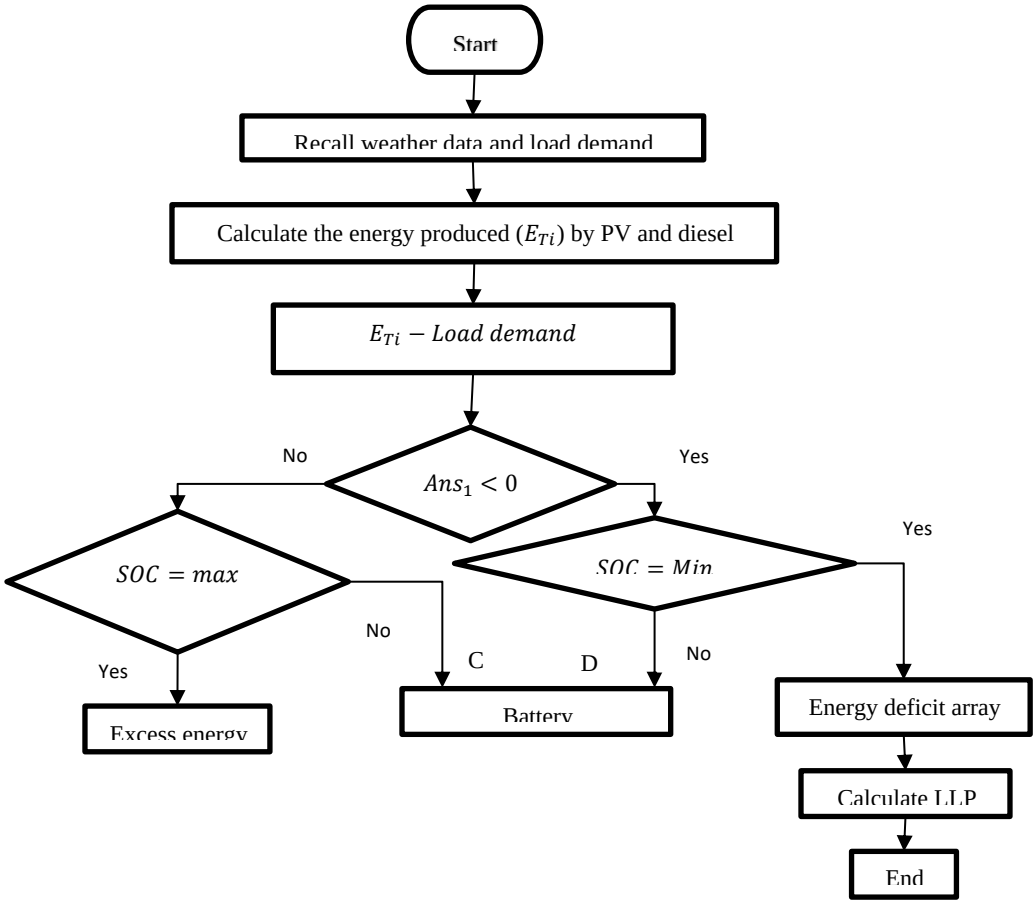

Figure 4.2 Flowchart for modeling a stand-alone PV system.

The simulation process starts by calculating the produced energy by the PV array, and then the net energy (E_{net}) is calculated. The maximum state of charge (SOC) of the battery is given to the variable SOC_i as an initial value. In addition to that, matrices are defined so as to contain the results of battery state of charge (SOC_f), damped energy (Dampf), and energy deficits (Doff) being initiated and defined. At this point a "for loop" is initiated to search the values of the E_{net} array. Then the energy difference is added to the variable SOC_i. Here, if the result SOC is higher than SOC_{max}, the damped energy is calculated and stored in the "Dampf" array. Meanwhile the ED is set zero and the battery SOC does not change. This condition represents the case of the energy produced by the PV array and is higher than the energy demand. The battery is fully charged from the previous step.

The second condition represents the case that the energy produced by the PV array and the battery together is lower than the energy required. Here the battery must stop supplying energy at the defined depth of discharge (DOD) level, while the ED equals

the uncovered load demand. In addition to that, the damped energy here is equal to zero.

The last condition represents the case that the energy produced by the PV array is lower than the load demand but the battery can cover the remaining load demand. In this case there is no damped nor deficit energy, while the battery SOC equals the difference between the maximum SOC and supplied energy. Finally, battery SOC values and deficit and damped energy values are recalled and the loss of load probability is calculated:

```
%%(1)Data sources

fileName = 'PV Modeling Book Data Source.xls';

sheetName = 'Source 7';

G= xlsread(fileName, sheetName , 'A1:A8761');

T= xlsread(fileName, sheetName , 'B1:B8761');

L= xlsread(fileName, sheetName , 'D1:D8761');

%%(2)System specifications

PV_Wp=2500; % the capacity of the PV array (Watt)

Battery_SOCmax= 1400; % battery capacity Wh/day

PV_eff=0.16; % efficiency of the PV module

V_B=12; % voltage of the used battery

Inv_RP=2500 %inverter rated power

DOD=0.8; %allowed depth of charge

Charge_eff=0.8; % charging eff

Alpha= .05; % alpha

Wire_eff= 0.98;
```

```
SOCmin=SOCmax*(1-DOD)

 %%(3.1) Simulation of the SAPV system

P_Ratio=(PV_Wp *(G/1000))/Inv_RP;

Inv_eff=97.644-(P_Ratio.*1.995)- (0.445./P_Ratio); %5KW

E_PV= ((PV_Wp*(G/1000))- (Alpha*(T-25)))*… Wire_eff*

 Inv_eff;

E_net=EP_V-L;

SOCi=SOCmax

SOCf=[];

Deff=[];

Dampf=[];

%%(3.2)

for i=1:length(E_net);

SOC= ED+SOCi;

if (SOC > SOCmax)

 Dampi=SOC-SOCmax;

 Defi=0;

 SOCi=SOCmax;

%%(3.3)

elseif (SOC<SOCmin)

 SOCi=SOCmin;

 Defi=SOC-SOCmin;

 Dampi=0;
```

```
%%(3.4)

else

SOCi=SOC;

Defi=0;

Dampi=0;

end

%%(3.5)

SOCf=[SOCf; SOCi];

Deff=[Deff; Defi];

Dampf=[Dampf; Dampi];

end

SOCf;

Deff;

Dampf;

SOC_per=SOCf./SOCmax;

LLP_calculated=abs(sum(Deff))/(sum (L))
```

4.4 ENERGY FLOW MODELING FOR HYBRID PV/DIESEL POWER SYSTEMS

Figure 4.5 shows a hybrid PV/diesel system. The system is supposed to have the PV array as a main source with a backup battery, while the diesel generator (DG) is operated in deficit time. Here the deficit time is defined as the time in which the

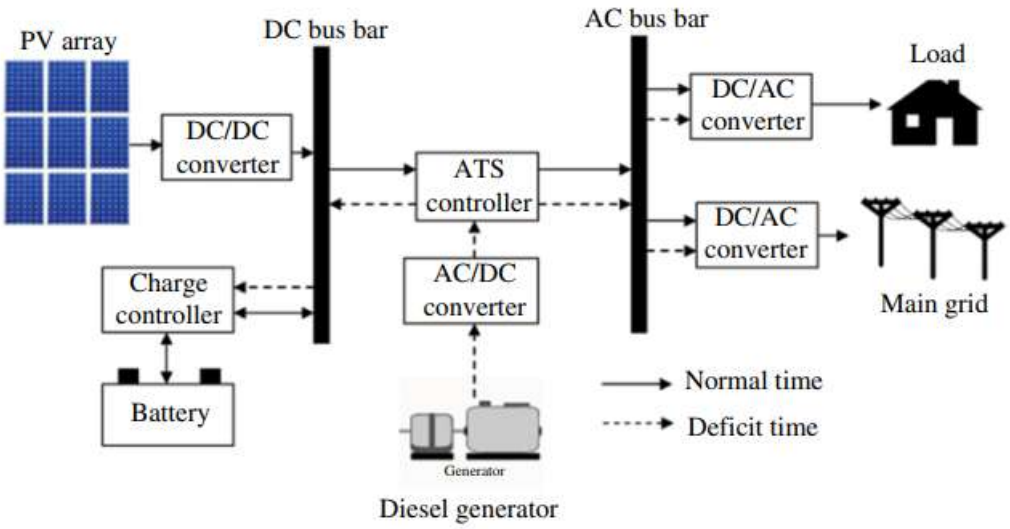

Figure 4.5 Hybrid PV/diesel system configuration.

instantaneously produced energy form the PV array and battery is not enough to cover the load demand. The implementation of an energy flow model for hybrid PV/diesel system is different from the hybrid PV/wind and SAPV systems. Figure 4.6 shows the flowchart of simulating the PV/diesel system.

Develop a MATLAB code for a PV/diesel system utilizing the data in (source) 2500Wp PV array, 3kVA diesel generator, and a 580Ah/12V battery at 1% loss of load probability

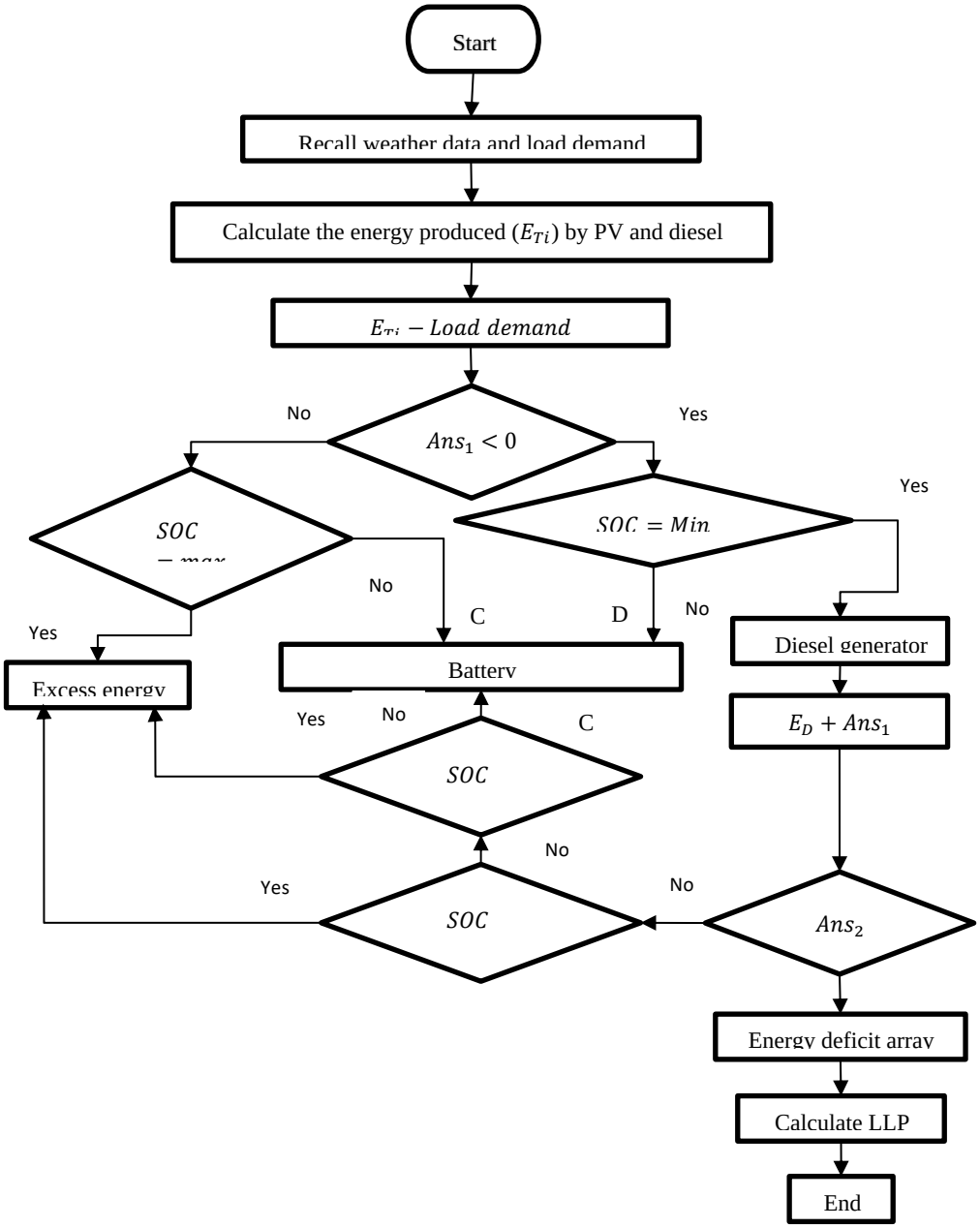

Figure 4.6 Flowchart for PV/diesel system simulation.

The system first supplies the load as there is no diesel generator in the system. Meanwhile the diesel generator will be operated in the time that the energy produced by the PV array and the battery is not enough to cover the load demand. The first and second parts of the energy flow model code are like the one for the SAPV system, but the capacity of the used diesel generator (kWh/day) must be added to the first part. After that, a "for loop" is initiated to search the array of the "energy net" (E_{net}) values. The following part represents the case that the energy generated by the PV array is more than the load demand and consequently there is no generated energy

neither by the diesel generator nor the battery. In addition, there is no energy deficit in this case, while the energy to be damped equals to the difference between the energy generated by PV and the load demand. The second case is when the energy generated by the PV array and the battery is less than the energy demand. In this case, the diesel generator must cover the load demand that is not covered by the PV array and the battery. In addition to that, the diesel generator is used to charge the battery. At this point, there are three scenarios:

1. The first is that the diesel generator produced the maximum possible energy to supply the load and to charge the battery, while the battery state of charge (SOC) is less than or equal maximum SOC.

2. The second is that the battery SOC reaches the maximum value and the diesel generator at this point must stop chagrining the battery.

3. In the third, the diesel generator could not cover all the demanded energy by the load, and it is consequently not able to charge the battery.

Finally, the following code represents the case that the battery is able to cover the load demand alone. Here the diesel generator is used to charge the battery as well. The diesel generator is supposed to keep the battery fully charged to be ready for deficit times. This is because the fact that the use of the energy stored in a battery is easier than operating a diesel generator since the diesel generator needs a start-up time. Moreover, the frequent on/off states of a diesel generator affects its lifetime negatively. However, in this part also the SOC of the battery must be controlled in order not to exceed the allowable SOC.

Eventually, four calculated values are stored in arrays. These values are the energy deficits, damped energy, battery SOC, and energy produced by diesel generator. Here also the loss of load probability can be calculated to evaluate the reliability of the designed system:

```
for i=1:length(E_net);

SOC= Net_E(i)+SOCi;
```

```
if (SOC > SOCmax)
 Dumpi=SOC-SOCmax;
 Defi=0;
 SOCi=SOCmax;
 E_Gen=0;
%%(2.1)
elseif (SOC<SOCmin)
 Old_Defi=(SOC-SOCmin)+E_Capacity;
 if (Old_Defi >=0)
 SOCi=SOCmin+Old_Defi;
%%(2.2)
if (SOCi<=SOCmax)
Defi=0;
 Dumpi=0;
 E_Gen= abs(Old_Defi)+ (SOCi-SOCmin);
 SOCi=SOCmin+Old_Defi;
%%(2.3)
else
 Defi=0;
 Dumpi=0;
```

```
 E_Gen= abs(Old_Defi)+ (SOCi-SOCmin)- (SOCi-SOCmax);
 SOCi=SOCmax;
 End
%%(2.4)
else
 SOCi=SOCmin;
 Defi=Old_Defi;
 Dumpi=0;
 E_Gen= E_Capacity;
 end
%%(3)
else
SOCi=SOC+ E_Capacity;
if (SOCi <= SOCmax)
Defi=0;
Dumpi=0;
E_Gen=E_Capacity;
SOCi=SOC+ E_Capacity;
else
Defi=0;
```

```
Dumpi=0;

E_Gen=E_Capacity- (SOCi-SOCmax);

SOCi=SOCmax;

end

end

SOCf=[SOCf; SOCi];

Deff=[Deff; Defi];

Dumpf=[Dumpf; Dumpi];

E_Geni=[E_Geni; E_Gen];

end

SOCf;

Deff;

Dumpf;

E_Geni;

SOC_per=SOCf./SOCmax;

LLP_calculated=abs(sum(Deff))/(Sum(L))
```

CHAPTER FOUR

RESULTS AND DISCUSSION

2.5.Introduction

This project focuses on electric spring and PV energy flow activities due to its wide implementation. Thus, an analysis and investigation are required to show the effect of PV and ES on HLI assessment comparing to original case. The following sections address the impact of PV and ES modelling techniques on HL1 assessment.

2.5.1 PV and ES Impacts on HL1 Adequacy Assessment

PV and ES are modelled to show the impact of each activity separately on generating systems adequacy indices. Multi scenarios are considered for each activity to show the changes in reliability indices compared with the varying of each activity scenario. The reliability indices that are used in this section is EENS only.

2.6 HL1 adequacy Assessment considering Case studies

This section is divided into three case studies. Case study 1 involves Hl1 assessment of the IEEE-RTS without any action. Case 2 involves the impact of PV model on the HL1 assessment. Case 3 includes the ES impact on the reliability of the generation systems

2.6.1 HL1 Assessment with PV

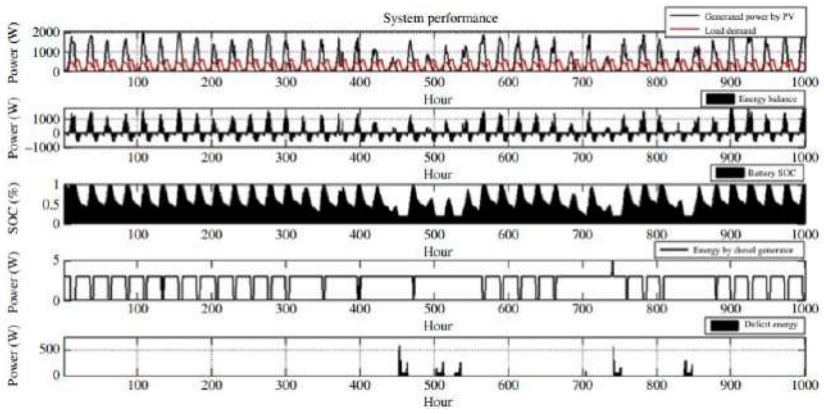

Figure 4.7 Performance of the designed hybrid PV/diesel system. (See insert for colour representation of the figure.)

TABLE 4.1 Comparison between Load-Following and Cycle-Charging Control Strategies of Hybrid PV/DG/Battery Systems

	Load Following	Cycle Charging
Clear sky		
Energy generated by PV (kWh/day)	13.32	13.32
Energy generated by battery (kWh/day)	0.72	2.2
Energy generated by DG (kWh/day)	6.26	6.26
DG operation time (h/day)	11.94	5.61
Deficient energy (kWh/day)	0	0
Excess energy (kWh/day)	8	8.1
Fuel consumption (l/day)	32.2	11.88
Fuzzy day		
Energy generated by PV (kWh/day)	3.89	3.89
Energy generated by battery (kWh/day)	1.05	3.36
Energy generated by DG (kWh/day)	7.66	7.59
DG operation time (h/day)	14.16	6.9
Deficient energy (kWh/day)	0	0
Excess energy (kWh/day)	0.1	0.11
Fuel consumption (l/day)	46.73	18

Table shows the result of EENS for Case studies.

Table 4.1 EENS for Case study

Case studies	Case study details	EENS(MWh/yr)
Case study 1	Base value	1197.4448
Case study 2	PV (24 MW)	1208.0000
Case study 3	PV (24MW+ 40 MW)	2134.9000

Case study 4	PV ((24+ 40+150) MW)	11090.0000
Case study 5	PV ((24+ 40+150+200) MW)	33621.000

The EENS base value without PV action has been previously assessed [4] . The effect PV on EENS is discussed as follows. When PV is not used, the EENS is 1197.4448 MWh/yr . After replacing G12 MW unit by PV 24 MW EENS value is higher than base case. As much as PV replaced the EENS becomes worse. This highlights the reliability benefits of the PV measures. When PV is considered, there is not an improvement in EENS. This proves that PV has a significant impact on the reliability of generation systems. The results provide confirmatory evidence that EENS of base case are quite different from others study cases . As well, it is noted that the dynamic considerations of available system capacity have an important impact on the generating systems adequacy assessment thus must be accurately modelled. During the planning phase, the reliability of electrical power systems can be enhanced by increasing the adequacy of supply and this increases the initial costs. The corresponding cost might not be worth the enhancement of reliability. The balance in the investment cost of PV and energy storage systems programmes can be achieved to find an optimal planning decision of reliability level. The results have shown that PV is clearly an affective if integrated with energy storage systems in terms of improving the reliability of power supply. In PV model, optimal regulatory incentives can be determined by considering the efficiency, state of charge and availability of solar radiation. However, when the load level is higher than the available generation capacity, this amount of load should be under the direct control of the utilities. Hence, electricity suppliers are allowed during adequacy deficiency to shed the load and then cycle partially or totally the curtailed energy per each interruption. In-need period significantly affects the EENS since peaking and cycling load units have less operating hours and more shutdowns and startups actions than base load units do. This is due to less the needed period is, the less failure probability of units. As well, startups of peaking units are only required when they are in need. Since peaking units, during the duty cycle, have less actual failure probability than base load units, they operate more reliably than base load units do. According to the priority order, the peaking and

cycling load units have lower loading while base load units have higher loading. That is why , the (PV+ES) model can be used as peaking units.

2.7 HL1 Adequacy Assessment with PV as Alternatives to Peaking Units using Hybrid Model

The impact of (PV) as alternatives to peaking units in terms of adequacy using is investigated in this section. Throughout the year, the total energy capacity for each generation unit in IEEE-RTS cannot be totally supplied. This is because of outages, planned maintenance and reserve margin operation requirement. The remaining energy, therefore, is the EES. In a yearly base, Figure shows the EES for each generation units as well as the ENS due to planned and unplanned outage and remain energy represents the available energy for reserve margin requirement. The utility has to generate energy more than demand requires in the aim of keeping system secure during the outages and sudden increase in demand. The available capacity above the load curve is called reserve capacity.

2.8 Conclusion

This project presents a modelling of solar radiation in reliability framework that successfully retains the statistical properties of the original data. This method generates data at each hour based on the probability of occurrence of solar radiation at n previous hours. Therefore, the proposed method can generate synthetic solar radiation that is suitable for chronological simulation, such as the sequential Monte Carlo simulation. Standard deviation and mean are other statistical characteristics that are highly retained by the proposed method. HL1 adequacy assessment is an essential area of power system reliability. It is used extensively in power system planning and operation phases. PV is the main contributor to energy management .It influences the energy consumed and significantly improves cost and reliability if integrated with energy storage systems. During generating system adequacy deficiency, most of the energy curtailed can be recovered in the same day; however, a certain amount of energy cannot be recovered due to the stochastic nature of failures that might be extended to the

recovery period time. Although recovery time is usually on off-peak period, the capacity of energy must be recovered during the hours of the day might exceed the available generation capacity. This amount of energy is called EENR. The major limitations of PV implementation are the highly initial cost and uncertainty. Power systems usually have reserve capacity margin to account for load uncertainty and generator outages as well as planned maintenance. The PV+ES programme proposed in this project improves the adequacy of the power supply without introducing additional classical power generating facility thus PV is a viable alternative that is much faster to be implemented. Thus, the PV is clearly more effective than classical generating units in terms of improving the reliability of power supply. The superiority of the proposed method in all tests irrefutably show its efficiency in modelling solar radiation. Future works can verify the ability of this method to simulate other metrological parameters required in reliability studies, such as wind and temperature.

REFERENCES

1. Dehnavi, E. and H. Abdi, *Determining optimal buses for implementing demand response as an effective congestion management method.* IEEE Transactions on Power Systems, 2017. **32**(2): p. 1537-1544.

2. Freeman, R., *Managing energy: Reducing peak load and managing risk with demand response and demand side management.* Refocus, 2005. **6**(5): p. 53-55.

3. Billinton, R.A., R.N. , *Reliability evaluation of power systems*2013: Plenum: New York, NY, USA, 1984.

4. Li, W., *Reliability assessment of electric power systems using Monte Carlo methods*2013: Springer Science & Business Media.

5. Ahsan, Q., *Load management: impacts on the reliability and production costs of interconnected systems.* International Journal of Electrical Power & Energy Systems, 1990. **12**(4): p. 257-262.

6. Teh, J., *Adequacy Assessment of Wind Integrated Generating Systems Incorporating Demand Response and Battery Energy Storage System.* Energies, 2018. **11**(10): p. 2649.

7. Joung, M. and J. Kim, *Assessing demand response and smart metering impacts on long-term electricity market prices and system reliability.* Applied Energy, 2013. **101**: p. 441-448.

8. Zhou, Y., P. Mancarella, and J. Mutale, *Modelling and assessment of the contribution of demand response and electrical energy storage to adequacy of supply.* Sustainable Energy, Grids and Networks, 2015. **3**: p. 12-23.

9. Rahmani andebili, M., *Risk and cost based generation scheduling smartly mixed with reliability driven and market driven demand response measures.* International Transactions on Electrical Energy Systems, 2015. **25**(6): p. 994-1007.

10. Yousefi Ramandi, M., et al., *Reliability and economic evaluation of demand side management programming in wind integrated power systems.* International Journal of Electrical Power & Energy Systems, 2016. **78**: p. 258-268.

11. Moshari, A., A. Ebrahimi, and M. Fotuhi-Firuzabad, *Short-term impacts of DR programs on reliability of wind integrated power systems considering demand-side uncertainties.* IEEE Transactions on Power Systems, 2016. **31**(3): p. 2481-2490.

12. Kopsidas, K. and A. Kapetanaki, *Optimal Demand Response Scheduling with Real Time Thermal Ratings of Overhead Lines for Improved Network Reliability.* IEEE Transactions on Smart Grid, 2016.

13. Allan, R.N., R. Billinton, and N. Abdel-Gawad, *The IEEE reliability test system-extensions to and evaluation of the generating system.* IEEE Transactions on Power Systems. (86WM 0384); T-PWRSNov86 1-7, 1986.

14. Subcommittee, P.M., *IEEE Reliability Test System* IEEE Transactions on Power Apparatus and Systems, 1979. **pp. 2047-2054,**.

15. Huang, D. and R. Billinton. *Impacts of demand side management on bulk system reliability evaluation considering load forecast uncertainty*. in *2011 IEEE Electrical Power and Energy Conference*. 2011.

16. Billinton, R. and D. Lakhanpal, *Impacts of demand-side management on reliability cost/reliability worth analysis.* IEE Proceedings - Generation, Transmission and Distribution, 1996. **143**(3): p. 225-231.

Ministry of Higher Education and Scientific Research

Al-Iraqia University

Collage of Engineering

Electrical Engineering Department

IMPLEMENTATION OF AN ADAPTIVE MEAN FILTER FOR SALT AND PEPPER NOISE REMOVAL

A Project Submitted to the Department of Electrical Engineering in Partial Fulfillment for the Requirements of the Degree of B.Sc. in Electrical Engineering

BY :

Ali Saeed Hadi

Ali Sameer Fidel

Ali Abdul Ameer Hayder

SUPERVISOR NAME

ASSIST.PROF: ANAS F.AHMED

2022-2023

DECLARATION

We hereby declare that this project report is based on our original work except for citations and quotations, which have been duly acknowledged.

Signature:

Name: علي سعيد هادي

Date:

Signature:

Name: علي عبد الامير

Date:

Signature

Name: علي سمير فاضل

Date:

APPROVAL FOR SUBMISSION

I certify that this project report entitled "**IMPLEMENTATION OF AN ADAPTIVE MEAN FILTER FOR SALT-AND-PEPPER NOISE REMOVAL** " was prepared by **Ali Saeed Hadi,Ali Sameer Fadel,Ali Abdulameer Hayder** has met the required standard for submission in partial fulfilment of the requirements for the award of Bachelor of Electrical Engineering at Al-Iraqia University .

Approved by :

Signature :

Supervisor : **ASSIST.PROF: ANAS F.AHMED**

Date :

ACKNOWLEDGEMENTS

First and forement, prises and thanks to ALLAH who helped us to complete this research

We would like to thank the project supervisor (**ASSIST.PROF: ANAS F.AHMED**), who each provided advice and Guidance throughout the search process and assist us in completing this work.

we would also like to express our thanks to the administration of the Electrical Engineering Department / AL-Iraqia University. In Finally.

we thank our families and any person who help us for their supports during the period of this work.

ABSTRACT

In this project, we proposed a salt-and-pepper noise (SPN) removal method, Adaptive Mean Filter (AmF), and provide some of its basic notions. We then apply AmF to several test images whose noise densities range from 10% to 90%: 6 traditional test images (lena image, brain image, xray of Back bone image processing) and other test images, provided in the TESTIMAGES Database. Afterwards, we compare AmF with the state-of-art methods, We compared the AMF filter with the rest of the filters in terms of PSNR and ssim with different noise densities. The results by The Peak Signal to Noise Ratio (PSNR) and Structural Similarity (SSIM) show that AmF performs better than the methods mentioned above. Moreover, we also compare the running time data of these algorithms. These results show that AmF outperforms the methods except for DAMF. We finally discuss the need for further research.

Table of Contents

Chapter One

Introduction

Chapter Two

Literature Review

Chapter Three

Methodology

Chapter Four

Discussions and Results

Chapter Five

Conclusion and Recommendations

for Future Work

CHAPTER ONE
Introduction

CHAPTER ONE
Introduction

1.1 Background :

With the rise of technology and the wide use of the internet, one way to communicate is through sending digital images. Unfortunately, during the transmission, digital images could be corrupted by various types of noise. One of the common noise types that is normally corrupting digital images is impulse noise. Impulse noise appears as sprinkles, which normally presented by two intensity levels, in images. Therefore, impulse noise can be presented by two noise components. The first noise component is the salt noise, which is presented by high intensity level. It appears as bright colored dots on the image. The second component is the pepper noise, which has lower intensity level. It appears as dark colored dots on the image , The second component is the pepper noise, which has lower intensity level. It appears as dark colored dots on the image **[1].**

Several causes may contribute to the appearance of impulse noise on digital images. Impulse noise may occur during image transmission through noisy channels, especially in air transmission channels. In these transmission channels, some of the data may be replaced by noise. These channels are used in some common applications such as broadcasting, videophone, traffic observation, and autonomous navigation **[2].**

In addition to this, impulse noise may be corrupted by bit errors in transmission, malfunctioning pixels, faulty memory locations and buffer overflow **[3].**

Moreover, lighting, induction from industrial machines, weak insulation of high-voltage power lines, and various unprotected electric switches are other causes for impulse noise **[4]**.

1.2 Problem Statements

Each captured image contains noise. noise can be produced by the image sensor and circuitry of a scanner or digital camera. Image noise can also originate in film grain and in the unavoidable shot noise of an ideal photon detector. Image noise is an undesirable by-product of image capture that obscures the desired information. The original meaning of "noise" was "unwanted signal"; Image noise can range from almost imperceptible specks on a digital photograph taken in good light, to optical and radio astronomical images that are almost entirely noise, from which a small amount of information can be derived by sophisticated processing. Such a noise level would be unacceptable in a photograph since it would be impossible even to determine the subject. There are different types of noises available At the same time, noise making the image blurred. The bad condition was submerged fully. It gives analysis big difficulty. Therefore, people need to suppress unwanted noise to improve image quality. For digital image noise reduction, the basic filtering algorithms are used Adaptive Mean Filter (AmF) **[5]**.

1.3 Aims and Objectives

We aim to use Matlab to process the image and compare the image clarity under filtering. The project aims to obtain the nearest image quality to the real one by removing the noise in the images. And The idea of mean filtering is simply to replace each pixel value in an image with the mean (`average') value of its neighbors, including itself. This has the effect of eliminating pixel values which are unrepresentative of their surroundings. Mean filtering is usually thought of as a convolution filter. Like other convolutions it is based around a kernel, which represents the shape and size of the neighborhood to be sampled when calculating the mean. Often a 3×3 square kernel is used, although larger kernels (e.g. 5×5 squares) can be used for more severe smoothing. In this project , we analyse two well-known objective image quality metrics, the peak-signal-to-noise ratio (PSNR) as well as the structural similarity index measure (SSIM), and we derive a simple mathematical relationship between them which works for various kinds of image degradations **.**

1.4 Sources of Noise In Images :

Noise is introduced in the image at the time of image acquisition or transmission:

1. The imaging sensor may be affected by environmental conditions during image
2. Tcquisition. Insufficient Light levels and sensor temperature may introduce the noise in the image.
3. Interference in the transmission channel may also corrupt the image.
4. If dust particles are present on the scanner screen, they can also introduce noise in the image **[6]**.

1.5 Classification of Noise :

1. Independent noise: Noise which is dependent on the image data. Image independent noise :can often be described by an additive noise model, where the recorded image.
2. Data-dependent noise: This noise arising when monochromatic radiation is scattered from a surface whose roughness is of the order of a wavelength, causing wave interference which results in image speckle**[7]**.

1.6 Noise Models :

- Salt & pepper Noise (Impulse Noise)
- Gaussian Noise (Amplifier Noise)
- Poisson Noise (Shot Noise)
- Spackle Noise

1.6.1 Salt & pepper Noise (Impulse Noise) :

the noise is caused by errors in the data transmission. The corrupted pixels are either set to the maximum value (which looks like snow in the image) or have single bits flipped over. In some cases, single pixels are set alternatively to zero or to the maximum value, giving the image a `salt and pepper' like appearance. Unaffected pixels always remain unchanged. The noise is usually quantified by the percentage of pixels which are corrupted. The typical intensity value for pepper noise is close to 0 and salt noise close to 255**[8]**.

1.6.2 Gaussian Noise (Amplifier Noise) :

Gaussian noise represents Statistical Noise having Probability Density Function(PDF) equal to that of the Normal distribution, which is also known as the Gaussian Distribution. It is a major part of the read noise of an image sensor that is of the constant level of noise in the dark areas **[8]**.

1.6.3 Poisson Noise (Shot Noise) :

The dominant noise in the lighter parts of an image from an image sensor is typically that caused by statistical quantum fluctuations that is variation in the number of photons sensed at a given exposure level **[8]**.

1.6.4 Spackle Noise :

Speckle noise is a phenomenon that accompanies all coherent imaging modalities in which images are produced by interfering echoes of a transmitted waveform that emanate from heterogeneities of the studied object **[8]**.

1.7 Denoising Techniques

There are basic two approaches of the image denoising: spatial domain filtering and transform domain filtering.

1.7.1 Linear filters:

A linear filter is the filter whose output is a linear function of the input. Any output value of a linear filter is the weighted mean of input values. In other words, to form one element of the output at time , it is necessary to multiply the input values for time moments adjacent to **[6]**.

1.7.1.1 Mean filter:

Mean filtering is a simple, intuitive and easy to implement method of smoothing images, i.e. reducing the amount of intensity variation between one pixel and the next. It is often used to reduce noise in images. The idea of mean filtering is simply to replace each pixel value in an image with the mean (`average') value of its neighbors, including itself. This has the effect of eliminating pixel values which are unrepresentative of their surroundings. The two main problems with mean filtering, which are:

A single pixel with a very unrepresentative value can significantly affect the mean value of all the pixels in its neighborhood.

When the filter neighborhood straddles an edge, the filter will interpolate new values for pixels on the edge and so will blur that edge. This may be a problem if sharp edges are required in the output **[6]**.

1.7.1.2 Wiener filter:

The wiener filtering method requires the information about the spectra of the noise and the original signal and it works well only if the underlying signal is smooth. Wiener method implements spatial smoothing and its model complexity control correspond to choosing the window size wiener filtering is able to achieve significant noise removal when the variance of noise is low, they cause blurring and smoothening of the sharp edges of the image **[6]**.

1.7.2 Non-linear filter:

n signal processing, a nonlinear (or non-linear) filter is a filter whose output is not a linear function of its input. That is, if the filter outputs signals R and S for two input signals r and s separately, but does not always output αR + βS when the input is a linear combination αr + βs.. **[6]**.

1.7.2 .1 Median filter:

Median filtering is a common step in image processing. Median filter is a well-used nonlinear filter that replaces the original gray level of a pixel by the median of the gray values of pixels in a specific neighborhood. The median filter is also called the order specific filter because it is based on statistics derived from ordering the elements of a set rather than taking the means. This filter is popular for reducing noise without blurring edges of the image It is particularly useful to reduce salt and pepper noise and speckle noise as well . Its edge preserving nature makes it useful in cases where edge blurring is undesirable **[6]**.

Chapter Two

Literature Review

Chapter Two

Literature Review

2.1Literature Review :

First, we need to understand what salt and pepper noise is. Salt and pepper noise is a type of image noise that appears as white and black pixels scattered randomly in an image. Digital filters can remove salt and pepper noise. **[10]**.

Imran & Zafar, 2016 Several studies have been conducted on the use of digital filters to remove salt and pepper noise from images. In the paper by A. Imran and N. Zafar titled "Removal of Salt and Pepper Noise from Images Using Digital Filters," they proposed a new hybrid filter which combines the median filter and the mean filter to remove salt and pepper noise from images. They evaluated their proposed filter on various images and compared it with other state-of-the-art methods, and their results show that the proposed filter outperforms other methods in terms of both peak signal-to-noise ratio (PSNR) and visual quality **[11]**.

Thakur & Kumar, 2018 Another study by V. K. Thakur and V. Kumar titled "A Comparative Study of Salt and Pepper Noise Removal Techniques for Digital Images," evaluated the performance of several filters, including the median filter, the adaptive median filter, and the arithmetic mean filter, for removing salt and pepper noise. Their results showed that the adaptive median filter outperforms other filters in terms of mean square error (MSE) and PSNR and is less sensitive to noise density **[12]**.

Islam & Rahman, 2019 In another paper by S. M. S. Islam and M. S. Rahman titled "Removal of Salt and Pepper Noise from Images Using Fuzzy Logic with Digital Filters," they proposed a new method that combines fuzzy logic with digital filters to remove salt and pepper noise from images. Their method is based on the fuzzy-based membership function and performs well in removing salt and pepper noise while preserving the edges of the image **[13]**.

Abdul Zehra & Al-Mahasneh, 2017 proposed a new approach for removing salt and pepper noise from images based on the adaptive impulse detection filter (AIDF) and the wavelet thresholding technique. The proposed method was evaluated using various metrics, and the results show that the proposed method outperforms other state-of-the art methods in terms of both visual quality and quantitative assessment **[14]**.

J. Liu, Q. Chen, and Q. Liu.2018 proposed a new method for removing salt and pepper noise from images using the self-adaptive non-local mean (SANLM) filter. The proposed method can adaptively estimate the parameters of the SANLM filter according to the noise and edge information of the image. Experimental results show that the proposed method outperforms other methods in terms of both quantitative and visual quality **[15]**.

S. M. Faisal and M. A. Basheer proposed a new method for removing salt and pepper noise from images based on the fuzzy switching median filter and the improved geographic weighted regression (GWR) model. The proposed method can effectively remove salt and pepper noise while preserving the image details. **[16`]**.

Faisal & Basheer, 2019 these are just a few examples of recent studies related to removing salt and pepper noise using digital filters. As you can see, researchers are still actively exploring new methods and improving existing ones to effectively remove salt and pepper noise from images **[17]**.

Chapter Three

Methodology

Chapter Three

Methodology

3.1 Preliminaries and AmF

In this section, we first provide some basic notions. Throughout this paper, let $A \coloneqq [aij]\ m{\times}n$ be an image matrix (IM) such that aij is an unsigned integer number and $0 \leq aij \leq 255$.

Definition 3.1.1 Let $A \coloneqq [aij]\ m{\times}n$ be an IM, aij is called a noisy entry of A if $aij = 0$ or $aij = 255$; otherwise, aij is called a regular entry of A.

Definition 3.1.2 Let A be an IM. Then, A is called a noise image matrix (NIM), if for some i and j, aij is a noisy entry of A.

Definition 3.1.3 Let A be an NIM. Then, $B \coloneqq [bij]\ m{\times}n$ is called binary matrix of A where

$bij = \begin{cases} 0, & aij \text{ is a noisy entry of } A \\ 1, & \text{otherwise} \end{cases}$

$$\begin{bmatrix} a_{tt} & \cdots & a_{t1} & a_{t2} & a_{t2} & \cdots & a_{tn} & a_{tn} & \cdots & a_{t(n-t+1)} \\ \vdots & \ddots & \vdots & \vdots & \vdots & \ddots & \vdots & \vdots & \ddots & \vdots \\ a_{1t} & \cdots & a_{1t} & a_{1t} & a_{12} & a_{1n} & a_{1n} & a_{1n} & \cdots & a_{1(n-t+1)} \\ a_{1t} & \cdots & a_{11} & a_{11} & a_{12} & a_{1n} & a_{1n} & a_{1n} & \cdots & a_{1(n-t+1)} \\ a_{2t} & \cdots & a_{21} & a_{21} & a_{22} & a_{2n} & a_{2n} & a_{2n} & \cdots & a_{2(n-t+1)} \\ a_{3t} & \cdots & a_{31} & a_{31} & a_{32} & a_{3n} & a_{2n} & a_{2n} & \cdots & a_{3(n-t+1)} \\ \vdots & \ddots & \vdots & \vdots & \vdots & \ddots & \vdots & \vdots & \ddots & \vdots \\ a_{mt} & \cdots & a_{m1} & a_{m1} & a_{m2} & a_{mn} & a_{mn} & a_{mn} & \cdots & a_{m(n-t+1)} \\ a_{mt} & \cdots & a_{m1} & a_{m1} & a_{m2} & a_{mn} & a_{mn} & a_{mn} & \cdots & a_{m(n-t+1)} \\ \vdots & \ddots & \vdots & \vdots & \vdots & \vdots & \vdots & \vdots & \vdots & \vdots \\ a_{(m-t+1)t} & \cdots & a_{(m-t+1)1} & a_{(m-t+1)1} & a_{(m-t+1)2} & \cdots & a_{(m-t+1)n} & a_{(m-t+1)n} & \cdots & a_{(m-t+1)(n-t+1)} \end{bmatrix}$$

Definition 3.1.5 Let $A \coloneqq [aij]\ m{\times}n$ and $k \in \{1,2, \dots, t\}$. Then, k-approximate matrix of aij in $\bar{\bar{A}}t$ is denoted by $A_{ij}{}^{k}$ and is as follows:

$$\begin{bmatrix} \bar{\bar{a}}_{(i+t-k)(j+t-k)} & \cdots & \bar{\bar{a}}_{(i+t-k)(j+t+k)} \\ \vdots & \ddots & \vdots \\ \bar{\bar{a}}_{(i+t+k)(j+t-k)} & \cdots & \bar{\bar{a}}_{(i+t+k)(j+t+k)} \end{bmatrix}$$

Definition 3.1.6 The matrix $\hat{A}ij\ k \coloneqq [\hat{a}1\ ]$ consisting of all regular entries of $A_{ij}{}^{k}$ and non-decreasing is called regular row matrix or regular entry matrix (REM) of $A_{ij}{}^{k}$.

Definition 3.1.7 Let $\hat{A}ij\ k \coloneqq [\hat{a}1v\ ]1{\times}w$ be the REM of $A_{ij}{}^{k}$. Then, Cesáro mean of $A_{ij}{}^{k}$ is defined as follows $C(\hat{A}_{ij}{}^{k}) \coloneqq \frac{1}{\omega}\sum_{v=1}^{w} \hat{a}1v$

Definition 3.1.8 A matrix with all its entries being zero is called zero matrix and is denoted [0]. Secondly, we give the algorithm of ACmF and its flowchart in Figure 1 as follows:

ACmF's Algorithm Steps

Step 1. Read a NIM $A \coloneqq [aij]{\times}n$ such that $\min\{m, n\} \geq 5$

Step 2. Convert A from uint8 form to double form

Step 3. For t from 5 to 1

Obtain the binary matrix $B \coloneqq [bij]{\times}n$ of A

Obtain $\bar{\bar{A}}t$ and $\bar{\bar{B}}_{t}$

For all i and j

If $bij = 0$

For k from 1 to t

If $Bij\ k \neq [0]$

Obtain A_{ij}^{k}

Obtain $\hat{A}_{ij}^{k}$

$aij \leftarrow Cm(\hat{A}_{ij}{}^{k})$

Break

End If

End For

End If

End For

End For

3.2 The Used Image Processing Functions for Matlab and The Flowchart of AMF

The Used Image Processing Functions for Matlab and the Flowchart of AMF

1-Read and display file Function [X، map] play a role in the file، it can be called in the following format: [X، map] =imread (filename، fmt) ， the filename for read the image file name. fmt as the image format. I show function is to display the file, its syntax is as follows: show (BW) show(X, map) **[6]**.

2- Calculate two-dimensional convolution Function conv2 format: C = conv2 (A, B) is considered the role of the convolution matrix A and B.

3- Matlab implementation of the noise Function imnoise format: J=imnoise(I, type) J = imnoise (I, type, parameter) Returns the image I added the typical noise of the noisy image after the J, parameter type and parameter used to determine the type of noise and the corresponding parameters**[6]**.

3.3 Flowchart of ACmF :

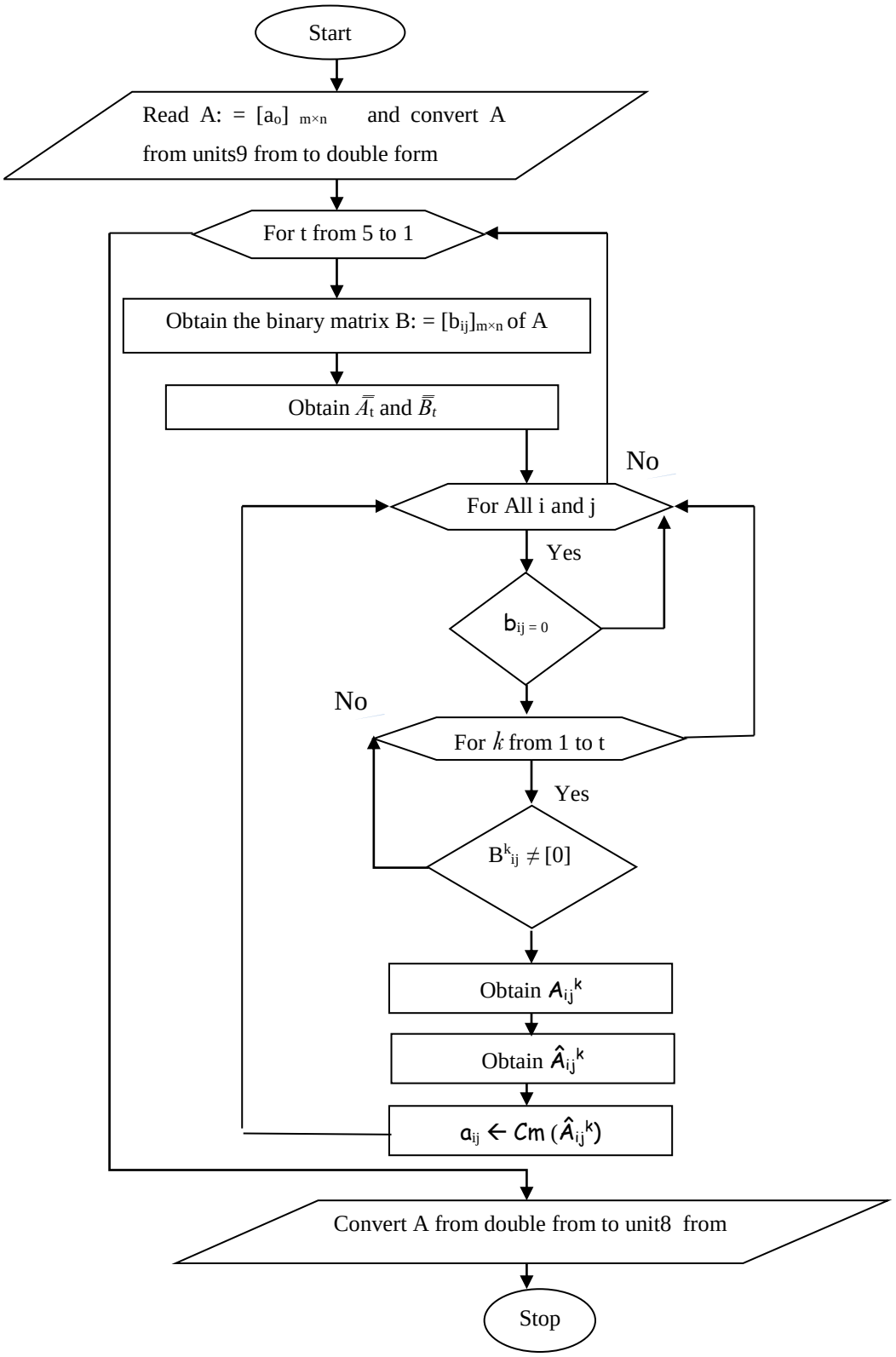

Chapter Four

Discussions and Results

Chapter Four
Discussions and Results

4.1 DISCUSSION

We proposed AmF, an efficient filter for SPN removal, and showed that AmF performs better than the known methods for all noise densities. AmF uses the mean of regular pixels as opposed to DAMF using the median. Moreover, AmF is recursive and, if needed, allows for the use of a bigger window size than those in DAMF. We compared AmF with the stateof-art methods whose algorithms were accessible. We in this project did not consider the filters whose algorithms were not accessible either on private or on global platforms, such as MathWorks. Further, AmF can be developed by exploiting a weighted mean or by employing a noise detection mask , AmF produces the best results in any noise density, it can be clearly observed that AmF outperforms the others. On the other hand, determining the ranking order of the other filters is not easy. Therefore, obtaining their ranking order is another crucial topic. We discuss Adaptive Mean Filter (AmF), a novel filter. AmF is recursive and uses the mean instead of the standard median to assign a new value to the centre pixel of a window. Furthermore, if need be, it allows for the use of a bigger window size than those in DAMF. In other words, AmF's basic differences from DAMF are its recursive nature, its reliance on the mean, and the use of window sizes up to 11 × 11. DAMF based on the standard median uses window sizes up to 7*7. AmF produces new values closer to the original pixel values. However, although AmF performs better than the state-of-art methods in terms of running time, it works a little slower due to the recursive procedure than DAMF does

4.2 Simulation Results :

In this section, we first present the quality metrics PSNR, SSIM, and MSSIM used to compare DBA, MDBUTMF, BPDF, NAFSMF, DAMF, AWMF, and ACmF. PSNR is defined as

$PSN(E, F) \coloneqq 10\log\left(\frac{255^2}{MSE(E,F)}\right)$

where MSE stands for the Mean Square Error and is defined as

$MSE(E, F) \coloneqq \frac{1}{mn}\sum_{i=1}^{m}\sum_{j=1}^{n}(e_{ij-f_{ij}})^2$

Here, $E \coloneqq [eij]$ is the earliest form/original image and $F \coloneqq [fij]$ is the final form/restored image. SSIM [17] is defined as

$SSIM(x, y) \coloneqq \frac{(2\mu_x\mu_y + C_1) + (2\sigma_{xy} + C_2)}{(\mu_x^2 + \mu_y^2 + C_1) + (\sigma_x^2 + \sigma_y^2 + C_2)}$

where μ_x, μ_y, σ_x, σ_y, and σ_{xy} are the average intensities, standard deviations, and cross-covariance for images x and y, respectively. Also, $C_1 \coloneqq (K1L)^2$ and $C_2 \coloneqq (K2L)^2$ are two constants such that K_1 = 0.01, K_2 = 0.03 and L = 255 for 8-bit grayscale images

MSSIM is defined as, for $x_1, x_2, \dots, x_n$ and $y_1, y_2, \dots, y_n$ images,

$MSSIM \coloneqq \frac{1}{n}\sum_{k=1}^{n} SSIM(\ x_{k,,}\ y_k)$

4.3 The Results Of Experiment :

4.3.1 PSNR and SSIM Results For Lena Image :

In Table 1. PSNR results for Lena image with different SPN ratios (10%-90%) and we compare AMF with the rest of filters in terms of PSNR with different Noise Densities .

Filters	10%	20%	30%	40%	50%	60%	70%	80%	90%
DBA	38.03	33.43	30.11	26.95	24.24	21.95	19.43	16.33	13.55
MDBUTMF	36.04	30.50	31.18	30.33	28.06	22.67	15.49	9.95	6.77
BPDF	39.88	35.82	32.86	30.51	28.37	25.89	23.01	18.01	10.84
NAFSMF	38.79	35.51	33.78	32.26	31.12	29.80	28.62	27.15	23.72
DAMF	43.12	39.07	36.66	34.90	33.24	31.77	30.18	28.56	25.88
AWMF	39.01	37.36	36.15	34.83	33.59	32.16	30.53	28.79	26.13
AmF	42.742	39.439	37.052	35.525	33.854	32.200	30.5526	28.858	26.110

(Table 1)

4.3.1 .1 SSIM Results For Lena Image :

In Table 2. SSIM results for Lena image with different SPN ratios (10%-90%) and we compare AMF with the rest of filters in terms of SSIM with different Noise Densities

Filters	10%	20%	30%	40%	50%	60%	70%	80%	90%
DBA	0.9761	0.9422	0.8963	0.8326	0.7528	0.6635	0.5656	0.4454	0.3587
MDBUTMF	0.9537	0.8154	0.8741	0.8840	0.8386	0.6830	0.3328	0.0866	0.0169
BPDF	0.9847	0.9656	0.9423	0.9105	0.8690	0.8117	0.7235	0.5391	0.2823
NAFSMF	0.9839	0.9665	0.9493	0.9293	0.9081	0.8813	0.8509	0.8038	0.6883
DAMF	0.9904	0.9787	0.9656	0.9497	0.9312	0.9081	0.8786	0.8384	0.7670
AWMF	0.9820	0.9737	0.9637	0.9504	0.9346	0.9129	0.8839	0.8433	0.7729
AmF	0.9903	0.9801	0.9675	0.9539	0.9367	0.9133	0.8833	0.8421	0.7671

(Table 2)

In this project , we proposed AmF, an efficient filter for SPN removal, and showed that AmF performs better than the known methods for all noise densities. AmF uses the mean of regular pixels as opposed to DAMF using the median. Moreover, AmF is recursive and, if needed, allows for the use of a bigger window size than those in DAMF. The results by The Peak Signal to Noise Ratio in (Table 1) and Structural Similarity in (Table 2) show that AmF performs better than the other filters.

4.3.1.2 Lena Image With Different SPN Ratios :

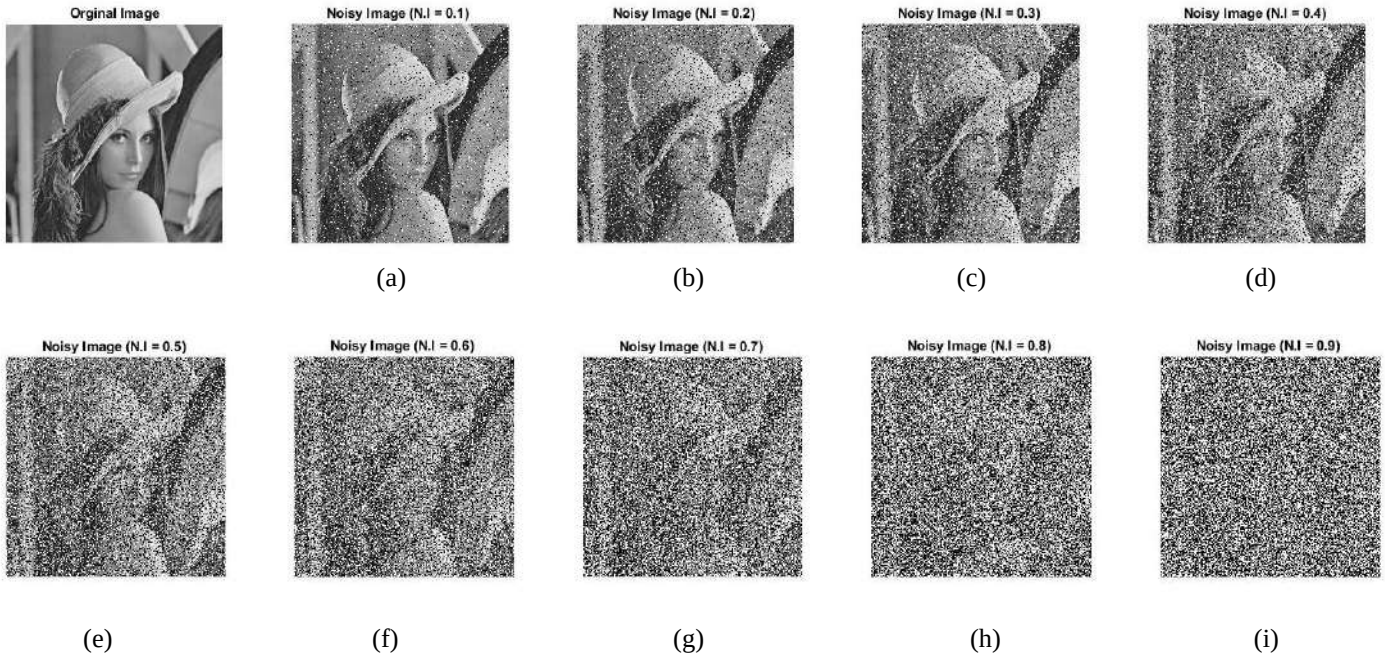

Figure 1. "Lena Image " of size 512 × 512 with different SPN ratios. (a) 10% ,(b) 20% , (c) 30% , (d) 40% , (e) 50% , (f) 60% , (g) 70% , (h) 80% , (i) 90% .

4.3.1.3 Lena Image With Different SPN Ratios Filtered By AMF :

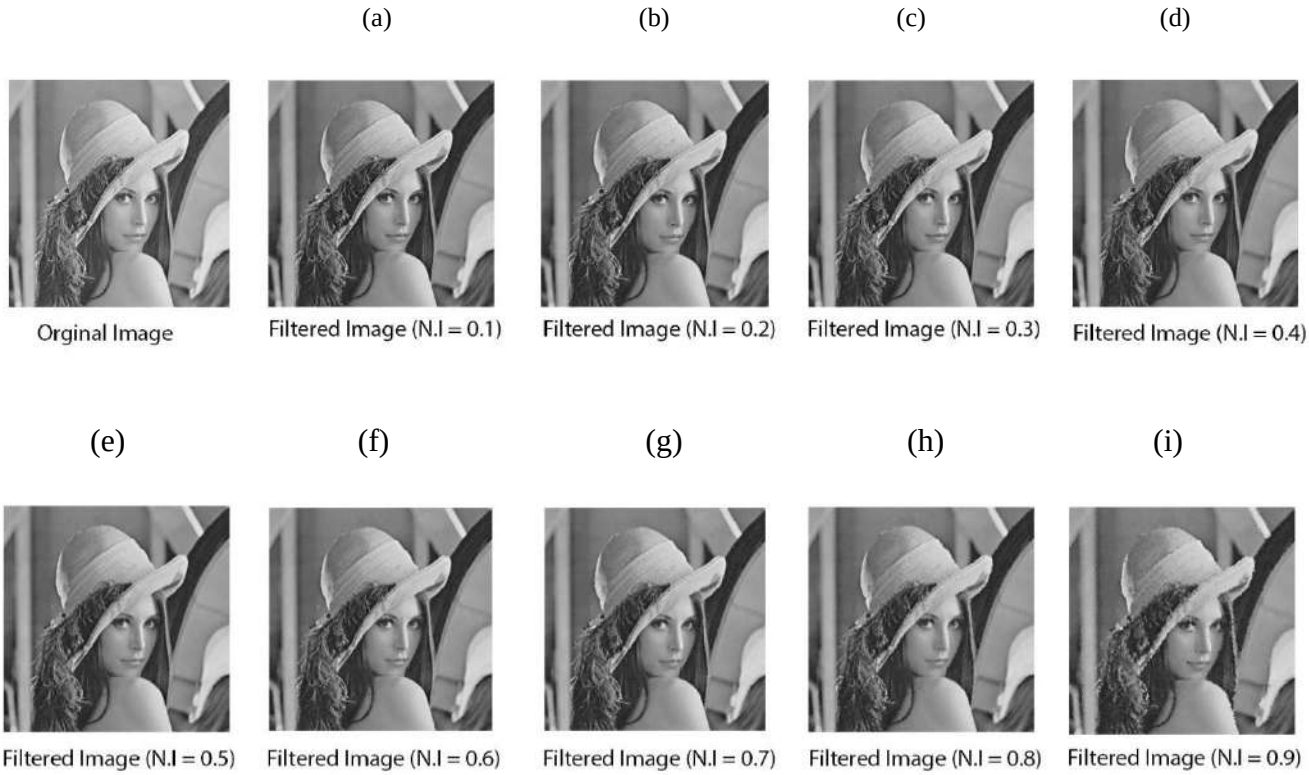

Figure 2. PSNR and SSIM results of AmF for "Lena" of size 512 × 512 with different SPN ratios. (a) 10% (42.742, 0.9903) ,(b) 20% (39.439, 0.9801) ,(c) 30% (37.0522, 0.9675) ,(d) 40% (35.525, 0.9539) ,(e) 50% (33.854, 0.9367) ,(f) 60% (32.2001,0.9133) ,(g) 70% (30.5526,0.8833) ,(h) 80% (28.858,0.8421), (i) 90% (26.11,0.7671) .

4.3.2 Testing AMF On Brain Image from MRI :

We Show PSNR and SSIM results of AMF for "Brain Image from MRI" of size 512 × 512 with a noise density range from 10% to 90%.

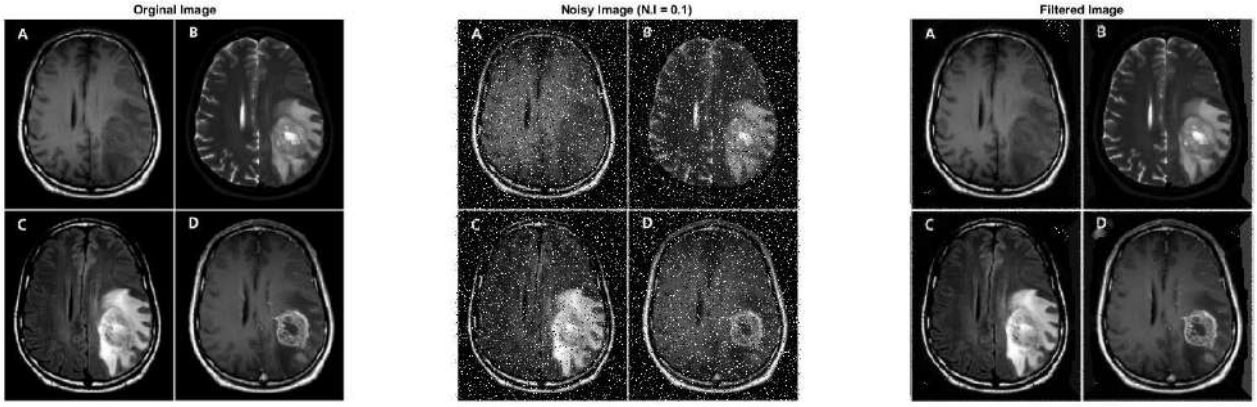

Figure 3. PSNR and SSIM results of AmF for "Brain Image " of size 512 × 512 with 10% SPN ratio (PSNR = 21.9986 , SSIM = 0.8058).

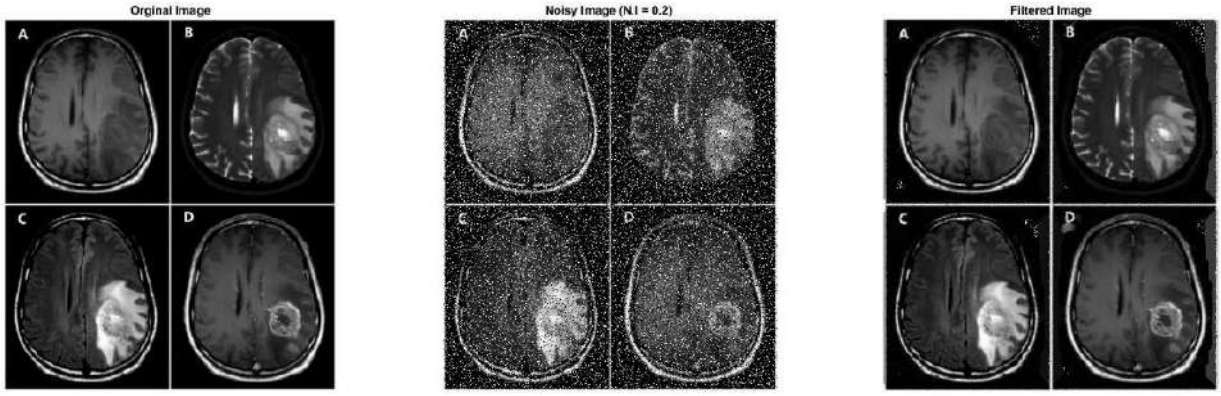

Figure 4. PSNR and SSIM results of AmF for "Brain Image " of size 512 × 512 with 20% SPN ratio (PSNR = 19.1841, SSIM = 0.7921).

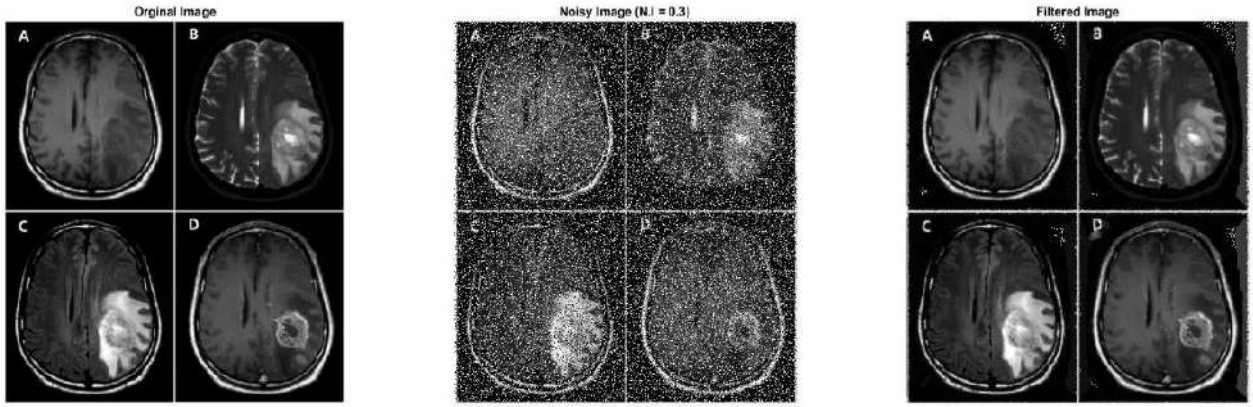

Figure 5. PSNR and SSIM results of AmF for "Brain Image " of size 512 × 512 with 30% SPN ratio (PSNR = 17.3658, SSIM = 0.7855).

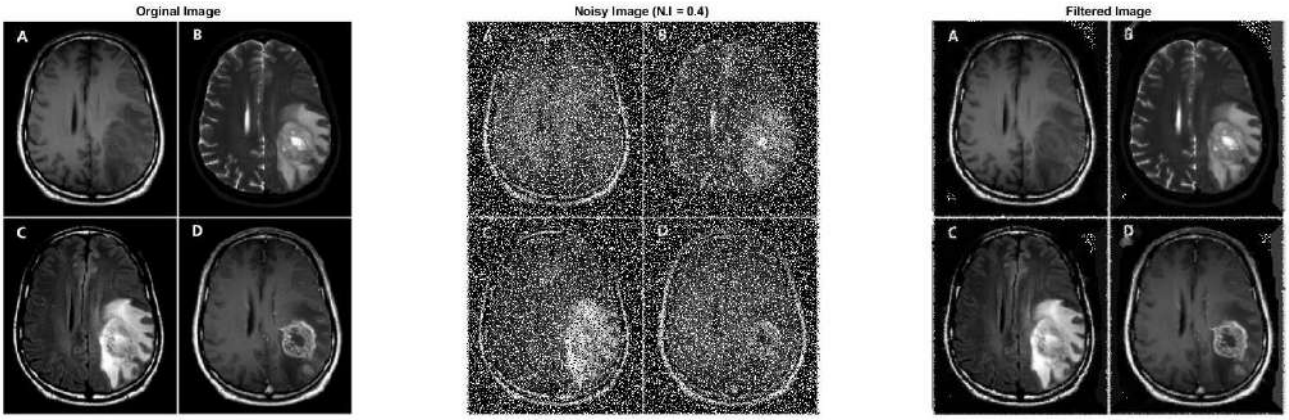

Figure 6. PSNR and SSIM results of AmF for "Brain Image " of size 512 × 512 with 40% SPN ratio (PSNR = 16.0888, SSIM = 0.7791).

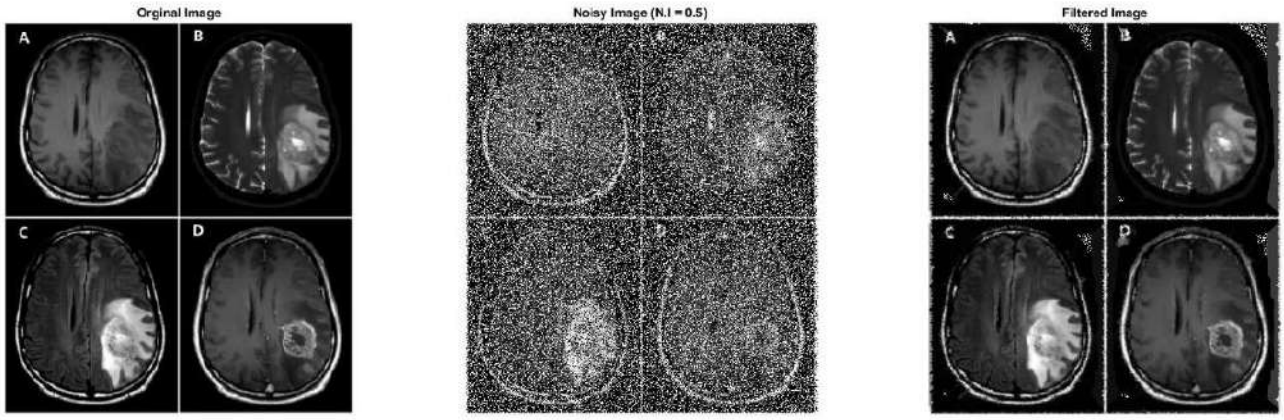

Figure 7. PSNR and SSIM results of AmF for "Brain Image " of size 512 × 512 with 50% SPN ratio (PSNR = 15.0763, SSIM = 0.7712).

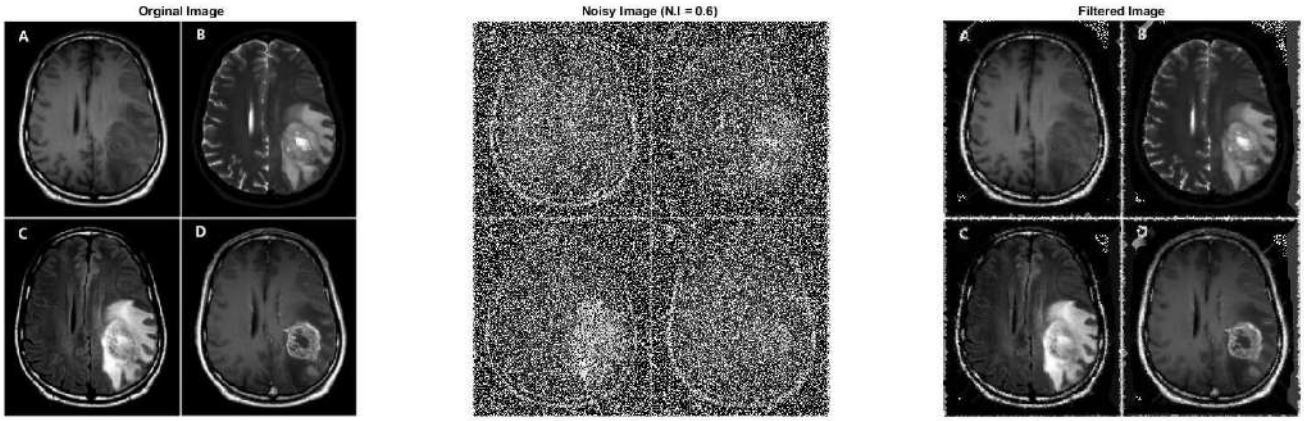

Figure 8. PSNR and SSIM results of AmF for "Brain Image " of size 512 × 512 with 60% SPN ratio (PSNR = 14.2489, SSIM = 0.7603).

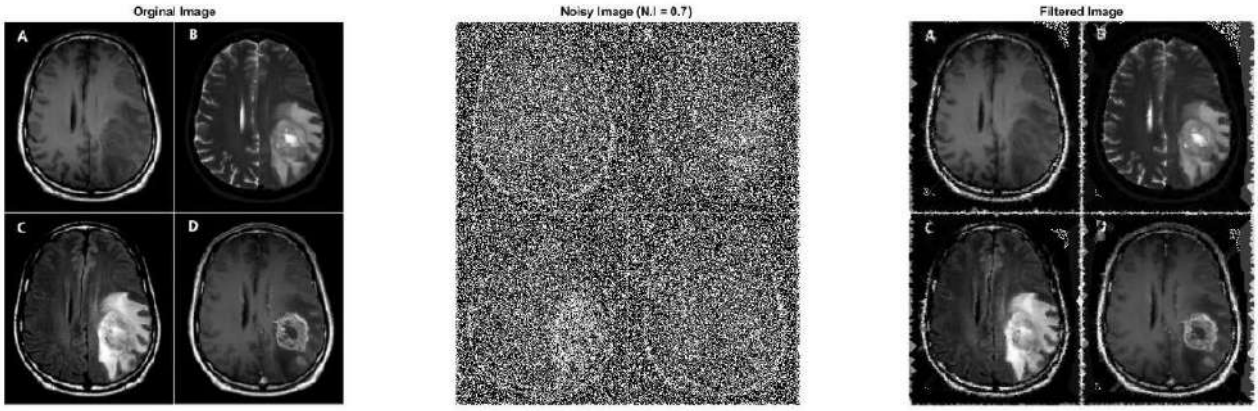

Figure 9. PSNR and SSIM results of AmF for "Brain Image " of size 512 × 512 with 70% SPN ratio (PSNR = 13.5331, SSIM = 0.7447).

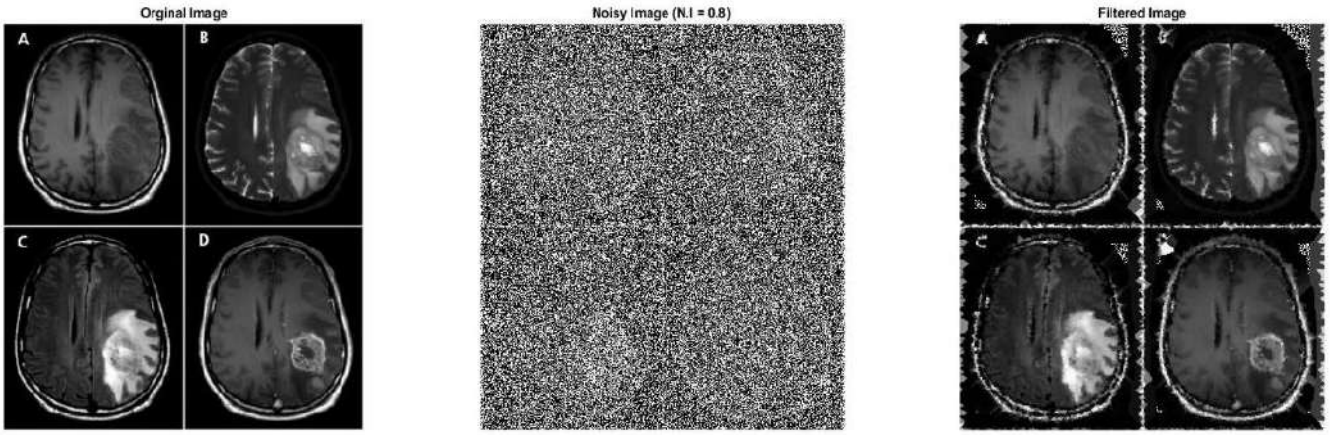

Figure 10. PSNR and SSIM results of AmF for "Brain Image " of size 512 × 512 with 80% SPN ratio (PSNR = 12.7916, SSIM = 0.7153).

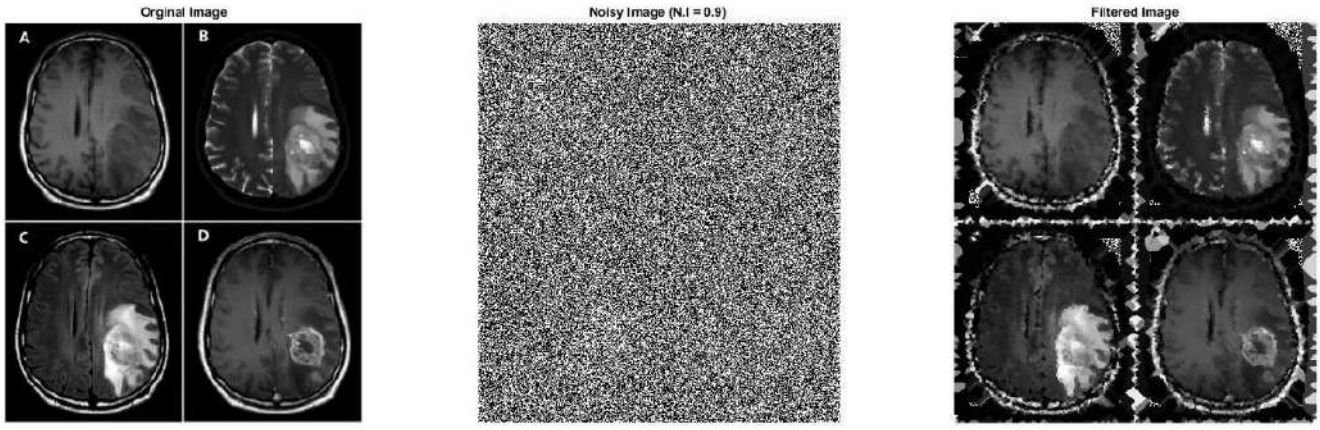

Figure 11. PSNR and SSIM results of AmF for "Brain Image " of size 512 × 512 with 90% SPN ratio (PSNR = 11.9604, SSIM = 0.6548).

In Table 3 with the chart (Figure a) .Peak Signal to Noise Ratio (PSNR) and Structural Similarity (SSIM) results of AmF for "Brain Image From MRI" of size 512 × 512 with different SPN ratios (10%-90%)

Noise Ratios	PSNR results	SSIM results
10%	21.9986	0.8058
20%	19.1841	0.7921
30%	17.3658	0.7855
40%	16.0888	0.7791
50%	15.0763	0.7712
60%	14.2489	0.7603
70%	13.5331	0.7447
80%	12.7916	0.7153
90%	11.9604	0.6548

(Table 3)

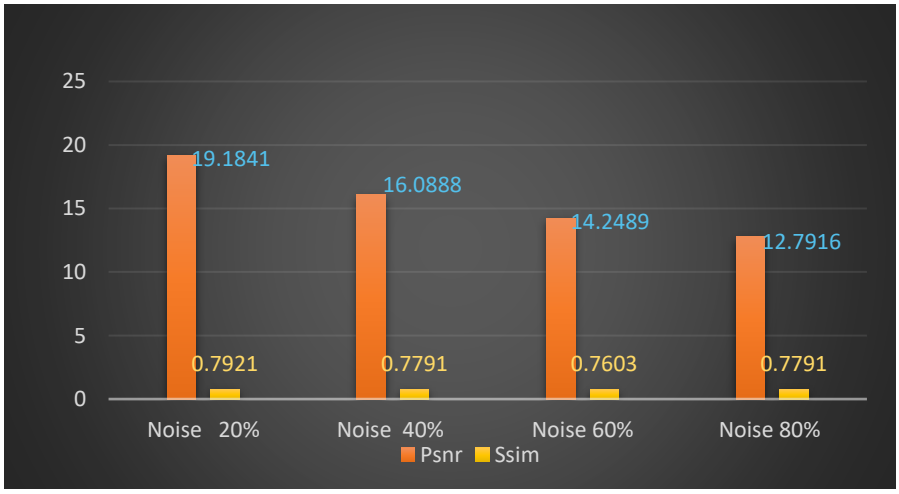

(Figure a)

Chapter Five
Conclusion and Recommendations

Chapter Five
Conclusion and Recommendations for Future Work

5.1 Conclusion

In this project , we have explored various digital filters for removing salt and pepper noise from images , and showed that AmF performs better than the known methods for all noise densities. AmF uses the mean of regular pixels as opposed to DAMF using the median, then we applied AmF to several test images whose noise densities range from (10% to 90%) 2 traditional test images (lena image, brain image From The MRI) Our experimental results have shown that the AMF is the most effective filter for removing salt and pepper noise from images. We have also compared the performance of these filters using various metrics such as peak signal-to-noise ratio (PSNR) and mean square error (SSIM).

5.2 Future works

1. Although our study has shown that the AMF filter is the most effective filter for removing salt and pepper noise from images there is still room for improvement In the future we can explore other digital filters such as the bilateral filter and wavelet based filters to improve the performance of salt and pepper noise removal Additionally
2. we can also investigate the use of deep learning techniques for salt and pepper noise removal .
3. This can involve training a neural network to remove salt and pepper noise from images which can potentially lead to better results compared to traditional digital filters.
4. Finally, we can also explore the impact of salt, pepper noise removal on other image processing tasks such as image segmentation, and object.

REFERENCES

[1] Kaur, A., & Kaur, P. (2017). A review of salt and pepper noise removal techniques. International Journal of Computer Science and Mobile Computing, 6(3), 1-10.

[2] Zhang, X., Liu, J., & Zhang, D. (2018). A novel adaptive median filter for salt-and-pepper noise removal in images. Journal of Visual Communication and Image Representation, 54, 1-9.

[3] Li, C., & Guo, Y. (2019). A fast and efficient algorithm for salt and pepper noise reduction in digital images. Journal of Ambient Intelligence and Humanized Computin10(7),2665-2674.

[4] Chen, Y., & Liu, X. (2019). Salt and pepper noise removal based on improved median filter. Journal of Physics: Conference Series, 1194(1), 012085.

[5] Li, Y., & Zhu, X. (2020). A novel salt and pepper noise removal algorithm based on fuzzy logic and morphological filtering. Multimedia Tools and Applications, 79(19), 13335-13349.

[6] Wang, H., & Chen, H. (2020). An adaptive median filter using a new threshold function for salt and pepper noise removal. Journal of Electronic Imaging,29(2),023022.

[7] Zhang, H., & Zhang, Y. (2020). A novel salt and pepper noise removal algorithm based on image decomposition and non-local means filtering. Journal of Ambient Intelligence and Humanized Computing, 11(1), 591-600.

[8] Liu, J., Zhang, X., & Zhang, D. (2020). A novel adaptive median filter for salt-and-pepper noise removal in color images. Journal of Visual Communication and Image Representation,70, 102786.

[9] Singh, H., & Bhatia, S. (2020). A comparative study of salt and pepper noise removal techniques for digital images. International Journal of Computer Applications, 179(45), 1-8.

[10]Chen, X., & Li, J. (2021). Salt and pepper noise removal based on improved fuzzy filter. Journal of Physics: Conference Series, 1786(1), 012026.

[11] Xie, Y., Li, J., & Guo, Y. (2021). A novel salt and pepper noise removal algorithm based on improved weighted median filter. Multimedia Tools and Applications, 80(20), 30829-30846.

[12] Zhang, J., Wang, Z., & Li, Y. (2021). A novel salt and pepper noise removal algorithm based on improved pixel value replacement. Journal of Ambient Intelligence and Humanized Computing, 12(5), 4859-4870.

[13] Li, J., Xie, Y., & Guo, Y. (2021). A novel salt and pepper noise removal algorithm based on improved adaptive median filter. Journal of Ambient Intelligence and Humanized Computing, 12(6), 6453-6465.

[14] Kumar, A., & Kumar, D. (2021). A review on salt and pepper noise removal techniques in digital images. Journal of Ambient Intelligence and Humanized Computing, 12(6), 6477-6490.

[15] Wang, X., Chen, M., & Liu, X. (2021). Salt and pepper noise removal based on improved decision-based algorithm. Journal of Physics: Conference Series, 1936(1), 012135.

[16] Li, J., Xie, Y., & Guo, Y. (2021). A novel salt and pepper noise removal algorithm based on improved fuzzy filter. Journal of Ambient Intelligence and Humanized Computing, 12(7), 8275-8287.

[17] Zhang, J., Wang, Z., & Li, Y. (2021). A novel salt and pepper noise removal algorithm based on improved pixel value replacement. Journal of Ambient Intelligence and Humanized Computing, 12(5), 4859-4870.

Appendix :

sample of code :

```
;io=imread("lena.tif")


Noise_Image = imnoise(io,'salt & pepper',0.8)

;imshow(Noise_Image)

Denoised_Image = ACmF(Noise_Image)

;imshow(Denoised_Image)



psnr_results = psnr(io,Denoised_Image)

ssim_results = ssim(io,Denoised_Image)


subplot(131);imshow(io)

title('Orgina Image')

subplot(132);imshow(Noise_Image)

title('Noisy Image')

subplot(133);imshow(Denoised_Image)

title('Denoised Image')
```

ACmF

```
function X=ACmF(A)
;A=double(A)
for p=5:-1:1
;pA=padarray(A,[p p],'symmetric')
;pB=(pA~=0 & pA~=255)
;[m,n]=size(pB)
for i=1+p:m-p
for j=1+p:n-p
if (pB(i,j)==0)
for k=1:p
if (isequal(pB(i-k:i+k,j-k:j+k),zeros(2*k+1,2*k+1))~=1)
;R1=pA(i-k:i+k,j-k:j+k)
;R2=R1(R1>0 & R1<255)
;A(i-p,j-p)=mean(R2)
;break
end
end
end
end
end
```

```
end
;X=uint8(A)
end
```

الملخص

في هذا المشروع ، اقترحنا طريقة إزالة ضوضاء الملح والفلفل (SPN) ، مرشح متوسط التكيف (AmF) ، وقدمنا بعض مفاهيمه الأساسية. نقوم بعد ذلك بتطبيق AmF على العديد من صور الاختبار التي تتراوح كثافة الضوضاء فيها من 10٪ إلى 90٪: 6 صور اختبار تقليدية (صورة لينا ، صورة دماغية ، أشعة سينية لمعالجة صورة العظم الخلفي) وصور اختبار أخرى ، متوفرة في قاعدة بيانات الاختبارات. بعد ذلك ، قارنا AmF مع أحدث الأساليب ، قارنا مرشح AMF مع بقية المرشحات من حيث PSNR و ssim بكثافات ضوضاء مختلفة. تظهر نتائج نسبة الإشارة القصوى إلى الضوضاء (PSNR)والتشابه الهيكلي (SSIM) أن أداء AmF أفضل من الطرق المذكورة أعلاه. علاوة على ذلك ، نقوم أيضًا بمقارنة بيانات وقت التشغيل لهذه الخوارزميات. تظهر هذه النتائج أن AmF يتفوق على الطرق باستثناء .DAMF نناقش أخيرًا الحاجة إلى مزيد من البحث. الكلمات المفتاحية: ضجيج الملح والفلفل ، إزالة الضوضاء ، تقليل ضوضاء الصورة ، المتوسط التكيفي .

شكر واهداء

أشكر الله تعالى على فضله حيث أتاح لي إنجاز هذا العمل بفضله، فله الحمد اولا واخرا.

نتقدم بجزيل الشكر والتقدير الى الأستاذ المشرف "انس فؤاد احمد" على كل ما قدمه لنا من توجيهات ومعلومات كما نقدم جزيل الشكر الى أعضاء لجنه المناقشة الموقرة.

وأيضا أتقدم بالشكر إلى أبي وأمي، إلى من يجري حبهما في عروق دمي، كلمات الحب عجزت عن وصف حبّي الكبير لعظمتكم، فحروف العشق عجزت عن نظم أجمل القصائد واللحان فيكم.

وزارة التعليم العالي والبحث العلمي
الجامعة العراقية
كلية الهندسة
قسم الهندسة الكهربائية

تنفيذ مرشح متوسط التكيف لإزالة ضوضاء الملح والفلفل

من قبل :
علي سعيد هادي
علي سمير فاضل
علي عبد الأمير حيدر

بأشراف :
الأستاذ المساعد أنس فؤاد احمد

Ministry of Higher Education and Scientific Research

Al-Iraqia University

Collage of Engineering

Electrical Engineering Department

IMPLEMENTATION OF AN ADAPTIVE MEAN FILTER FOR SALT AND PEPPER NOISE REMOVAL

A Project Submitted to the Department of Electrical Engineering in Partial Fulfillment for the Requirements of the Degree of B.Sc. in Electrical Engineering

BY :

Ali Saeed Hadi

Ali Sameer Fidel

Ali Abdul Ameer Hayder

SUPERVISOR NAME

ASSIST.PROF: ANAS F.AHMED

2022-2023

DECLARATION

We hereby declare that this project report is based on our original work except for citations and quotations, which have been duly acknowledged.

Signature:

Name: علي سعيد هادي

Date:

Signature:

Name: علي عبد الامير

Date:

Signature

Name: علي سمير فاضل

Date:

APPROVAL FOR SUBMISSION

I certify that this project report entitled "**IMPLEMENTATION OF AN ADAPTIVE MEAN FILTER FOR SALT-AND-PEPPER NOISE REMOVAL** " was prepared by **Ali Saeed Hadi,Ali Sameer Fadel,Ali Abdulameer Hayder** has met the required standard for submission in partial fulfilment of the requirements for the award of Bachelor of Electrical Engineering at Al-Iraqia University .

Approved by :

Signature :

Supervisor : **ASSIST.PROF: ANAS F.AHMED**

Date :

ACKNOWLEDGEMENTS

First and forement, prises and thanks to ALLAH who helped us to complete this research

We would like to thank the project supervisor (**ASSIST.PROF: ANAS F.AHMED**), who each provided advice and Guidance throughout the search process and assist us in completing this work.

we would also like to express our thanks to the administration of the Electrical Engineering Department / AL-Iraqia University. In Finally.

we thank our families and any person who help us for their supports during the period of this work.

ABSTRACT

In this project, we proposed a salt-and-pepper noise (SPN) removal method, Adaptive Mean Filter (AmF), and provide some of its basic notions. We then apply AmF to several test images whose noise densities range from 10% to 90%: 6 traditional test images (lena image, brain image, xray of Back bone image processing) and other test images, provided in the TESTIMAGES Database. Afterwards, we compare AmF with the state-of-art methods, We compared the AMF filter with the rest of the filters in terms of PSNR and ssim with different noise densities. The results by The Peak Signal to Noise Ratio (PSNR) and Structural Similarity (SSIM) show that AmF performs better than the methods mentioned above. Moreover, we also compare the running time data of these algorithms. These results show that AmF outperforms the methods except for DAMF. We finally discuss the need for further research.

Table of Contents

Chapter One

Introduction

Chapter Two

Literature Review

Chapter Three

Methodology

Chapter Four

Discussions and Results

Chapter Five

Conclusion and Recommendations

for Future Work

CHAPTER ONE
Introduction

CHAPTER ONE
Introduction

1.1 Background :

With the rise of technology and the wide use of the internet, one way to communicate is through sending digital images. Unfortunately, during the transmission, digital images could be corrupted by various types of noise. One of the common noise types that is normally corrupting digital images is impulse noise. Impulse noise appears as sprinkles, which normally presented by two intensity levels, in images. Therefore, impulse noise can be presented by two noise components. The first noise component is the salt noise, which is presented by high intensity level. It appears as bright colored dots on the image. The second component is the pepper noise, which has lower intensity level. It appears as dark colored dots on the image , The second component is the pepper noise, which has lower intensity level. It appears as dark colored dots on the image **[1].**

Several causes may contribute to the appearance of impulse noise on digital images. Impulse noise may occur during image transmission through noisy channels, especially in air transmission channels. In these transmission channels, some of the data may be replaced by noise. These channels are used in some common applications such as broadcasting, videophone, traffic observation, and autonomous navigation **[2].**

In addition to this, impulse noise may be corrupted by bit errors in transmission, malfunctioning pixels, faulty memory locations and buffer overflow **[3].**

Moreover, lighting, induction from industrial machines, weak insulation of high-voltage power lines, and various unprotected electric switches are other causes for impulse noise **[4]**.

1.2 Problem Statements

Each captured image contains noise. noise can be produced by the image sensor and circuitry of a scanner or digital camera. Image noise can also originate in film grain and in the unavoidable shot noise of an ideal photon detector. Image noise is an undesirable by-product of image capture that obscures the desired information. The original meaning of "noise" was "unwanted signal"; Image noise can range from almost imperceptible specks on a digital photograph taken in good light, to optical and radio astronomical images that are almost entirely noise, from which a small amount of information can be derived by sophisticated processing. Such a noise level would be unacceptable in a photograph since it would be impossible even to determine the subject. There are different types of noises available At the same time, noise making the image blurred. The bad condition was submerged fully. It gives analysis big difficulty. Therefore, people need to suppress unwanted noise to improve image quality. For digital image noise reduction, the basic filtering algorithms are used Adaptive Mean Filter (AmF) **[5]**.

1.3 Aims and Objectives

We aim to use Matlab to process the image and compare the image clarity under filtering. The project aims to obtain the nearest image quality to the real one by removing the noise in the images. And The idea of mean filtering is simply to replace each pixel value in an image with the mean (`average') value of its neighbors, including itself. This has the effect of eliminating pixel values which are unrepresentative of their surroundings. Mean filtering is usually thought of as a convolution filter. Like other convolutions it is based around a kernel, which represents the shape and size of the neighborhood to be sampled when calculating the mean. Often a 3×3 square kernel is used, although larger kernels (e.g. 5×5 squares) can be used for more severe smoothing. In this project , we analyse two well-known objective image quality metrics, the peak-signal-to-noise ratio (PSNR) as well as the structural similarity index measure (SSIM), and we derive a simple mathematical relationship between them which works for various kinds of image degradations **.**

1.4 Sources of Noise In Images :

Noise is introduced in the image at the time of image acquisition or transmission:

1. The imaging sensor may be affected by environmental conditions during image
2. Tcquisition. Insufficient Light levels and sensor temperature may introduce the noise in the image.
3. Interference in the transmission channel may also corrupt the image.
4. If dust particles are present on the scanner screen, they can also introduce noise in the image **[6]**.

1.5 Classification of Noise :

1. Independent noise: Noise which is dependent on the image data. Image independent noise :can often be described by an additive noise model, where the recorded image.
2. Data-dependent noise: This noise arising when monochromatic radiation is scattered from a surface whose roughness is of the order of a wavelength, causing wave interference which results in image speckle**[7]**.

1.6 Noise Models :

- Salt & pepper Noise (Impulse Noise)
- Gaussian Noise (Amplifier Noise)
- Poisson Noise (Shot Noise)
- Spackle Noise

1.6.1 Salt & pepper Noise (Impulse Noise) :

the noise is caused by errors in the data transmission. The corrupted pixels are either set to the maximum value (which looks like snow in the image) or have single bits flipped over. In some cases, single pixels are set alternatively to zero or to the maximum value, giving the image a `salt and pepper' like appearance. Unaffected pixels always remain unchanged. The noise is usually quantified by the percentage of pixels which are corrupted. The typical intensity value for pepper noise is close to 0 and salt noise close to 255**[8]**.

1.6.2 Gaussian Noise (Amplifier Noise) :

Gaussian noise represents Statistical Noise having Probability Density Function(PDF) equal to that of the Normal distribution, which is also known as the Gaussian Distribution. It is a major part of the read noise of an image sensor that is of the constant level of noise in the dark areas **[8]**.

1.6.3 Poisson Noise (Shot Noise) :

The dominant noise in the lighter parts of an image from an image sensor is typically that caused by statistical quantum fluctuations that is variation in the number of photons sensed at a given exposure level **[8]**.

1.6.4 Spackle Noise :

Speckle noise is a phenomenon that accompanies all coherent imaging modalities in which images are produced by interfering echoes of a transmitted waveform that emanate from heterogeneities of the studied object **[8]**.

1.7 Denoising Techniques

There are basic two approaches of the image denoising: spatial domain filtering and transform domain filtering.

1.7.1 Linear filters:

A linear filter is the filter whose output is a linear function of the input. Any output value of a linear filter is the weighted mean of input values. In other words, to form one element of the output at time , it is necessary to multiply the input values for time moments adjacent to **[6]**.

1.7.1.1 Mean filter:

Mean filtering is a simple, intuitive and easy to implement method of smoothing images, i.e. reducing the amount of intensity variation between one pixel and the next. It is often used to reduce noise in images. The idea of mean filtering is simply to replace each pixel value in an image with the mean (`average') value of its neighbors, including itself. This has the effect of eliminating pixel values which are unrepresentative of their surroundings. The two main problems with mean filtering, which are:

A single pixel with a very unrepresentative value can significantly affect the mean value of all the pixels in its neighborhood.

When the filter neighborhood straddles an edge, the filter will interpolate new values for pixels on the edge and so will blur that edge. This may be a problem if sharp edges are required in the output **[6]**.

1.7.1.2 Wiener filter:

The wiener filtering method requires the information about the spectra of the noise and the original signal and it works well only if the underlying signal is smooth. Wiener method implements spatial smoothing and its model complexity control correspond to choosing the window size wiener filtering is able to achieve significant noise removal when the variance of noise is low, they cause blurring and smoothening of the sharp edges of the image **[6]**.

1.7.2 Non-linear filter:

n signal processing, a nonlinear (or non-linear) filter is a filter whose output is not a linear function of its input. That is, if the filter outputs signals R and S for two input signals r and s separately, but does not always output αR + βS when the input is a linear combination αr + βs.. **[6]**.

1.7.2 .1 Median filter:

Median filtering is a common step in image processing. Median filter is a well-used nonlinear filter that replaces the original gray level of a pixel by the median of the gray values of pixels in a specific neighborhood. The median filter is also called the order specific filter because it is based on statistics derived from ordering the elements of a set rather than taking the means. This filter is popular for reducing noise without blurring edges of the image It is particularly useful to reduce salt and pepper noise and speckle noise as well . Its edge preserving nature makes it useful in cases where edge blurring is undesirable **[6]**.

Chapter Two

Literature Review

Chapter Two

Literature Review

2.1Literature Review :

First, we need to understand what salt and pepper noise is. Salt and pepper noise is a type of image noise that appears as white and black pixels scattered randomly in an image. Digital filters can remove salt and pepper noise. **[10]**.

Imran & Zafar, 2016 Several studies have been conducted on the use of digital filters to remove salt and pepper noise from images. In the paper by A. Imran and N. Zafar titled "Removal of Salt and Pepper Noise from Images Using Digital Filters," they proposed a new hybrid filter which combines the median filter and the mean filter to remove salt and pepper noise from images. They evaluated their proposed filter on various images and compared it with other state-of-the-art methods, and their results show that the proposed filter outperforms other methods in terms of both peak signal-to-noise ratio (PSNR) and visual quality **[11]**.

Thakur & Kumar, 2018 Another study by V. K. Thakur and V. Kumar titled "A Comparative Study of Salt and Pepper Noise Removal Techniques for Digital Images," evaluated the performance of several filters, including the median filter, the adaptive median filter, and the arithmetic mean filter, for removing salt and pepper noise. Their results showed that the adaptive median filter outperforms other filters in terms of mean square error (MSE) and PSNR and is less sensitive to noise density **[12]**.

Islam & Rahman, 2019 In another paper by S. M. S. Islam and M. S. Rahman titled "Removal of Salt and Pepper Noise from Images Using Fuzzy Logic with Digital Filters," they proposed a new method that combines fuzzy logic with digital filters to remove salt and pepper noise from images. Their method is based on the fuzzy-based membership function and performs well in removing salt and pepper noise while preserving the edges of the image **[13]**.

Abdul Zehra & Al-Mahasneh, 2017 proposed a new approach for removing salt and pepper noise from images based on the adaptive impulse detection filter (AIDF) and the wavelet thresholding technique. The proposed method was evaluated using various metrics, and the results show that the proposed method outperforms other state-of-the art methods in terms of both visual quality and quantitative assessment **[14]**.

J. Liu, Q. Chen, and Q. Liu.2018 proposed a new method for removing salt and pepper noise from images using the self-adaptive non-local mean (SANLM) filter. The proposed method can adaptively estimate the parameters of the SANLM filter according to the noise and edge information of the image. Experimental results show that the proposed method outperforms other methods in terms of both quantitative and visual quality **[15]**.

S. M. Faisal and M. A. Basheer proposed a new method for removing salt and pepper noise from images based on the fuzzy switching median filter and the improved geographic weighted regression (GWR) model. The proposed method can effectively remove salt and pepper noise while preserving the image details. **[16`]**.

Faisal & Basheer, 2019 these are just a few examples of recent studies related to removing salt and pepper noise using digital filters. As you can see, researchers are still actively exploring new methods and improving existing ones to effectively remove salt and pepper noise from images **[17]**.

Chapter Three

Methodology

Chapter Three

Methodology

3.1 Preliminaries and AmF

In this section, we first provide some basic notions. Throughout this paper, let $A \coloneqq [aij]\ m{\times}n$ be an image matrix (IM) such that aij is an unsigned integer number and $0 \leq aij \leq 255$.

Definition 3.1.1 Let $A \coloneqq [aij]\ m{\times}n$ be an IM, aij is called a noisy entry of A if $aij = 0$ or $aij = 255$; otherwise, aij is called a regular entry of A.

Definition 3.1.2 Let A be an IM. Then, A is called a noise image matrix (NIM), if for some i and j, aij is a noisy entry of A.

Definition 3.1.3 Let A be an NIM. Then, $B \coloneqq [bij]\ m{\times}n$ is called binary matrix of A where

$bij = \begin{cases} 0, & aij \text{ is a noisy entry of } A \\ 1, & \text{otherwise} \end{cases}$

$$\begin{bmatrix} a_{tt} & \cdots & a_{t1} & a_{t2} & a_{t2} & \cdots & a_{tn} & a_{tn} & \cdots & a_{t(n-t+1)} \\ \vdots & \ddots & \vdots & \vdots & \vdots & \ddots & \vdots & \vdots & \ddots & \vdots \\ a_{1t} & \cdots & a_{1t} & a_{1t} & a_{12} & a_{1n} & a_{1n} & a_{1n} & \cdots & a_{1(n-t+1)} \\ a_{1t} & \cdots & a_{11} & a_{11} & a_{12} & a_{1n} & a_{1n} & a_{1n} & \cdots & a_{1(n-t+1)} \\ a_{2t} & \cdots & a_{21} & a_{21} & a_{22} & a_{2n} & a_{2n} & a_{2n} & \cdots & a_{2(n-t+1)} \\ a_{3t} & \cdots & a_{31} & a_{31} & a_{32} & a_{3n} & a_{2n} & a_{2n} & \cdots & a_{3(n-t+1)} \\ \vdots & \ddots & \vdots & \vdots & \vdots & \ddots & \vdots & \vdots & \ddots & \vdots \\ a_{mt} & \cdots & a_{m1} & a_{m1} & a_{m2} & a_{mn} & a_{mn} & a_{mn} & \cdots & a_{m(n-t+1)} \\ a_{mt} & \cdots & a_{m1} & a_{m1} & a_{m2} & a_{mn} & a_{mn} & a_{mn} & \cdots & a_{m(n-t+1)} \\ \vdots & \ddots & \vdots & \vdots & \vdots & \vdots & \vdots & \vdots & \vdots & \vdots \\ a_{(m-t+1)t} & \cdots & a_{(m-t+1)1} & a_{(m-t+1)1} & a_{(m-t+1)2} & \cdots & a_{(m-t+1)n} & a_{(m-t+1)n} & \cdots & a_{(m-t+1)(n-t+1)} \end{bmatrix}$$

Definition 3.1.5 Let $A \coloneqq [aij]\ m{\times}n$ and $k \in \{1,2, \dots, t\}$. Then, k-approximate matrix of aij in $\bar{\bar{A}}t$ is denoted by $A_{ij}{}^{k}$ and is as follows:

$$\begin{bmatrix} \bar{\bar{a}}_{(i+t-k)(j+t-k)} & \cdots & \bar{\bar{a}}_{(i+t-k)(j+t+k)} \\ \vdots & \ddots & \vdots \\ \bar{\bar{a}}_{(i+t+k)(j+t-k)} & \cdots & \bar{\bar{a}}_{(i+t+k)(j+t+k)} \end{bmatrix}$$

Definition 3.1.6 The matrix $\hat{A}ij\ k \coloneqq [\hat{a}1\ ]$ consisting of all regular entries of $A_{ij}{}^{k}$ and non-decreasing is called regular row matrix or regular entry matrix (REM) of $A_{ij}{}^{k}$.

Definition 3.1.7 Let $\hat{A}ij\ k \coloneqq [\hat{a}1v\ ]1{\times}w$ be the REM of $A_{ij}{}^{k}$. Then, Cesáro mean of $A_{ij}{}^{k}$ is defined as follows $C(\hat{A}_{ij}{}^{k}) \coloneqq \frac{1}{\omega}\sum_{v=1}^{w} \hat{a}1v$

Definition 3.1.8 A matrix with all its entries being zero is called zero matrix and is denoted [0]. Secondly, we give the algorithm of ACmF and its flowchart in Figure 1 as follows:

ACmF's Algorithm Steps

Step 1. Read a NIM $A \coloneqq [aij]{\times}n$ such that $\min\{m, n\} \geq 5$

Step 2. Convert A from uint8 form to double form

Step 3. For t from 5 to 1

Obtain the binary matrix $B \coloneqq [bij]{\times}n$ of A

Obtain $\bar{\bar{A}}t$ and $\bar{\bar{B}}_{t}$

For all i and j

If $bij = 0$

For k from 1 to t

If $Bij\ k \neq [0]$

Obtain A_{ij}^{k}

Obtain $\hat{A}_{ij}^{k}$

$aij \leftarrow Cm(\hat{A}_{ij}{}^{k})$

Break

End If

End For

End If

End For

End For

3.2 The Used Image Processing Functions for Matlab and The Flowchart of AMF

The Used Image Processing Functions for Matlab and the Flowchart of AMF

1-Read and display file Function [X، map] play a role in the file، it can be called in the following format: [X، map] =imread (filename، fmt) ， the filename for read the image file name. fmt as the image format. I show function is to display the file, its syntax is as follows: show (BW) show(X, map) **[6]**.

2- Calculate two-dimensional convolution Function conv2 format: C = conv2 (A, B) is considered the role of the convolution matrix A and B.

3- Matlab implementation of the noise Function imnoise format: J=imnoise(I, type) J = imnoise (I, type, parameter) Returns the image I added the typical noise of the noisy image after the J, parameter type and parameter used to determine the type of noise and the corresponding parameters**[6]**.

3.3 Flowchart of ACmF :

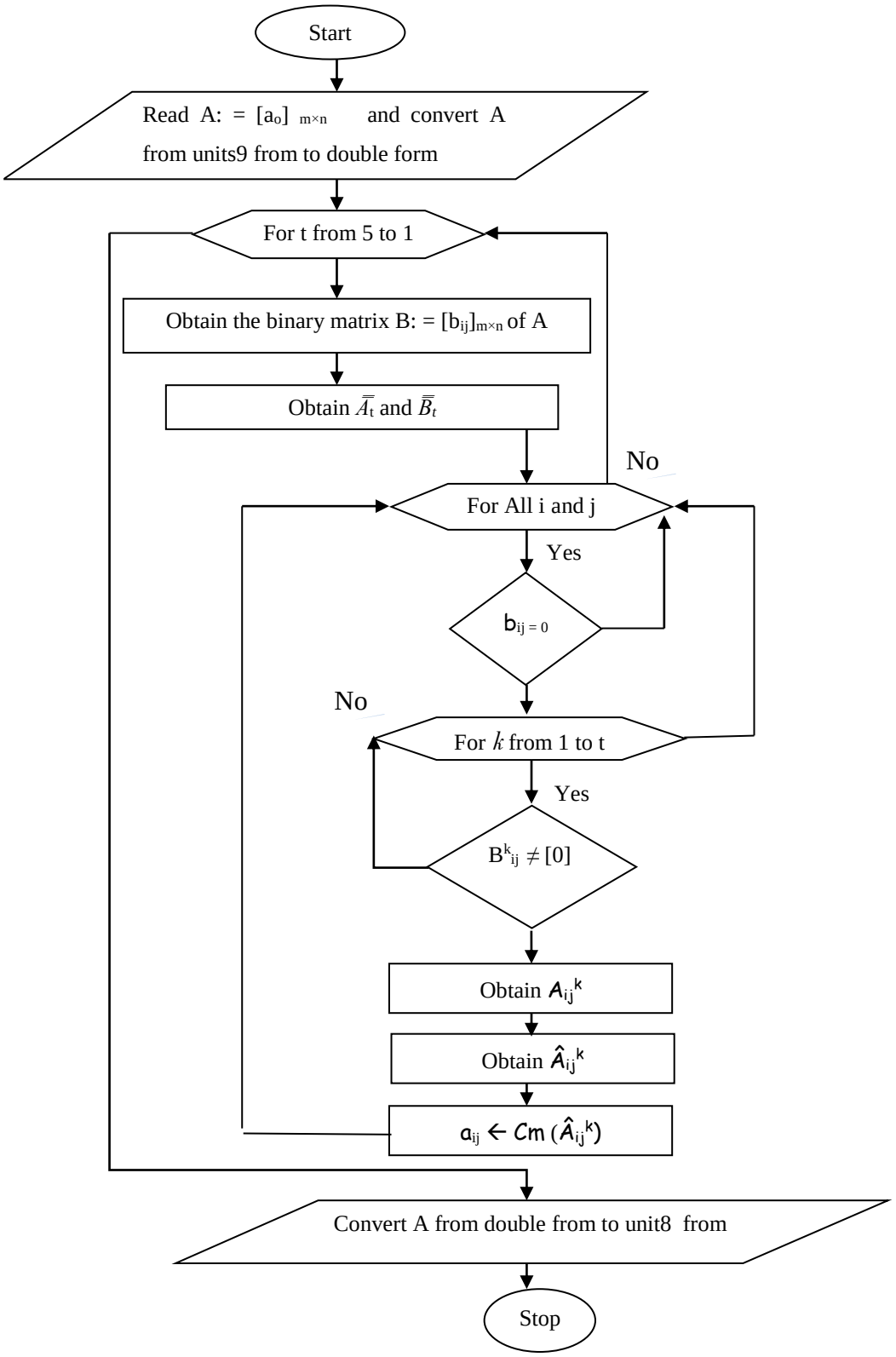

Chapter Four

Discussions and Results

Chapter Four
Discussions and Results

4.1 DISCUSSION

We proposed AmF, an efficient filter for SPN removal, and showed that AmF performs better than the known methods for all noise densities. AmF uses the mean of regular pixels as opposed to DAMF using the median. Moreover, AmF is recursive and, if needed, allows for the use of a bigger window size than those in DAMF. We compared AmF with the stateof-art methods whose algorithms were accessible. We in this project did not consider the filters whose algorithms were not accessible either on private or on global platforms, such as MathWorks. Further, AmF can be developed by exploiting a weighted mean or by employing a noise detection mask , AmF produces the best results in any noise density, it can be clearly observed that AmF outperforms the others. On the other hand, determining the ranking order of the other filters is not easy. Therefore, obtaining their ranking order is another crucial topic. We discuss Adaptive Mean Filter (AmF), a novel filter. AmF is recursive and uses the mean instead of the standard median to assign a new value to the centre pixel of a window. Furthermore, if need be, it allows for the use of a bigger window size than those in DAMF. In other words, AmF's basic differences from DAMF are its recursive nature, its reliance on the mean, and the use of window sizes up to 11 × 11. DAMF based on the standard median uses window sizes up to 7*7. AmF produces new values closer to the original pixel values. However, although AmF performs better than the state-of-art methods in terms of running time, it works a little slower due to the recursive procedure than DAMF does

4.2 Simulation Results :

In this section, we first present the quality metrics PSNR, SSIM, and MSSIM used to compare DBA, MDBUTMF, BPDF, NAFSMF, DAMF, AWMF, and ACmF. PSNR is defined as

$PSN(E, F) \coloneqq 10\log\left(\frac{255^2}{MSE(E,F)}\right)$

where MSE stands for the Mean Square Error and is defined as

$MSE(E, F) \coloneqq \frac{1}{mn}\sum_{i=1}^{m}\sum_{j=1}^{n}(e_{ij-f_{ij}})^2$

Here, $E \coloneqq [eij]$ is the earliest form/original image and $F \coloneqq [fij]$ is the final form/restored image. SSIM [17] is defined as

$SSIM(x, y) \coloneqq \frac{(2\mu_x\mu_y + C_1) + (2\sigma_{xy} + C_2)}{(\mu_x^2 + \mu_y^2 + C_1) + (\sigma_x^2 + \sigma_y^2 + C_2)}$

where μ_x, μ_y, σ_x, σ_y, and σ_{xy} are the average intensities, standard deviations, and cross-covariance for images x and y, respectively. Also, $C_1 \coloneqq (K1L)^2$ and $C_2 \coloneqq (K2L)^2$ are two constants such that K_1 = 0.01, K_2 = 0.03 and L = 255 for 8-bit grayscale images

MSSIM is defined as, for $x_1, x_2, \dots, x_n$ and $y_1, y_2, \dots, y_n$ images,

$MSSIM \coloneqq \frac{1}{n}\sum_{k=1}^{n} SSIM(\ x_{k,,}\ y_k)$

4.3 The Results Of Experiment :

4.3.1 PSNR and SSIM Results For Lena Image :

In Table 1. PSNR results for Lena image with different SPN ratios (10%-90%) and we compare AMF with the rest of filters in terms of PSNR with different Noise Densities .

Filters	10%	20%	30%	40%	50%	60%	70%	80%	90%
DBA	38.03	33.43	30.11	26.95	24.24	21.95	19.43	16.33	13.55
MDBUTMF	36.04	30.50	31.18	30.33	28.06	22.67	15.49	9.95	6.77
BPDF	39.88	35.82	32.86	30.51	28.37	25.89	23.01	18.01	10.84
NAFSMF	38.79	35.51	33.78	32.26	31.12	29.80	28.62	27.15	23.72
DAMF	43.12	39.07	36.66	34.90	33.24	31.77	30.18	28.56	25.88
AWMF	39.01	37.36	36.15	34.83	33.59	32.16	30.53	28.79	26.13
AmF	42.742	39.439	37.052	35.525	33.854	32.200	30.5526	28.858	26.110

(Table 1)

4.3.1 .1 SSIM Results For Lena Image :

In Table 2. SSIM results for Lena image with different SPN ratios (10%-90%) and we compare AMF with the rest of filters in terms of SSIM with different Noise Densities

Filters	10%	20%	30%	40%	50%	60%	70%	80%	90%
DBA	0.9761	0.9422	0.8963	0.8326	0.7528	0.6635	0.5656	0.4454	0.3587
MDBUTMF	0.9537	0.8154	0.8741	0.8840	0.8386	0.6830	0.3328	0.0866	0.0169
BPDF	0.9847	0.9656	0.9423	0.9105	0.8690	0.8117	0.7235	0.5391	0.2823
NAFSMF	0.9839	0.9665	0.9493	0.9293	0.9081	0.8813	0.8509	0.8038	0.6883
DAMF	0.9904	0.9787	0.9656	0.9497	0.9312	0.9081	0.8786	0.8384	0.7670
AWMF	0.9820	0.9737	0.9637	0.9504	0.9346	0.9129	0.8839	0.8433	0.7729
AmF	0.9903	0.9801	0.9675	0.9539	0.9367	0.9133	0.8833	0.8421	0.7671

(Table 2)

In this project , we proposed AmF, an efficient filter for SPN removal, and showed that AmF performs better than the known methods for all noise densities. AmF uses the mean of regular pixels as opposed to DAMF using the median. Moreover, AmF is recursive and, if needed, allows for the use of a bigger window size than those in DAMF. The results by The Peak Signal to Noise Ratio in (Table 1) and Structural Similarity in (Table 2) show that AmF performs better than the other filters.

4.3.1.2 Lena Image With Different SPN Ratios :

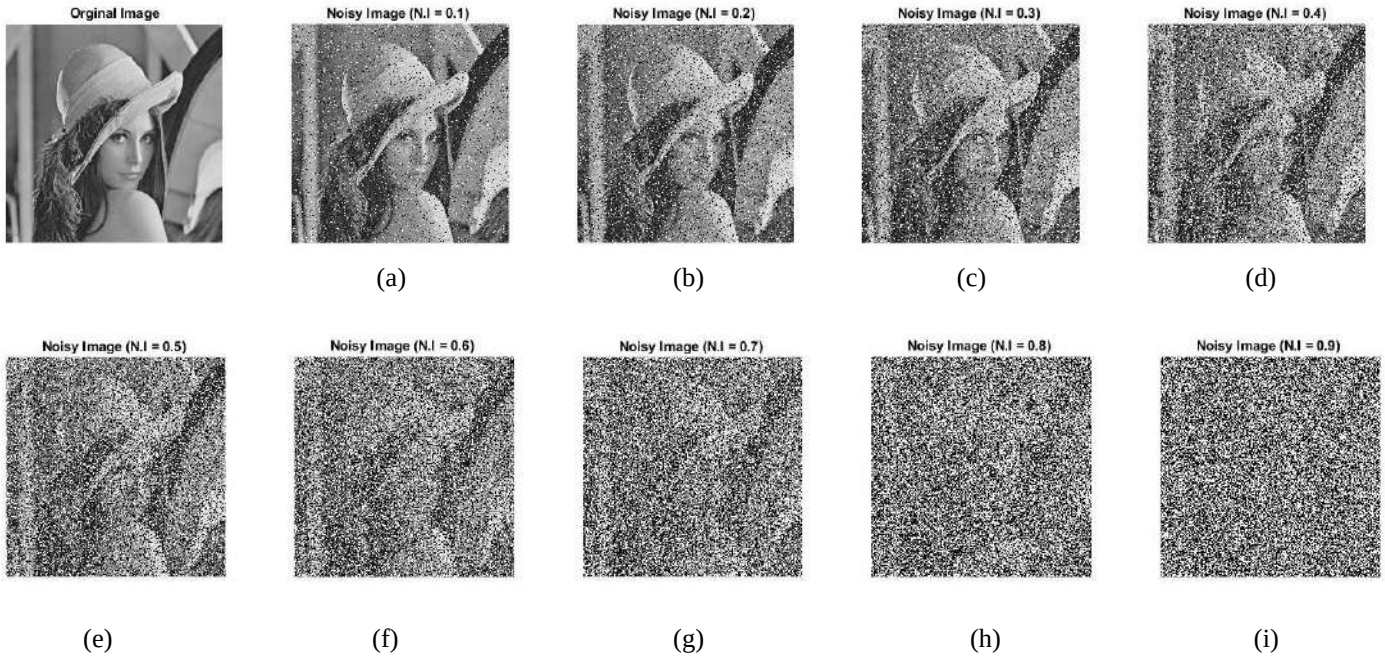

Figure 1. "Lena Image " of size 512 × 512 with different SPN ratios. (a) 10% ,(b) 20% , (c) 30% , (d) 40% , (e) 50% , (f) 60% , (g) 70% , (h) 80% , (i) 90% .

4.3.1.3 Lena Image With Different SPN Ratios Filtered By AMF :

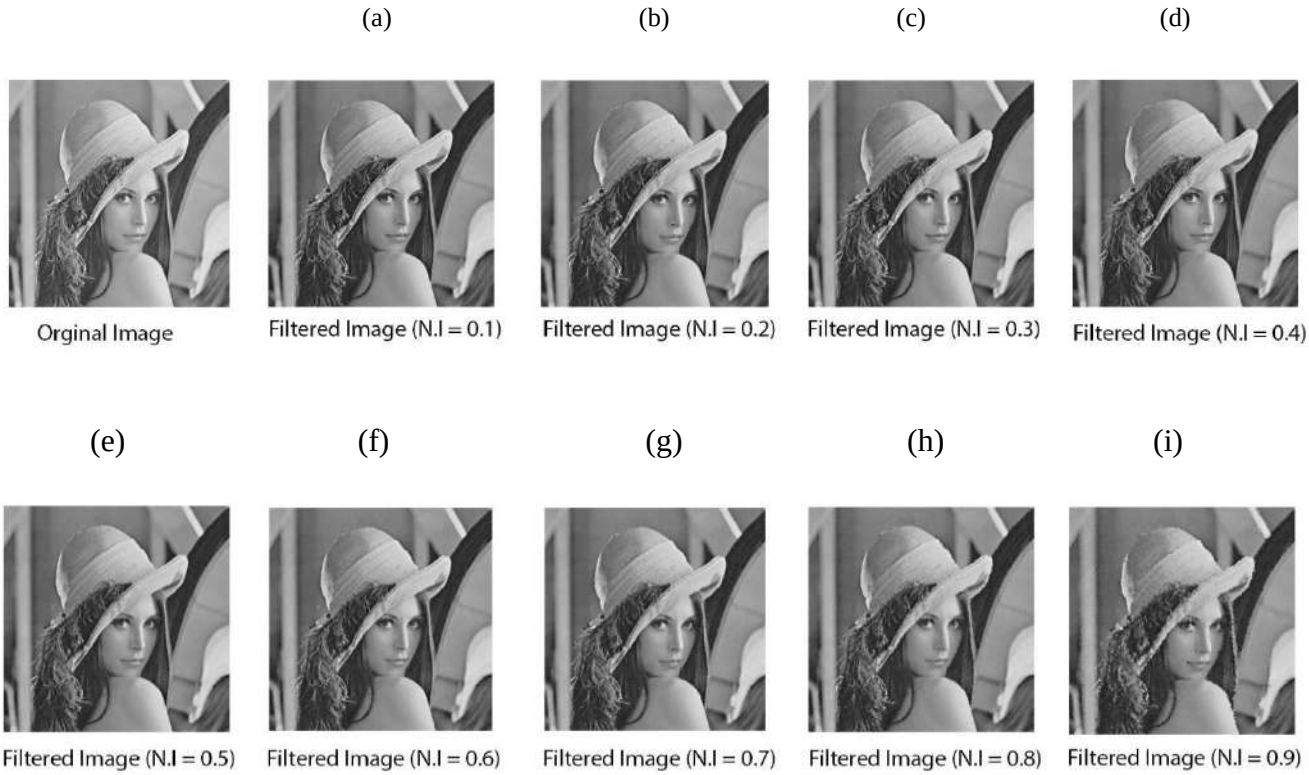

Figure 2. PSNR and SSIM results of AmF for "Lena" of size 512 × 512 with different SPN ratios. (a) 10% (42.742, 0.9903) ,(b) 20% (39.439, 0.9801) ,(c) 30% (37.0522, 0.9675) ,(d) 40% (35.525, 0.9539) ,(e) 50% (33.854, 0.9367) ,(f) 60% (32.2001,0.9133) ,(g) 70% (30.5526,0.8833) ,(h) 80% (28.858,0.8421), (i) 90% (26.11,0.7671) .

4.3.2 Testing AMF On Brain Image from MRI :

We Show PSNR and SSIM results of AMF for "Brain Image from MRI" of size 512 × 512 with a noise density range from 10% to 90%.

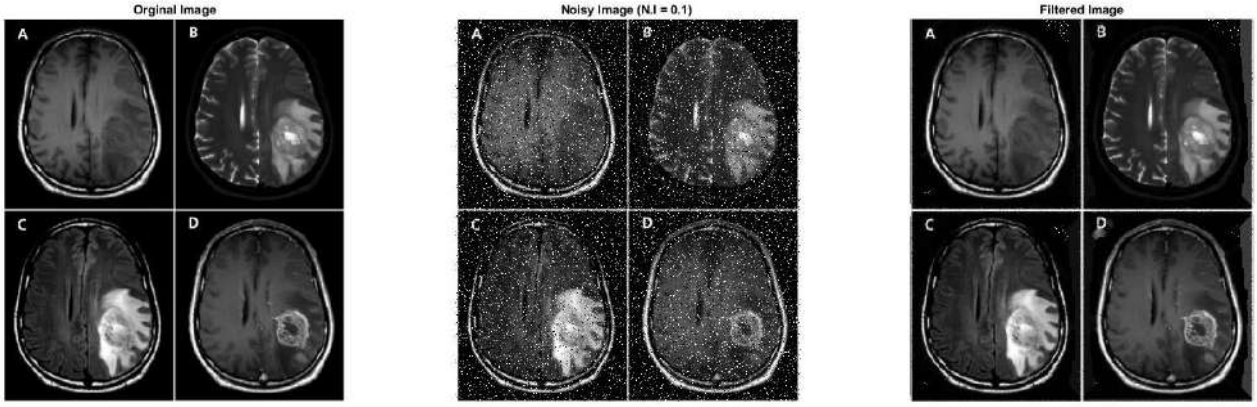

Figure 3. PSNR and SSIM results of AmF for "Brain Image " of size 512 × 512 with 10% SPN ratio (PSNR = 21.9986 , SSIM = 0.8058).

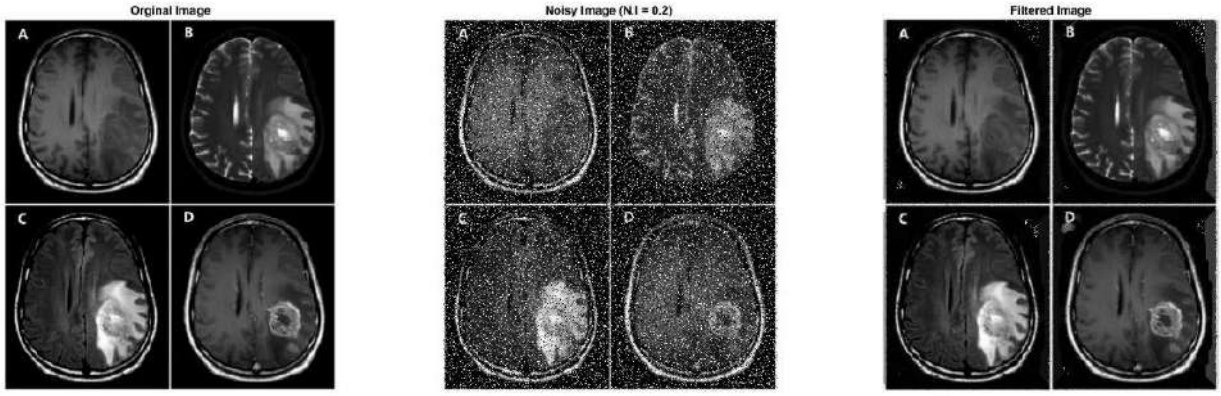

Figure 4. PSNR and SSIM results of AmF for "Brain Image " of size 512 × 512 with 20% SPN ratio (PSNR = 19.1841, SSIM = 0.7921).

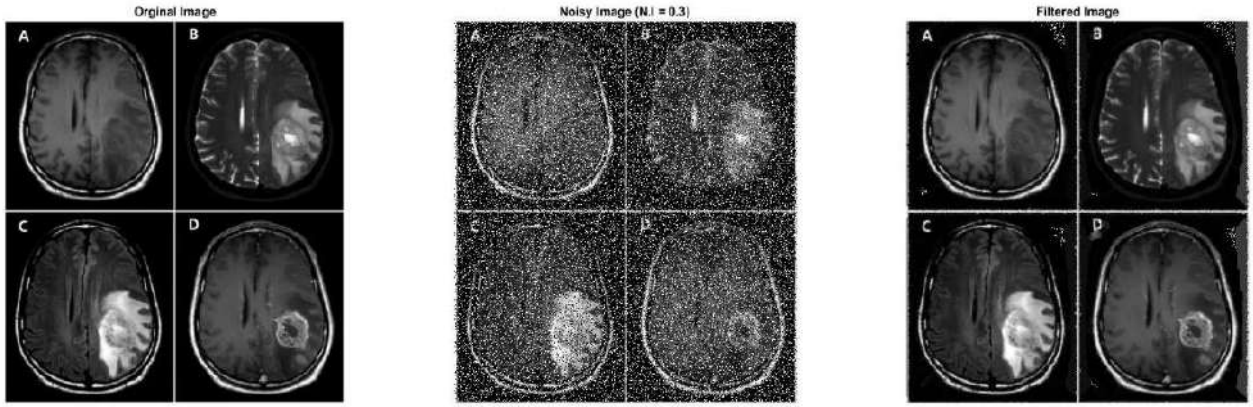

Figure 5. PSNR and SSIM results of AmF for "Brain Image " of size 512 × 512 with 30% SPN ratio (PSNR = 17.3658, SSIM = 0.7855).

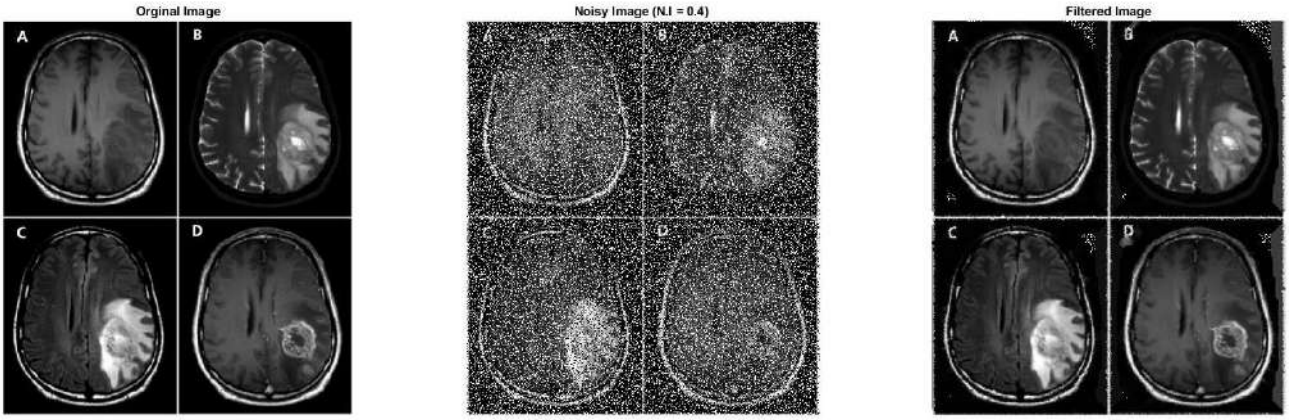

Figure 6. PSNR and SSIM results of AmF for "Brain Image " of size 512 × 512 with 40% SPN ratio (PSNR = 16.0888, SSIM = 0.7791).

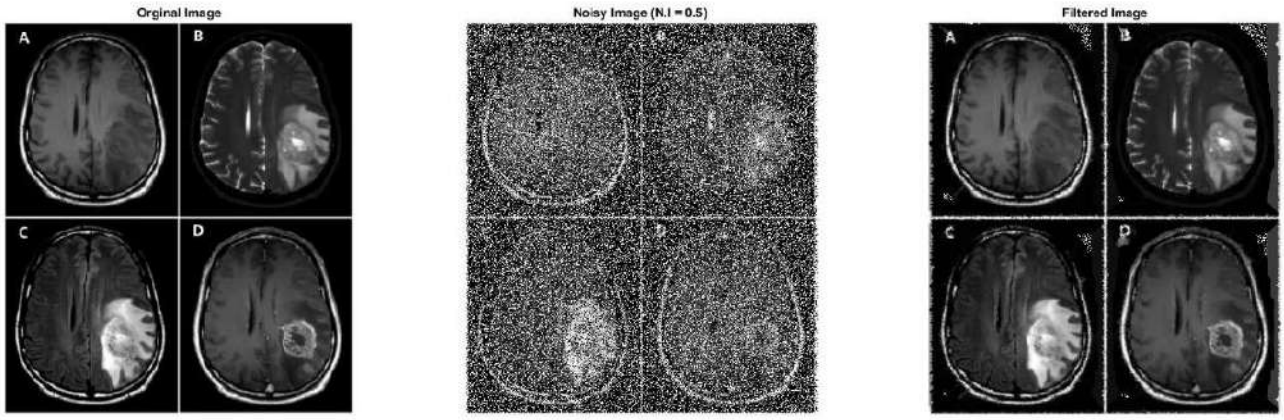

Figure 7. PSNR and SSIM results of AmF for "Brain Image " of size 512 × 512 with 50% SPN ratio (PSNR = 15.0763, SSIM = 0.7712).

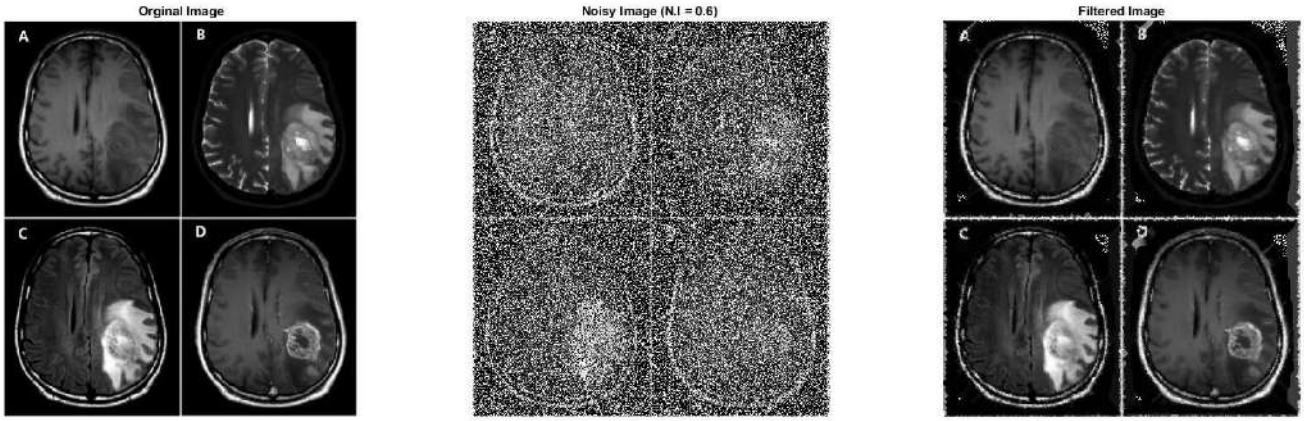

Figure 8. PSNR and SSIM results of AmF for "Brain Image " of size 512 × 512 with 60% SPN ratio (PSNR = 14.2489, SSIM = 0.7603).

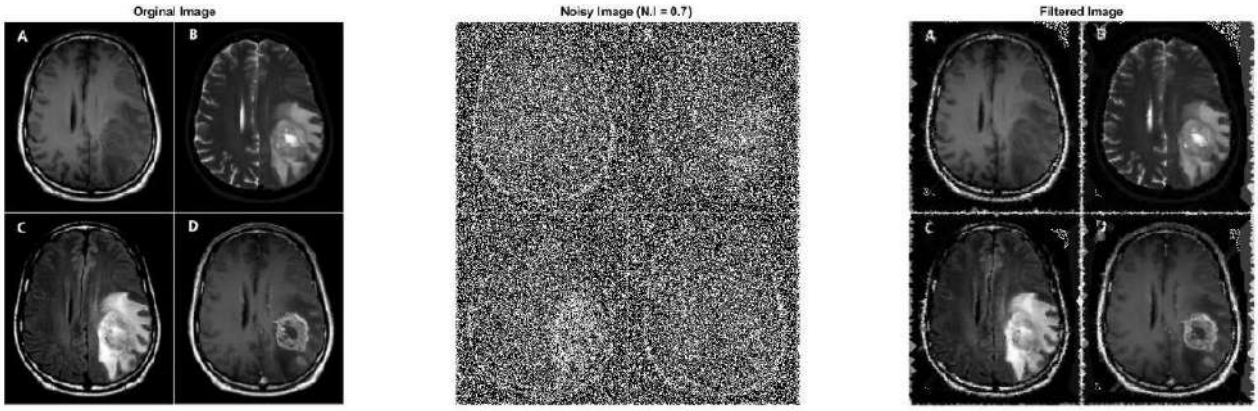

Figure 9. PSNR and SSIM results of AmF for "Brain Image " of size 512 × 512 with 70% SPN ratio (PSNR = 13.5331, SSIM = 0.7447).

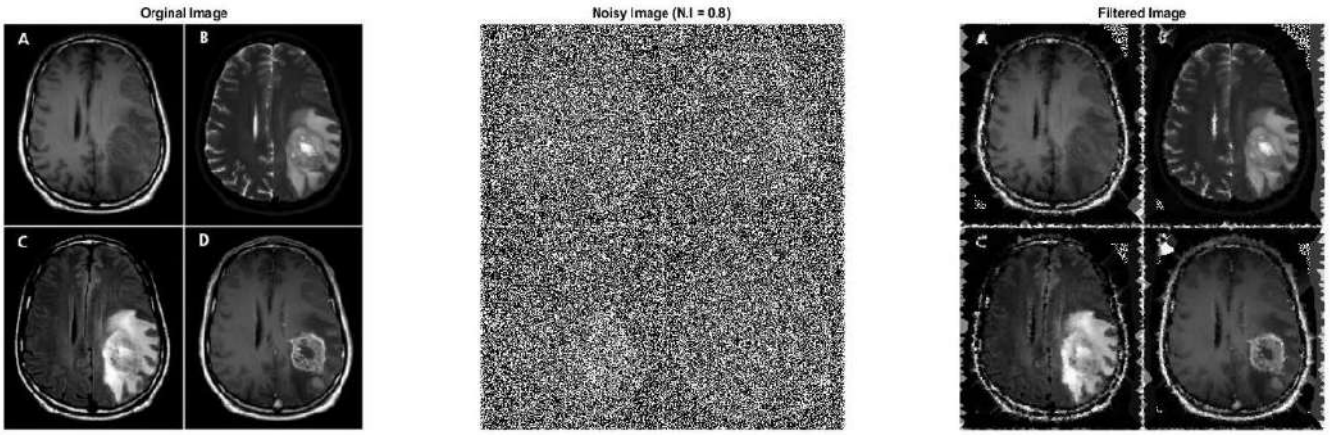

Figure 10. PSNR and SSIM results of AmF for "Brain Image " of size 512 × 512 with 80% SPN ratio (PSNR = 12.7916, SSIM = 0.7153).

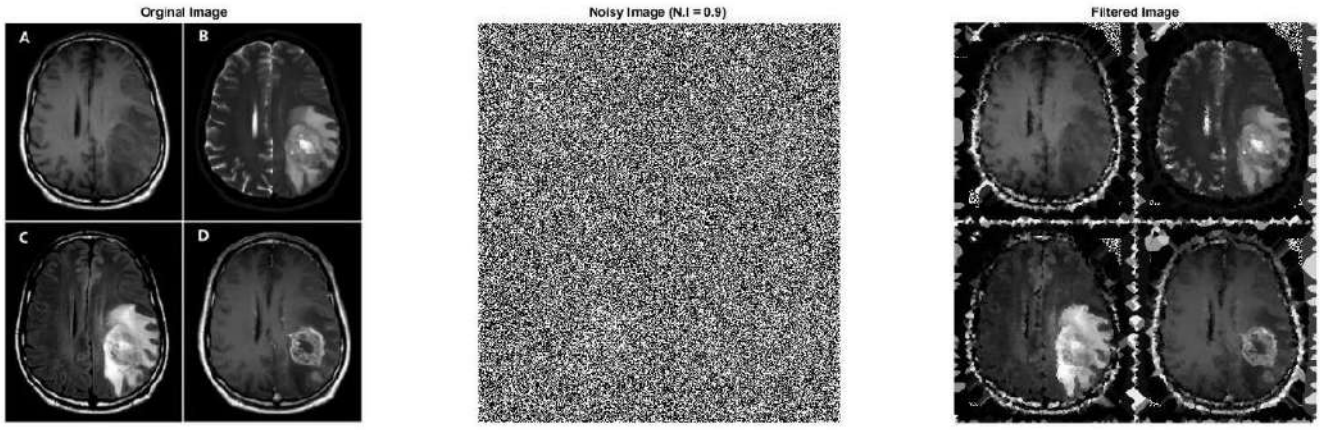

Figure 11. PSNR and SSIM results of AmF for "Brain Image " of size 512 × 512 with 90% SPN ratio (PSNR = 11.9604, SSIM = 0.6548).

In Table 3 with the chart (Figure a) .Peak Signal to Noise Ratio (PSNR) and Structural Similarity (SSIM) results of AmF for "Brain Image From MRI" of size 512 × 512 with different SPN ratios (10%-90%)

Noise Ratios	PSNR results	SSIM results
10%	21.9986	0.8058
20%	19.1841	0.7921
30%	17.3658	0.7855
40%	16.0888	0.7791
50%	15.0763	0.7712
60%	14.2489	0.7603
70%	13.5331	0.7447
80%	12.7916	0.7153
90%	11.9604	0.6548

(Table 3)

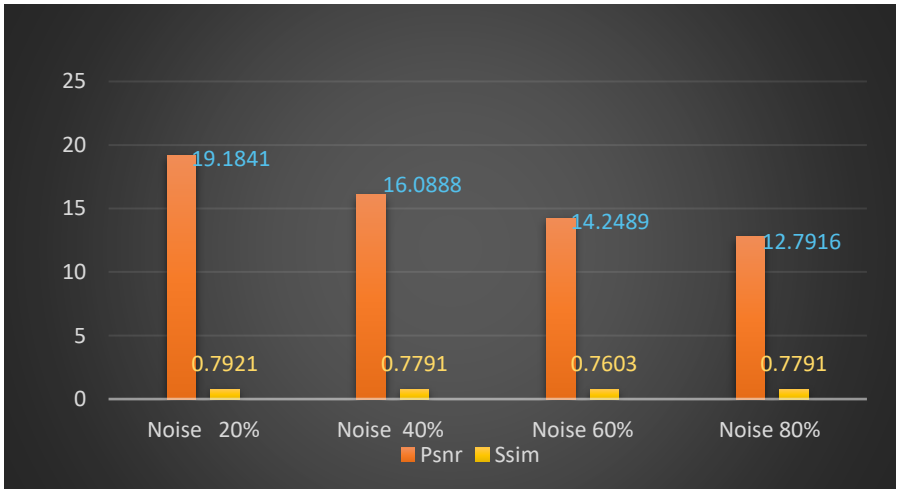

(Figure a)

Chapter Five
Conclusion and Recommendations

Chapter Five
Conclusion and Recommendations for Future Work

5.1 Conclusion

In this project , we have explored various digital filters for removing salt and pepper noise from images , and showed that AmF performs better than the known methods for all noise densities. AmF uses the mean of regular pixels as opposed to DAMF using the median, then we applied AmF to several test images whose noise densities range from (10% to 90%) 2 traditional test images (lena image, brain image From The MRI) Our experimental results have shown that the AMF is the most effective filter for removing salt and pepper noise from images. We have also compared the performance of these filters using various metrics such as peak signal-to-noise ratio (PSNR) and mean square error (SSIM).

5.2 Future works

1. Although our study has shown that the AMF filter is the most effective filter for removing salt and pepper noise from images there is still room for improvement In the future we can explore other digital filters such as the bilateral filter and wavelet based filters to improve the performance of salt and pepper noise removal Additionally
2. we can also investigate the use of deep learning techniques for salt and pepper noise removal .
3. This can involve training a neural network to remove salt and pepper noise from images which can potentially lead to better results compared to traditional digital filters.
4. Finally, we can also explore the impact of salt, pepper noise removal on other image processing tasks such as image segmentation, and object.

REFERENCES

[1] Kaur, A., & Kaur, P. (2017). A review of salt and pepper noise removal techniques. International Journal of Computer Science and Mobile Computing, 6(3), 1-10.

[2] Zhang, X., Liu, J., & Zhang, D. (2018). A novel adaptive median filter for salt-and-pepper noise removal in images. Journal of Visual Communication and Image Representation, 54, 1-9.

[3] Li, C., & Guo, Y. (2019). A fast and efficient algorithm for salt and pepper noise reduction in digital images. Journal of Ambient Intelligence and Humanized Computin10(7),2665-2674.

[4] Chen, Y., & Liu, X. (2019). Salt and pepper noise removal based on improved median filter. Journal of Physics: Conference Series, 1194(1), 012085.

[5] Li, Y., & Zhu, X. (2020). A novel salt and pepper noise removal algorithm based on fuzzy logic and morphological filtering. Multimedia Tools and Applications, 79(19), 13335-13349.

[6] Wang, H., & Chen, H. (2020). An adaptive median filter using a new threshold function for salt and pepper noise removal. Journal of Electronic Imaging,29(2),023022.

[7] Zhang, H., & Zhang, Y. (2020). A novel salt and pepper noise removal algorithm based on image decomposition and non-local means filtering. Journal of Ambient Intelligence and Humanized Computing, 11(1), 591-600.

[8] Liu, J., Zhang, X., & Zhang, D. (2020). A novel adaptive median filter for salt-and-pepper noise removal in color images. Journal of Visual Communication and Image Representation,70, 102786.

[9] Singh, H., & Bhatia, S. (2020). A comparative study of salt and pepper noise removal techniques for digital images. International Journal of Computer Applications, 179(45), 1-8.

[10]Chen, X., & Li, J. (2021). Salt and pepper noise removal based on improved fuzzy filter. Journal of Physics: Conference Series, 1786(1), 012026.

[11] Xie, Y., Li, J., & Guo, Y. (2021). A novel salt and pepper noise removal algorithm based on improved weighted median filter. Multimedia Tools and Applications, 80(20), 30829-30846.

[12] Zhang, J., Wang, Z., & Li, Y. (2021). A novel salt and pepper noise removal algorithm based on improved pixel value replacement. Journal of Ambient Intelligence and Humanized Computing, 12(5), 4859-4870.

[13] Li, J., Xie, Y., & Guo, Y. (2021). A novel salt and pepper noise removal algorithm based on improved adaptive median filter. Journal of Ambient Intelligence and Humanized Computing, 12(6), 6453-6465.

[14] Kumar, A., & Kumar, D. (2021). A review on salt and pepper noise removal techniques in digital images. Journal of Ambient Intelligence and Humanized Computing, 12(6), 6477-6490.

[15] Wang, X., Chen, M., & Liu, X. (2021). Salt and pepper noise removal based on improved decision-based algorithm. Journal of Physics: Conference Series, 1936(1), 012135.

[16] Li, J., Xie, Y., & Guo, Y. (2021). A novel salt and pepper noise removal algorithm based on improved fuzzy filter. Journal of Ambient Intelligence and Humanized Computing, 12(7), 8275-8287.

[17] Zhang, J., Wang, Z., & Li, Y. (2021). A novel salt and pepper noise removal algorithm based on improved pixel value replacement. Journal of Ambient Intelligence and Humanized Computing, 12(5), 4859-4870.

Appendix :

sample of code :

```
;io=imread("lena.tif")


Noise_Image = imnoise(io,'salt & pepper',0.8)

;imshow(Noise_Image)

Denoised_Image = ACmF(Noise_Image)

;imshow(Denoised_Image)



psnr_results = psnr(io,Denoised_Image)

ssim_results = ssim(io,Denoised_Image)


subplot(131);imshow(io)

title('Orgina Image')

subplot(132);imshow(Noise_Image)

title('Noisy Image')

subplot(133);imshow(Denoised_Image)

title('Denoised Image')
```

ACmF

```
function X=ACmF(A)
;A=double(A)
for p=5:-1:1
;pA=padarray(A,[p p],'symmetric')
;pB=(pA~=0 & pA~=255)
;[m,n]=size(pB)
for i=1+p:m-p
for j=1+p:n-p
if (pB(i,j)==0)
for k=1:p
if (isequal(pB(i-k:i+k,j-k:j+k),zeros(2*k+1,2*k+1))~=1)
;R1=pA(i-k:i+k,j-k:j+k)
;R2=R1(R1>0 & R1<255)
;A(i-p,j-p)=mean(R2)
;break
end
end
end
end
end
```

```
end
;X=uint8(A)
end
```

الملخص

في هذا المشروع ، اقترحنا طريقة إزالة ضوضاء الملح والفلفل (SPN) ، مرشح متوسط التكيف (AmF) ، وقدمنا بعض مفاهيمه الأساسية. نقوم بعد ذلك بتطبيق AmF على العديد من صور الاختبار التي تتراوح كثافة الضوضاء فيها من 10٪ إلى 90٪: 6 صور اختبار تقليدية (صورة لينا ، صورة دماغية ، أشعة سينية لمعالجة صورة العظم الخلفي) وصور اختبار أخرى ، متوفرة في قاعدة بيانات الاختبارات. بعد ذلك ، قارنا AmF مع أحدث الأساليب ، قارنا مرشح AMF مع بقية المرشحات من حيث PSNR و ssim بكثافات ضوضاء مختلفة. تظهر نتائج نسبة الإشارة القصوى إلى الضوضاء (PSNR)والتشابه الهيكلي (SSIM) أن أداء AmF أفضل من الطرق المذكورة أعلاه. علاوة على ذلك ، نقوم أيضًا بمقارنة بيانات وقت التشغيل لهذه الخوارزميات. تظهر هذه النتائج أن AmF يتفوق على الطرق باستثناء .DAMF نناقش أخيرًا الحاجة إلى مزيد من البحث. الكلمات المفتاحية: ضجيج الملح والفلفل ، إزالة الضوضاء ، تقليل ضوضاء الصورة ، المتوسط التكيفي .

شكر واهداء

أشكر الله تعالى على فضله حيث أتاح لي إنجاز هذا العمل بفضله، فله الحمد اولا واخرا.

نتقدم بجزيل الشكر والتقدير الى الأستاذ المشرف "انس فؤاد احمد" على كل ما قدمه لنا من توجيهات ومعلومات كما نقدم جزيل الشكر الى أعضاء لجنه المناقشة الموقرة.

وأيضا أتقدم بالشكر إلى أبي وأمي، إلى من يجري حبهما في عروق دمي، كلمات الحب عجزت عن وصف حبّي الكبير لعظمتكم، فحروف العشق عجزت عن نظم أجمل القصائد واللحان فيكم.

وزارة التعليم العالي والبحث العلمي
الجامعة العراقية
كلية الهندسة
قسم الهندسة الكهربائية

تنفيذ مرشح متوسط التكيف لإزالة ضوضاء الملح والفلفل

من قبل :
علي سعيد هادي
علي سمير فاضل
علي عبد الأمير حيدر

بأشراف :
الأستاذ المساعد أنس فؤاد احمد

Ministry of Higher Education and Scientific research
Al-Iraqia University
Engineering College
Electrical Engineering Department

ELECTRICAL SPRING MODELLIND BASED ON GENERATING SYSTEM ADEQUACY

A Project Submitted to the Department of Electrical Engineering in Partial Fulfilment for the Requirements of the Degree of B.Sc. in Electrical Engineering

BY

ALI MUHAMMAD NASRALLAH
ABDULRAHMAN MAUTH MOHAMMED
OTHMAN JALAL JASIM
MUTAZ MASHAN ENAD

SUPERVISOR

DR. HUSSEIN GUMAA JABER

2022-2023

DECLARATION

We hereby declare that this project report is based on our original work except for citations and quotations, which have been duly acknowledged.

Signature : _____

Name : _____

Date : _____

Signature : _____

Name : _____

Date : _____

Signature : _____

Name : _____

Date : _____

Signature : _____

Name : _____

Date : _____

APPROVAL FOR SUBMISSION

I certify that this project report entitled **"ELECTRICAL SPRING MODELLIND BASED ON GENERATING SYSTEM ADEQUACY"** was prepared by (**ALI MUHAMMAD NASRALLAH, ABDULRAHMAN MAUTH MOHAMMED ,OTHMAN JALAL JASIM,MUTAZ MASHAN ENAD)** has met the required standard for submission in partial fulfilment of the requirements for the award of Bachelor of **Electrical Engineering at Al-Iraqia University .**

Approved by,

Signature : _____

Supervisor : _____

Date : _____

ACKNOWLEDGEMENTS

In the name of Allah, the most gracious, the most merciful. First, I would like to thank and praise almighty Allah from the depths of my heart, for giving me the opportunity to pursue Bachelor degree study in Al-Iraqia University and providing me with the ability and patience upon facing difficulties during all this time. We offer my sincerest gratitude to my supervisor, Dr. Hussein Jumma, who has guided and supported us with his patience and knowledge throughout our research. We attribute our accomplishment to his encouragement, patience and effort, without him this project would not have been completed. One simply could not wish for a better and friendlier supervisor as he is. His suggestions and advices had helped us in our times of despair when our research was facing some problems. We would like to extend our gratitude to our family members who always support us and pray for us to complete our project. Our appreciation also goes to the Electrical Engineering department, for giving us the opportunity to further our studies.

ABSTRACT

Electrical power systems have to be aware of the major challenges that still lie ahead, for example, the massive penetration of electrical vehicle and load and supply-side uncertainties. Since, the adequacy of power supply assessment is an important process in power systems planning phase, PV technology is one of the most efficient and applicable solution to be considered. If the generation unit's capacity is insufficient to meet the system load, then assistance is required from alternative sources. A PV is widely implemented in electrical power generation due to its considerable impact on system reliability and efficiency. Generating capacity adequacy assessment is usually performed by using two-state model in which all generation units transit only between up and down states regardless of the types of generators. The findings from this project show that the proposed PV and Electric spring models can perform better than Original case without this model and is, therefore, a more robust strategy to be implemented. In addition, the findings show that this model leads to more accurate and realistic assessment of adequacy of supply .The sequential Monte Carlo simulation (MCS) was employed in this project. The study was conducted using the IEEE-reliability test system (RTS).

Chapter One

Introduction

1.1 Background

Modern electrical power systems must meet constantly changing power consumption requirements with a satisfactory level of reliability, environmental friendliness and quality (Billinton, 2013). Nevertheless, meeting these challenges has become progressively difficult owing to the increase in electricity demands caused by population and industrial growth (Dehnavi and Abdi, 2017). Thus, electrical power grids must be highly integrated to cope with the uncertainty of load and supply. The International Energy Agency estimated that the global power energy demand in 2030 will be more than 50% higher than that in the present (Freeman, 2005), for example, due to the massive implementation of the electric vehicle (Martínez-Lao et al., 2017). In addition to this issue, the infrastructure investments required to support the growing global electricity demand will be massive because ageing power system components will have to be replaced.

Thus, the usual practices aimed at balancing electricity supply and demand have to be examined closely. Reduction of power consumption is worth more than power generated (Saini, 2004). For example, after accounting for transmission and distribution along line losses, one unit of electricity saved at the consumer side is worth 10% more of the unit saved at the generator side. Although system reliability can be

maintained by increasing investment into the system, the cost of investment must be justified by the value of reliability improvement. In this sense, the reliability and economic constraints are opposite (Billinton, 2013). Thus, finding an optimal managerial decision at the planning phases is beneficial for ensuring customer satisfaction at all times.

As a whole, PV and electric spring models investigated in this project fit into the wider agenda of generating integration of RES. Since RES, has received considerable attention in recent years due to their significant impacts on reliability, RES and electric spring programmes are expected to be implemented substantially in the next few decades to satisfy the requirements of new challenges, such as the intermittent nature of renewable energies, global environmental concerns and economic constraints. These programmes should be considered in the planning and operation phases of electrical power systems and must be integrated with generation-side management to maintain the reliability and increase the efficiency of power systems.

1.2 Power Systems Reliability

The electric utility industry is obligated to supply efficient and reliable electric services to customers as economically as possible (Li, 2013). However, it is unpractical to design and construct fully reliable electrical power systems. Power system planners attempt to design a reasonable level of reliability at an acceptable initial and running cost. The reliability of power systems is a measure of the overall ability of the system to achieve its basic function. System reliability is divided into two: system adequacy and system security as shown in Figure 1.1.

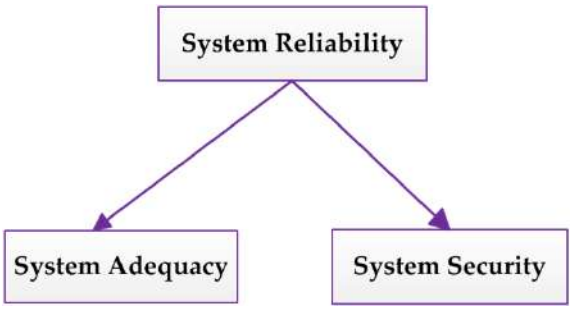

Figure 1.1 Division of system reliability (Billinton, 2013)

System adequacy refers to the existence of sufficient facilities to meet the consumer demand. These facilities involve the generators to generate sufficient energy, the associated transmission lines to transmit the required energy to the distribution systems and the distribution networks to transport the energy to customers. Therefore, system adequacy does not include system disturbances. Security relates to the ability of the system to respond to disturbances.

Electric power systems are generally categorized into three hierarchical levels (HLs) of generation, transmission and distribution as shown in Figure 1.2.

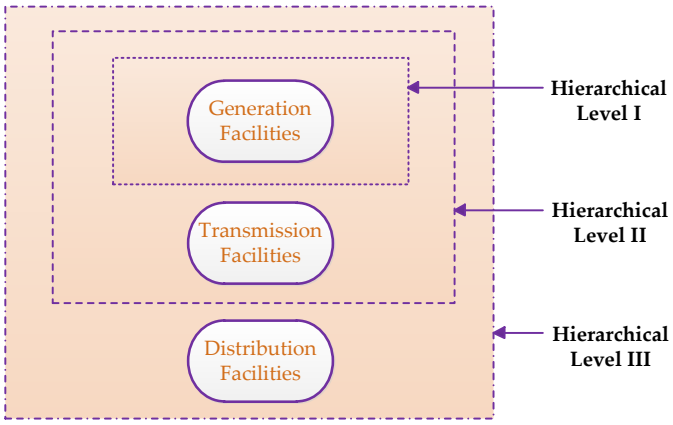

Figure 1.2 Hierarchical levels (Billinton, 2013)

HL1 involves the analysis of the generation facility, HL2 considers the analysis of the generation and transmission facilities and HL3 considers the analysis of an

additional distribution facility. Only HL1 and HL2 studies are regularly performed given that complete HL3 studies are highly complex because of their large problem scale. Thus, the distribution network is normally analysed individually and separately from the generation and transmission systems. Electrical power reliability is usually calculated in terms of certain reliability indices. These are usually measured to evaluate the level of reliability worth and cost at specific zone in electrical power systems, therefore, it is significant to tabulate these indices as in Appendix A (Billinton, 2013). HLI reliability assessment is defined as generating capacity adequacy evaluation. One of the power system reliability investigation studies is the generating systems adequacy study and it is concerned only with the ability to satisfy customer demand (Billinton, 2013). Generating systems adequacy is the ability of generation systems to provide a sufficient and continuous supply of electricity to the users' demands. The ability of transmission and distribution system to move the supplied energy to the end-user is neglected in HLI assessment. In this study, transmission and distribution systems are not considered and assumed fully reliable. Thus, this project focuses on the HLI assessment. Generating capacity adequacy assessment is usually performed by using two, three and four-state model. In two-state model, all generation units transit only between up and down states regardless of the types of generators. The three-state model takes the partial outage of the large thermal generation units into account. Four-state model is properly used to model peaking and cycling generation units. Expected values based on probabilistic assessment are used to assess the level of adequacy, namely loss of load expectation (LOLE), expected energy not-supplied (EENS), loss of load frequency (LOLF) and loss of load duration (LOLD).

1.3 **Problem Statement, Project Gap , Aim and Objectives**

Electric spring is an electric device that can be used to: i) provide electric voltage support; ii) store electric energy; and iii) damp electric oscillations. Thereby , reliability of supply will be improved. Solar energy is one of the most eco-friendly and cheapest source of energy. Solar power can contribute considerably to a sustainable electricity supply of world and to a reduction of CO2 emissions and to enhance reliability of supply if integrated with other techniques. The conventional generation systems (i.e. thermal and nuclear) have a high production cost and are unclean. photovoltaic (PV) systems are clean , silent, free maintenance , efficient and reliable source of energy. Renewable energies (RES) have a high uncertainty and are unpredictable source of energy. Electrical spring can be integrated with RES to overcome their uncertainty and thereby the reliability of generation side can be improved. The variability of renewable sources has high impact on power system. PV and electric spring (ES) are one of several options for better grid reliability. The Objectives are to model PV energy systems and electric spring in reliability framework by using Matlab and then to assess EENS for each case study. The main aim of this project is to decrease the pollution and production cost of electricity. This Project serves to establish power system reliability of hierarchical level 1 (HL1) using MCS technique. The IEEE Reliability Test System (IEEE-RTS) generation model and load model are applied to convolute a system risk model. The project contribution are :-

1. Incorporating PV improves system reliability but the variability of PV power output compromises on PV capacity credit. ES has been included into system risk model to enhance system reliability performance.

2. System adequacy index(EENS) is investigated to show the system reliability performance. Impact on system reliability of generation units , via variation of PV and ES capacities are presented.
3. Actual Iraqi PV irradiance data is incorporated in this study. This analytical technique can help Iraqis energy supplier to evaluate the potential of PV to benefit system reliability and find ways to improve its potentials.

1.4 Scope of project

The scope of the project concentrates exclusively on the generating capacity adequacy (or HLI) assessment incorporating with selected PV and electric models. Probabilistic approach is used by utilising sequential Monte Carlo simulation (MCS) to calculate reliability indices. The system risk model is acquired by combining the generation model with the load model. Thus, risk indices are obtained. Sequential MCS simulates the actual process and the random behaviour of the generation systems in HLI assessment. The reliability indices are obtained by combining the load model with the generation model and then to find power inadequacy in terms of energy amount per each interruption.

1.5 Project Structure

In accordance with the aforementioned objectives, the project is structured as fouyr chapters, which are summarised as follows: Chapter 1 gives a general overview of the background of the work. Chapter 2 presents. Chapter 3 introduces the methodology. Chapter 4 gives the result and the main conclusions of this project.

Chapter Two

LITERATURE REVIEW

2.1 Introduction

This chapter is an attempt to perform a different kind of analysis that addresses the gaps. A review of various initiatives, techniques, impacts and recent developments of the PV and electric spring of electrical power systems are presented.

Renewable energy sources (RES) are stochastic in nature, intermittent, unpredictable and uncontrollable. Despite this, they remain crucial sources for a sustainable future grid. Electric spring ES has been used aggressively as a method to mitigate the effects of RES intermittency by implementing various methods such as DLC and energy storage systems (ESS). However, they cannot be implemented in real-time like load scheduling (Soni and Panda, 2017). ES is considered as a valuable tool to mitigate the intermittency of RES (Moura and De Almeida, 2010). Whereas ES programmes are able to mitigate the negative impacts of wind energy intermittency towards the reliability of the electrical power systems (Moshari et al., 2016). Many studies have assessed the intermittency of renewable energy sources at the supply side either as bulk units or at the demand-side as medium units. A priority-based ES and ESS for solar photovoltaic systems have been proposed to mitigate the intermittency of power generation (Kandasamy et al., 2017). ES has been used to integrate the growing number of renewable energy sources in Portugal (Moura and De Almeida, 2010). A probabilistic programming for smart microgrids has been implemented by considering ES as compensation for the uncertainty caused by wind and solar power generation (Aghajani et al., 2017). The technical potential of active load management

in a distributed electrical power systems with a high penetration of RES was studied in (Zong et al., 2012). The impacts of adding wind power and DR on both greenhouse gas emissions and generator cycling requirements has been proposed to show the effectiveness of ES in mitigating the variability of renewable generation (Broeer et al., 2018). DSM has a significant rule in the integrated resource planning (Hu et al., 2013) and provides an applicable tool to incorporate utility and customer necessities into integrated planning procedures (Gellings and Smith, 1989). The impact of DSM has been addressed to enable the integration of growing volatility resources (Moura and De Almeida, 2010, Wimmler et al., 2017). Integration of DSM with distributed generation and ESS has been studied (Farmad and Biglar, 2012). The integration of DR into energy and reserve market optimization problem has been presented (Darvish et al., 2015). The integration of both DSM and supply-side management in generation expansion planning has been investigated (Karunanithi et al., 2017). The impact of integrating solar and wind energies incorporating DSM programmes on the reliability has been examined (Aiowaifeer et al., 2015).In Table , ES objectives and techniques, additive model, reliability indices and test systems are compared while in Table 1 , the contributions, benefits and limitations are compared.

Table 1 Summary of comparison on the DSM impact on HL1

Sources	DSM programme	Additive model	Reliability indices	Test system
(Ahsan, 1990)	DLC, PLS	ESS	LOLE	IEEE-RTS
(Teh, 2018)	DLC, PLS	ESS,RES	EENS	IEEE-RTS
(Joung and Kim, 2013)	RTP, PC	Smart metering	LOLE,EENS	IEEE-RTS
(Zhou et al., 2015)	CLP, PC	ESS	LOLE,LOLD, LOLF,EENS	IEEE-RTS

(Rahmani andebili, 2015)	CLP, PC	UC	VOLL	synthetic systems
(Yousefi Ramandi et al., 2016)	ILs	RES	EENS	IEEE-RTS
(Moshari et al., 2016)	EDRPs	RES and LFU	LOLE,EENS	IEEE-RBTS
(Kopsidas and Kapetanaki, 2016)	=	DTR, RES	EENS, EFLC,EDLC	IEEE-RTS

From Table 2.2, it appears that researchers have adopted a certain basis for scientific research. For example, DLC programmes were frequently used in HL1 reliability assessment since the distribution systems and transmission liens are assumed fully reliable. Since EENS has the longest convergence time among the other reliability indices, it has been used widely in HL1 reliability assessment to determine the reliability performance in term of energy. It should also be noted that LOLE has been considerably used because this index reflects the inadequacy duration. In this regards, IEEE-RTS is extensively used to calculate the well-known reliability indices.

2.2 The Potential Benefits of ES

The potential benefits of ES are, Maintaining voltage stability, Relieving transmission congestion , Balancing energy resource, Mitigating the drawbacks posed by the intermittency of renewable energy sources, Increase the flexibility of electrical power system operation, Reinforce the integrated resource planning , Increase the utilisation of RES, Maintaining the reliability of electrical power systems and reducing the risk of being out of service, Avoiding the capital costs, Increase the system efficiency, Reducing the running costs, Enhancing power quality, security and power factor, Increase the customer satisfaction, Improving the market performance of electricity power systems, Mitigating the environmental damage.

Chapter Three

METHODOLOGY

3.1 Background

This section gives a data analysis and background of the IEEE-RTS, showing the assumptions in this study, energy supplied and unsupplied, priority order and capacity limits for each type of generation units.

Sequential MCS is performed due to chronological load model to calculate the reliability indices of the generation systems. MATLAB software is used in this thesis for system modeling and simulation. The sampling size is 3000 iterations in this study. As it was observed that all the simulations in this thesis converged at around the 2500th iteration, choosing 3000 iterations provided a conservative approach to ensure an adequate number of simulations has been performed to guarantee convergence. The hourly load profile and generation systems of the IEEE-RTS are adopted in this thesis (Allan et al., 1986, Subcommittee, 1979). The generation systems have 32 generators with a maximum capacity of 3405 MW that is serving 2850 MW of annual peak load. The generating system model of IEEE-RTS consists of 8736 load data points. IEEE-RTS data are shown in Appendix B. IEEE-RTS schematic diagram is shown in Figure 3.1.

Within a day, 1-16 hours are considered on-peak hours, while 17– 24 hours are considered off-peak hours. The probability of startup failure of peaking and cycling generation units is assumed to be 0.03 (Billinton, 2013). The maximum range of LFU

is considered 15% (Huang and Billinton, 2011). Each generation unit is of different type, capacity, size and failure rate. Therefore, each generation unit has its own unique operating requirements. Since the loading order of the generating units has a large impact on the system production costs, priority list method is used for minimising production cost (Billinton and Lakhanpal, 1996).

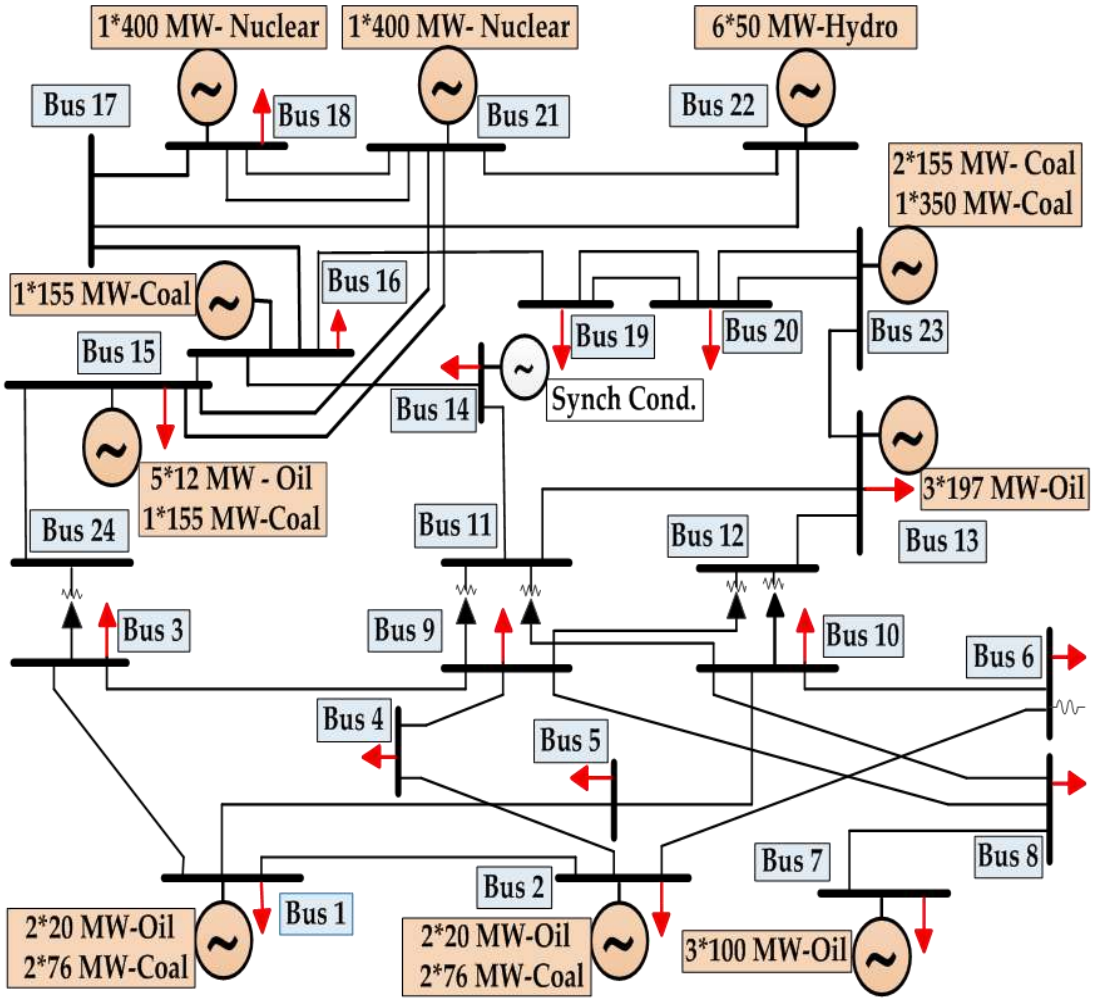

Figure 3.1 IEEE-RTS schematic diagram (Allan et al., 1986, Subcommittee, 1979)

Table 3.1 shows the priority order, capacity and the expected energy production of each generation unit type. Expected energy supplied (EES) by each type of generating unit is shown as well. As the priority order increases, the expected energy production of each generation unit decreases (Billinton and Lakhanpal, 1996, Allan et al., 1986).

According to the chronological load level, load types are divided into three; base load, cycling load and peaking load. Thus, generation units are consequently divided based on the type of supplied load. These types are; base, cycling and peaking generation units.

Table Base, peaking and cycling generation units' priority order (Billinton and Lakhanpal, 1996, Allan et al., 1986).

Priority order	Capacity (MW)	Unit type	EES (GWh)	Load supplied
1-6	50×6	Hydro	2594.592	Base
7-8	400×2	Nuclear	6142.754	
9	350×1	Coal	2521.737	
10-12	197×3	Oil	3002.401	
13-16	155×4	Coal	680.454	
17-19	100×3	Oil	333.287	Cycling
20-23	76×4	Coal	18.638	
24-28	12×5	Oil	1.149	Peaking
29-32	20×4	Oil	0.885	

3.2 Overview of Methodology

The proposed methodology is divided into three case studies. First Case involves generating systems adequacy assessment of the IEEE-RTS with PLS and CLS actions using two-state model. Second Case involves the comparison between hybrid model and two-state model as in Case one. Third Case includes the comparison of PLS and CLS on the HL1 assessment in presence of planned maintenance and LFU using hybrid model. The reliability indices that are used in Case one are LOLE, EENS, LOLF and

LOLD. The EENS is used in Cases two to three. Cases one to three are compared to show the impact of the proposed methodology as opposed to available methodologies in literature. It is worth mentioning that Case one gives a justification of using PLS and CLS in Case three while Case two gives a justification of using the hybrid model

The system risk model is acquired by combining the generation model with the load model. Then, risk indices are obtained such as LOLE, EENS, LOLF and LOLD. The analytical method and the simulation method are used to assess risk indices. In this thesis, sequential MCS is used to assess reliability indices. Sequential MCS simulates the actual process and the random behaviour of the generation systems in HLI assessment. The reliability indices are obtained by combining the load curve with the total available capacity of generation units and then to find power inadequacy in terms of energy, duration, frequency and duration per each interruption. Figure 3.2 shows the combination of the original load curve and the total available capacity of generation units.

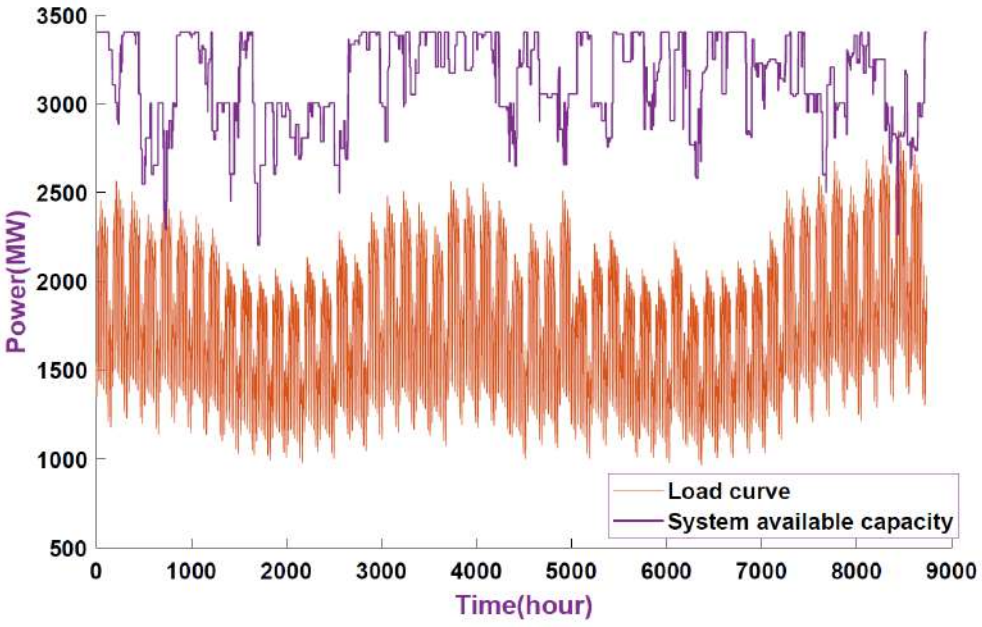

Figure 3.2 Combination of load with system available capacity (Li, 2013)

Figure 3.3 shows the flowchart of the methodology for assessing the adequacy of the generating system using two-state model with no load modification.

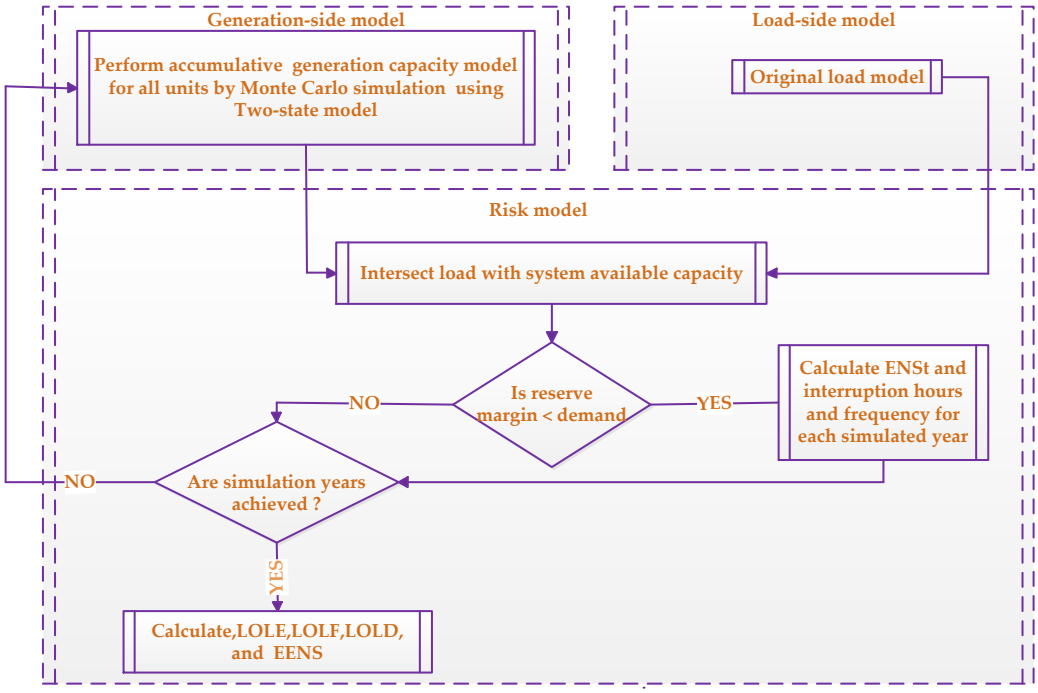

Figure 3.3 Flow chart of the previous study methodology (Li, 2013)

3.3 Generating Capacity Adequacy Model

This section briefly describes some of the well-known methodologies for generating capacity adequacy assessment to adequacy studies of power systems using DSM technique and an operating consideration. HLI reliability evaluation is the process of total generating systems adequacy assessment to meet the system demand requirement as shown in Figure 3.6 (Billinton, 2013, Li, 2013)

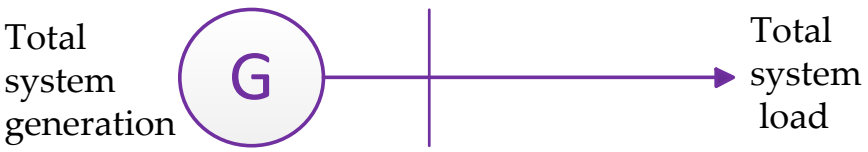

Figure 3. 4 System model for HLI adequacy evaluation (Billinton, 2013, Li, 2013).

The main objective of generating capacity adequacy evaluation is to assess the system reserve required to meet the system load. This evaluation is divided into two different aspects called static and operating adequacy evaluation. Static evaluation is the long-term planning requirement to meet the load. Operating capacity evaluation deals with short-term of the capacity requirement to meet the demand (Billinton, 2013, Li, 2013). This thesis deals with static aspects.

Generating capacity adequacy assessment involves the generation model, load model. The combination of these two models produces a risk model as shown in Figure 3.7

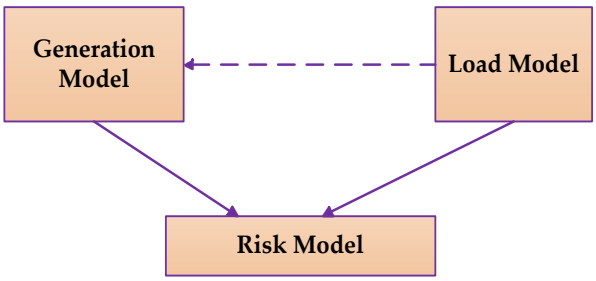

Figure 3.5 HLI assessment model (Billinton, 2013, Li, 2013).

3.3.1 Load Model

Load can be modelled in different ways to depict the demand throughout a specific period. Hourly load data can be modelled chronologically. A chronological load model is obtained from the available hourly data. The load $L(t)$ for hour t can be acquired by this equation (Billinton, 2013, Li, 2013):-

$$L(t) = L_w \times L_d \times L_h \tag{3.1}$$

Where L_w is the percentage of the weekly load in terms of the annual peak, L_d is the percentage of the daily load in terms of the weekly peak load and L_h is the percentage of the hourly load in terms of the daily peak. The annual hourly load model is obtained by acquiring 24-hour load profile, daily percentage, weekly percentage and the annual peak load. This load model is implemented in this thesis. Figure 3.8 shows the chronological hourly load model for the IEEE-RTS.

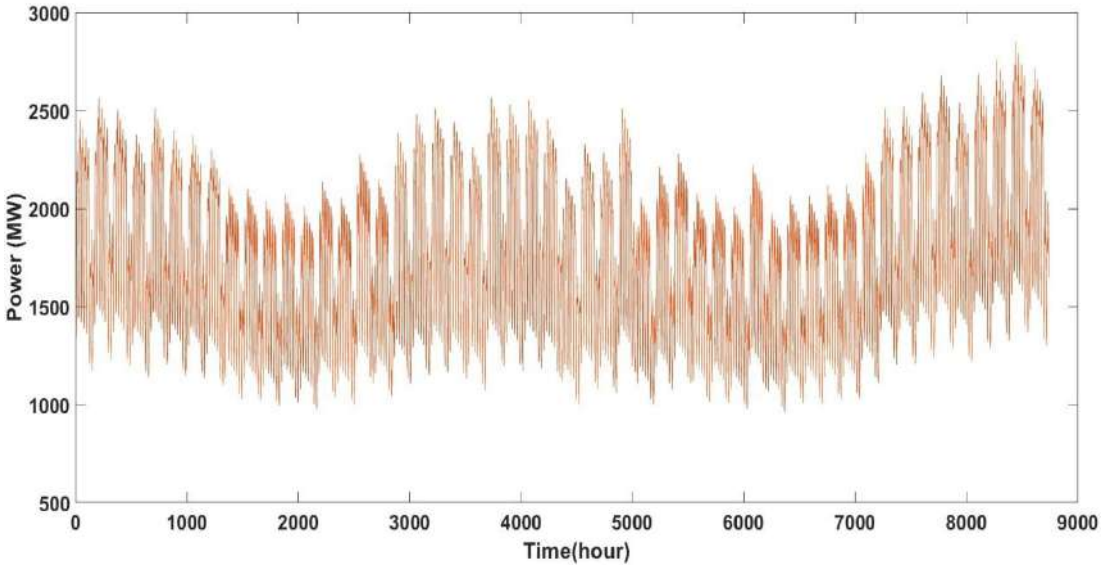

Figure 3.6 Chronological hourly load model for the IEEE-RTS (Billinton, 2013, Li, 2013).

3.3.2 Available Capacity of Generation Units Using Monte Carlo Simulation

The major focus of this thesis is to develop generating system adequacy assessment model for power systems incorporating load shifting technique. Generating system adequacy assessment can be achieved using either a probabilistic or a deterministic approach. Deterministic methods are gradually being changed by probabilistic methods due to their ability to reflect the actual risk of the corresponding systems. Probabilistic approach is used in this thesis by implementing sequential MCS

(Billinton, 2013, Li, 2013). Stochastic simulation includes a large number of time dependent random variables. However, this issue has been resolved with the improvements in digital computers.

MCS can be generally divided into two approaches, namely, non-sequential and sequential approaches (Billinton, 2013, Li, 2013). In non-sequential MCS, the system states are randomly simulated. In sequential MCS, the chronological behaviour of the system is sampled by simulating sequences of system states for several periods. Sequential MCS is used to estimate the risk indices by simulating the random behaviour of the generation units. The sequential MCS method is utilized in this thesis.

Risk model is formed by superimposing the chronological load model on total system available capacity. Operational history for each single generation unit is performed in the form of mean times to repair (MTTR) and generating unit mean times to failure (MTTF). These two parameters are taken as the reciprocal of the repair and failure rates, respectively as shown in Equations (2.3) and (3.3) (Billinton, 2013, Li, 2013).

$$MTTR = 1/\mu$$

$$MTTF = 1/\lambda$$

Random numbers, which are between 0 and 1, are used in conjunction with MTTR and MTTF to form a state history of each generator. State history of each generator consists of a series of random up-down-up or up-derated-down-up times. The state residence time for each generator is sampled according to a certain probability distribution. In this thesis, the relevant distributions are assumed to be exponential. Then, the random values of time-to-failure (TTF) and time-to-repair (TTR) are obtained from Equations (4.3) and (5.3) (Billinton, 2013, Li, 2013).

$$TTF = -MTTF In\ U$$

$$TTR = -MTTR\ In\ U$$

Where U is the uniformly distributed random number between [0,1], λ is the failure rate, and μ is the repair rate. The possible operating states of a generating unit are shown in Figure 3.10.

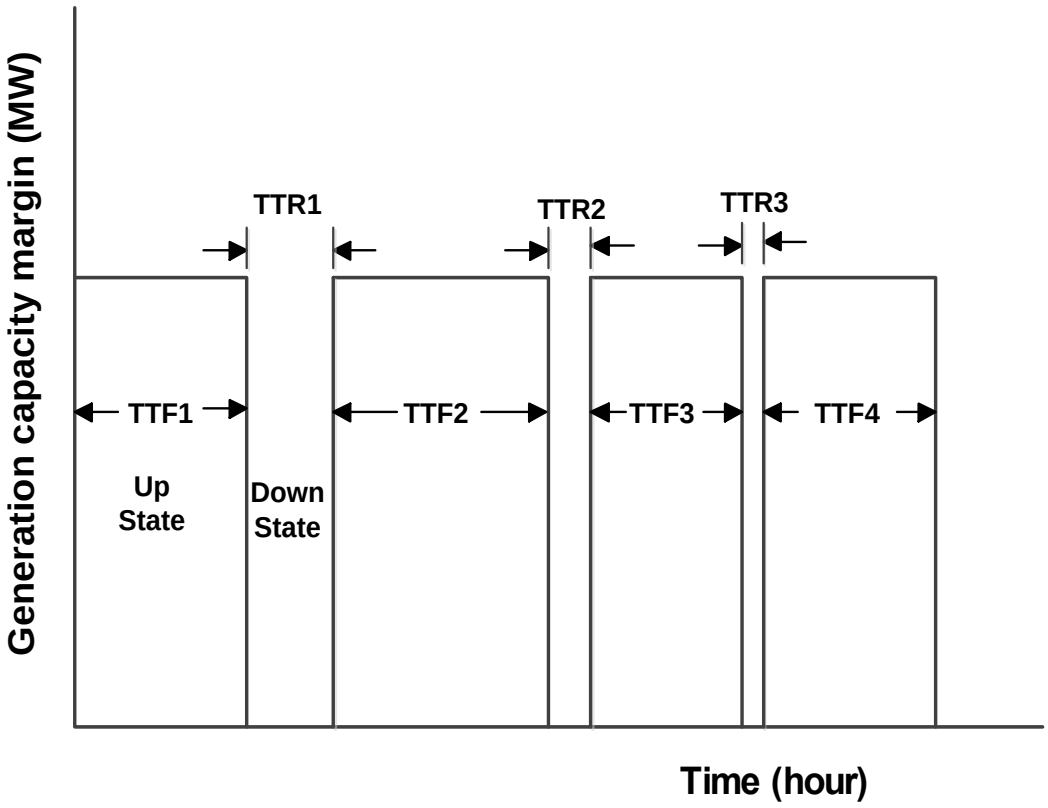

Figure 3.7 Possible operating cycle (TTF and TTR) of two-state model (Billinton, 2013, Li, 2013).

The process of assessing the total available capacity of all generation units can be briefly described as follows:

1. Simulate the available capacity for each generation unit by accumulating all operating history of available capacity for each generation units in the form of chronological up-derated-down-up or up-down-up operating cycles as shown in Figures 3.10 and 3.11.
2. Obtain the system available capacity for the simulated year by combining the operating cycles of all the generating units in the system. Figure 3.12 shows the total system available capacity for two units.

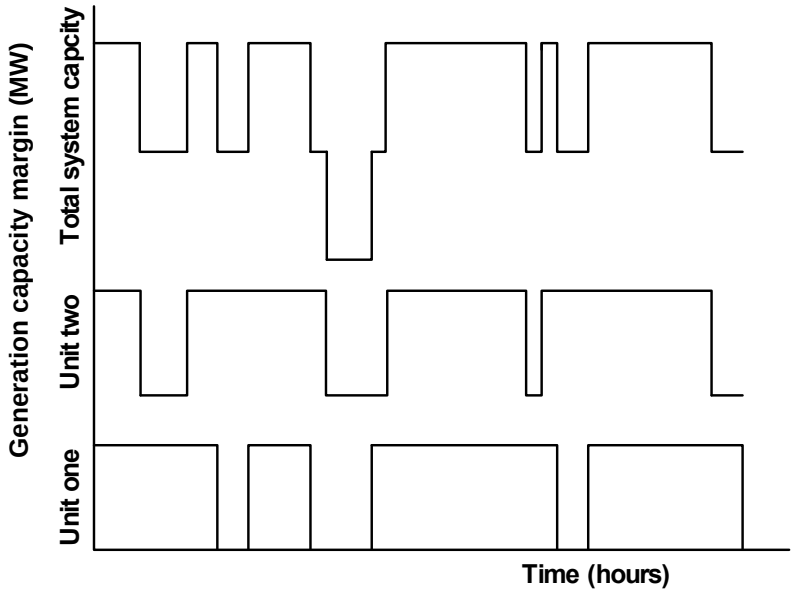

Figure 3.8 Available capacity of each unit (Billinton, 2013, Li, 2013).

3.3.3 Risk Model

The generation and load models are both superimposed to produce the risk model or the system available margin model. The superimposition of the available capacity on the load is shown in Figure 3.13.

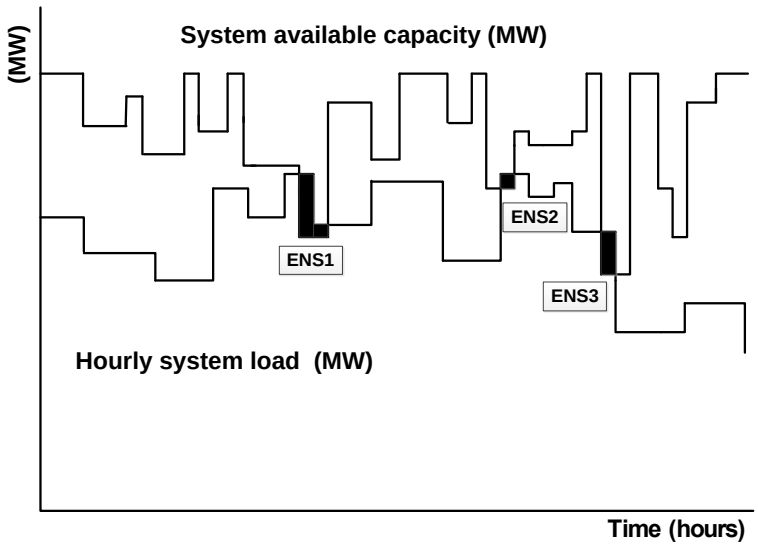

Figure 3.9 Superimposition of the system available capacity on the load (Billinton, 2013, Li, 2013)

A positive margin refers that the supplied energy is adequate to satisfy the system demand. A negative margin denotes that the system generation is insufficient and thus system demand has to be shed. The next step is to calculate appropriate reliability indices that can be used to describe the HLI reliability evaluation of the power system. EENS depicts the average amount of load loss due to generating inadequacy (Billinton, 2013).

In each sampled year, e.g. in year i, loss of load duration (LLD_i) in hours, the loss of load occurrence (LLO_i), and the energy not supplied (ENS_i) in MWh are obtained from the available margin model. The reliability indices in s sampling years therefore can be calculated using the following equations (Billinton, 2013, Li, 2013):

$$EENS = \frac{\sum_{i=1}^{s} ENS_i}{s} \qquad \text{(MWh/year)}$$

3.3.4 Two-state Model

Generation units are divided into three types; base load, cycling and peaking units. Base load units operate consistently to generate the electrical power needed to satisfy base load demand. These units are the most economical to operate and stop only for maintenance or unplanned outages. Peaking units operate only during high demand when load level surpasses the power supply of base load units. These units have a much higher production cost than base and cycling units. Due to this, the duty cycle of peaking units is shorter than duty cycle of base load units. In the two-state model, all generation units transit only between up and down states regardless of the types of generators, as shown in Figure 3.14. The transition rates between up and down conform to the common assumption that they are constant due to its underlying exponential distribution.

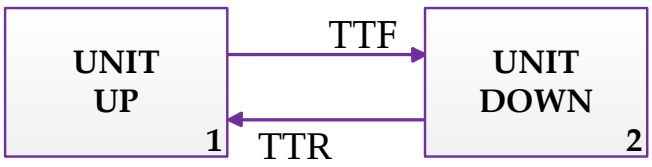

Figure 3.10 Two-state model for a base load unit (Billinton, 2013, Li, 2013).

3.4.5 Electric spring model

One of the electric spring application is energy storage system EES. For reliability evaluation, four parameters are usually used to characterize a battery energy storage unit. They are , storage capacity, charging/discharging rate (Rc/Rd), charging/discharging efficiency (Efc/ Efd), charging/discharging limit (Lc/Ld) (i.e.maximum/minimum capacity of energy storage) , The available energy remaining in the energy storage is the state of charge (SOC). Equation boundary conditions are :-

$$\mathrm{Ld} * \mathrm{tj} \leq \mathrm{AGsoc(j)} \leq \mathrm{Lc} * \mathrm{tj}$$

$$0 \leq \mathrm{Ecj} \leq \mathrm{Rc} * \mathrm{tj}$$

$$0 \leq \mathrm{Edj} \leq \mathrm{Rd} * \mathrm{tj}$$

$$\mathrm{AG} = \begin{cases} \mathrm{AGsoc\ (j-1)} + \mathrm{Efc} * \mathrm{ECj} & \text{charching} \\ \mathrm{AGsoc(j-1)} - 1/\mathrm{Efd} * \mathrm{EDj} & \text{discharching} \end{cases}$$ Where AGsoc(j) is the state of charge at time step j, AGsoc(j-1) is the state of charge at time step (j-1), tj is the duration of time step j, Ecj and Edj are the available energy for charging and required energy for discharging at time step j.

3.3.6 PV Model

The size and performance of PV systems strongly depend on meteorological variables such as solar energy, wind speed, and ambient temperature, and therefore, to optimize and control PV systems, accurate models must be developed in order to simulate system's performance. PV system models can be divided into two types of energy flow models and current-based models. Energy flow models are used for

system sizing, while current-based models are mainly use to demonstrate system control strategies . Modelling of stand-alone PV systems (SAPV) is very important in sizing system's energy sources. Figure 4.1 shows a typical PV system consisting of a PV module/ array, power conditioner such as charge controller or maximum power point tracking (MPPT) controller, batteries, inverter, and load. In general, a PV array collects energy form the sun and converts it to DC current. The DC current flows through a power conditioner to supply the load through an inverter. The daily output power produced by a PV module/array is given by

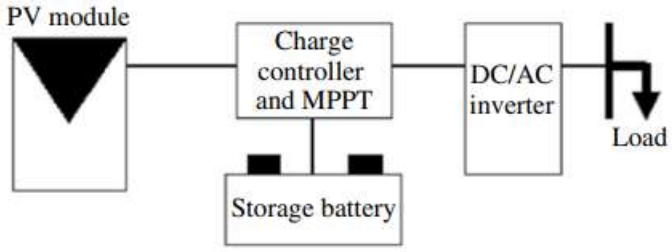

Figure Typical PV system components.

The calculation of energy produced by the PV array (E_{PV}) depends on the time step of the weather data used. In other words, if hourly input solar radiation data are given, then the power produced by the PV array,$P_{PV}(t)$, is equal to PV energy produc-tion, $E_{PV}(t)$. In contrast, if the input data are daily solar energy, the

$$E_{pv}(t) = P_{pv}(t)S$$

Where S is the day length that can be given by

$$s = \frac{2}{15}\cos^{-1}(-\tan L \tan \delta)$$

where L is the latitude and δ is the angle of declination. Figure 4.2 shows the flowchart for modeling an SAPV. The energy at the front end of an SAPV system or at the load side is given by

$$E_{net}(t) = \sum_{i=1}^{366} \left(E_{pv}(t) - E_L(t) \right)$$

where E_L is the load energy demand. The result of Equation 4.3 is either positive $\left(E_{pv} > E_L\right)$ or negative $\left(E_{pv} > E_L\right)$. If the energy difference is positive, then there is an excess in energy (EE), and if negative, then there will be an energy deficit (ED). The excess energy is stored in batteries in order to be used in times of ED. ED can be defined as the disability of the PV array to provide full power to the load at a specific time.

3.4 Solar Radiation Models:

Solar radiation models, such as the Perez model, are used to estimate the solar radiation components at a given location. These models take into account parameters like latitude, longitude, solar zenith angle, and atmospheric conditions to calculate the solar irradiance on a horizontal surface or using google maps to determine the longitude and latitude

3.4.1 Solar Energy Calculation:

Based on the solar radiation components obtained from the models, the solar energy incident on a horizontal surface can be estimated. The solar energy calculation considers the time period of interest, the tilt angle and orientation of the solar panels, shading effects, and system efficiency.

3.4.2 Data and Analysis:

Latitude and Longitude Selection:

A specific location is chosen based on latitude and longitude coordinates. These coordinates provide the geographical positioning necessary for accurate solar energy estimation.

(Al-iraqia university longitude and latitude on google maps)

3.4.3 Solar Radiation Data:

Solar radiation data for the selected location can be obtained from various sources, such as meteorological databases or satellite-based data repositories. The data should cover a sufficient time period to account for seasonal variations.

3.4.4 Solar Energy Estimation:

Using the solar radiation models and the obtained solar radiation data, the solar energy incident on a horizontal surface is calculated. MATLAB can be utilized to perform the necessary calculations efficiently

3.4.5 Results and Discussion:

The results obtained from the solar energy estimation provide insights into the solar energy potential of the specific location. The solar energy availability can be presented in the form of monthly or annual profiles, showcasing the variations throughout the year. These results can aid in assessing the feasibility of solar power projects, optimizing system design, and determining the economic viability of solar energy utilization.

3.4.6 Conclusion:

The determination of solar energy availability based on latitude and longitude coordinates provides a valuable tool for assessing the solar energy potential of a specific location. By using solar radiation models and calculations, accurate estimates of solar energy can be obtained. This information is crucial for decision-making processes related to solar power system design, deployment, and renewable energy integration.

3.5 Summary

The aforementioned flowcharts show that their algorithms have multiple models in load and generation-sides. All these algorithms can be summarised in the following steps:

Step 1: Specify the chronological hourly load curve.

Step 2: Model the original load without any modification.

Step 3: Calculate ENR which represents the total summation of the corresponding ENR_t.

Step 4: i=i+1

Step 5: Model the generation systems for the related static generation capacity by using the Two-state model.

Step 6: Generate the random statuses of each generator and obtain the total system available capacity by summing the generation capacity of each generator.

Step 7: Compare the generation capacity margin with the system demand. If the margin is greater, then Step 9 is executed; otherwise, go to Step 12.

Step 8: Acquire ENS_t .

Step 9: Check the number of simulations that has been performed. If the maximum number of simulations is not yet met, go to Step 5, otherwise proceed to Step 13.

Step 10: Calculate the total EENS

Step 11: If total static generation capacity is less than 3405, go to step 17.

Step 12: Calculate LOLE, EENS, LOLF and LOLD for Case study one.

Step 13: Remove one 20 MW units from static generation capacity based on priority list method and put instead PV with 20 MW then repeat the steps above.

Step 14: Calculate EENS for

Step 15: Case study two.

CHAPTER FOUR

RESULTS AND DISCUSSION

4.1 Introduction

This project focuses on electric spring and PV energy flow activities due to its wide implementation. Thus, an analysis and investigation are required to show the effect of PV and ES on HLI assessment comparing to original case. The following sections address the impact of PV and ES modelling techniques on HL1 assessment.

4.1.1 PV and ES Impacts on HL1 Adequacy Assessment

PV and ES are modelled to show the impact of each activity separately on generating systems adequacy indices. Multi scenarios are considered for each activity to show the changes in reliability indices compared with the varying of each activity scenario. The reliability indices that are used in this section is EENS only.

4.2 HL1 adequacy Assessment considering Case studies

This section is divided into three case studies. Case study 1 involves Hl1 assessment of the IEEE-RTS without any action. Case 2 involves the impact of PV model on the HL1 assessment. Case 3 includes the ES impact on the reliability of the generation systems

4.3 HL1 Assessment with PV and ES

Table shows the result of EENS for Case studies.

Table 4.1 EENS for Case study one

Case studies	Case study details	EENS(MWh/yr)
Case study 1	Base value	1197.4448
Case study 2	PV (12MW)	1627.0000
Case study 3	PV ((12*2)MW))	1601.0000
Case study 4	PV (12MW+ 20 MW)	2800.9000
Case study 5	PV ((12+ 20+76) MW)	17047.0000
Case study 6	PV ((12+ 20+76+100) MW)	74875.000
Case study 7	PV(12MW) +ES (Battery Bank 20 MW)	1325.8000
Case study 8	PV(24MW) +ES (Battery Bank 20 MW)	1061.7000

The EENS base value without PV action has been previously assessed (Li, 2013) . The effect PV on EENS is discussed as follows. When PV is not used, the EENS is 1197.4448 MWh/yr . After replacing G12 MW unit by PV 12MW EENS value is higher than base case. As much as PV replaced the EENS becomes worse. This highlights the reliability benefits of the ES measures. When ES is considered, there is

almost an improvement in EENS.When ES is considered, EENS value reduces significantly, improving the index values by 10%. This proves that ES has a significant impact on the reliability of generation systems. The reason for this significant improvement is that the ES program is used when the power supply is unable to meet the load demand. The results provide confirmatory evidence that EENS of base case are quite different from others study cases . As well, it is noted that the dynamic considerations of available system capacity have an important impact on the generating systems adequacy assessment thus must be accurately modelled.During the planning phase, the reliability of electrical power systems can be enhanced by increasing the adequacy of supply and this increases the initial costs. The corresponding cost might not be worth the enhancement of reliability. The balance between investment cost and (PV+ES) programmes can be achieved to find an optimal planning decision of reliability level.The results have shown that ES is clearly more effective than PV alone in terms of improving the reliability of power supply. In (PV+ES) model, optimal regulatory incentives can be determined by considering the efficiency, state of charge and availability of solar radiation. However, when the load level is higher than the available generation capacity, this amount of load should be under the direct control of the utilities. Hence, electricity suppliers are allowed during adequacy deficiency to shed the load and then cycle partially or totally the curtailed energy per each interruption. In-need period significantly affects the EENS since peaking and cycling load units have less operating hours and more shutdowns and startups actions than base load units do. This is due to less the needed period is, the less failure probability of units. As well, startups of peaking units are only required when they are in need. Since peaking units, during the duty cycle, have less actual failure probability than base load units, they operate more reliably than base load units

do. According to the priority order, the peaking and cycling load units have lower loading while base load units have higher loading. That is why , the (PV+ES) model can be used as peaking units.

4.4 HL1 Adequacy Assessment with PV+ES as Alternatives to Peaking Units using Hybrid Model

The impact of (PV+ES) as alternatives to peaking units in terms of adequacy using is investigated in this section. Throughout the year, the total energy capacity for each generation unit in IEEE-RTS cannot be totally supplied. This is because of outages, planned maintenance and reserve margin operation requirement. The remaining energy, therefore, is the EES. In a yearly base, Figure shows the EES for each generation units as well as the ENS due to planned and unplanned outage and remain energy represents the available energy for reserve margin requirement.

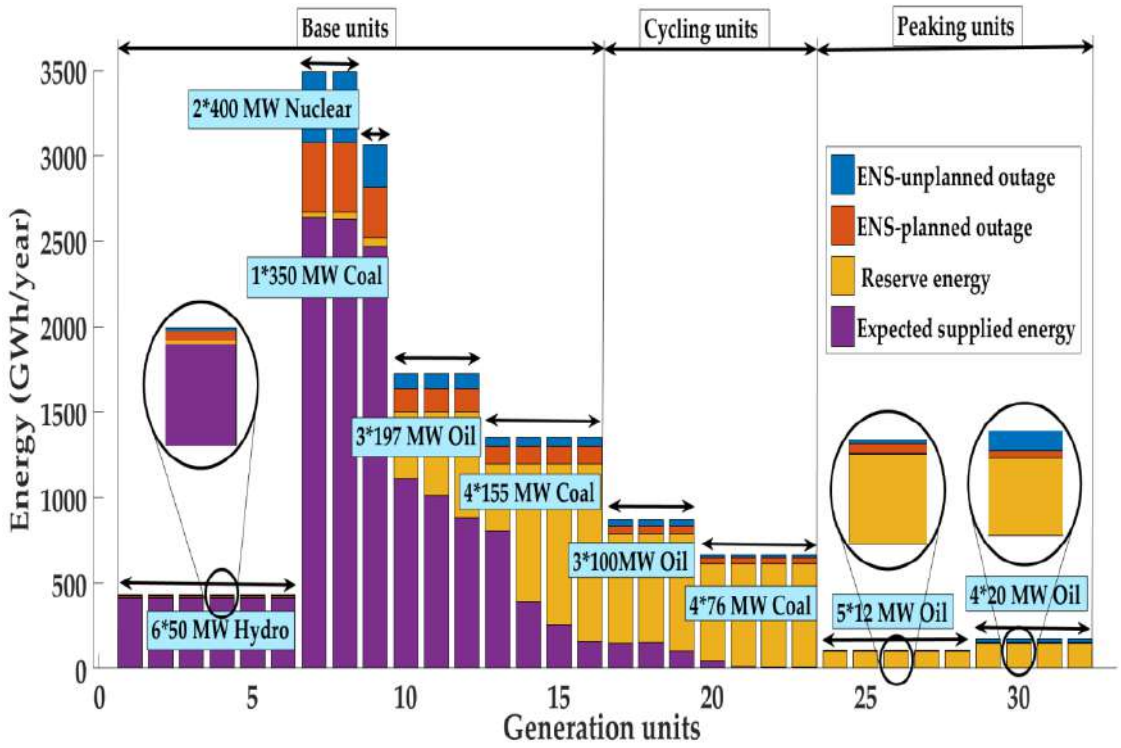

Figure EES and ENS of IEEE-RTS generation units

In this figure, each bar represents the total energy capacity for the all generation units throughout the year. First top part of each bar represents the ENS due to unplanned outage which depends on the failure rate of the corresponding unit. The second part is ENS due to planned outage which depends on the period of maintenance for the corresponding unit. Third part represents the available reserve energy, which is not consumed because of spinning reserve requirement. The last part of the bar is the EES. These distributions will provide a significant indicator to make a balance among all generation units if proper load shifting scheme is implemented. It is worth mentioning that the most economic units must be in the duty more than the less economic units to guarantee an optimal and efficient operation of generation plant. To achieve that, an optimal balance among all generation units must be committed.

The utility has to generate energy more than demand requires in the aim of keeping system secure during the outages and sudden increase in demand. The available capacity above the load curve is called reserve capacity.

4.5 Conclusion

HL1 adequacy assessment is an essential area of power system reliability. It is used extensively in power system planning and operation phases. PV+ES is the main contributor to energy management . It influences the energy consumed and significantly improves cost and reliability. During generating system adequacy deficiency, most of the energy curtailed can be recovered in the same day; however, a certain amount of energy cannot be recovered due to the stochastic nature of failures that might be extended to the recovery period time. Although recovery time is usually on off-peak period, the capacity of energy must be recovered during the hours of the day might exceed the available generation capacity. This amount of energy is called

EENR. PV+ES programmers are classified in this study as corrective action , it is implemented after fault occurrence, and the preventive load-shifting programme is implemented when the system is under increased risk and this programme type can be implemented to ensure the optimal level of reliability. The major limitations of PV+ES implementation are the highly initial cost and RES uncertainty. Power systems usually have reserve capacity margin to account for load uncertainty and generator outages as well as planned maintenance. The PV+ES programme proposed in this project improves the adequacy of the power supply without introducing additional classical power generating facility thus PV+ES is a viable alternative that is much faster to be implemented. Thus, the PV+ES is clearly more effective than classical generating units in terms of improving the reliability of power supply.

REFERENC

AGHAJANI, G., SHAYANFAR, H. & SHAYEGHI, H. 2017. Demand side management in a smart micro-grid in the presence of renewable generation and demand response. *Energy,* 126**,** 622-637.

AHSAN, Q. 1990. Load management: impacts on the reliability and production costs of interconnected systems. *International Journal of Electrical Power & Energy Systems,* 12**,** 257-262.

AIOWAIFEER, M., ALMUHAINI, M. & ALSAGGAF, A. The impact of load management and renewable DG on the service restoration of future power distribution systems. Environment and Electrical Engineering (EEEIC), 2015 IEEE 15th International Conference on, 2015. IEEE, 1789-1794.

ALLAN, R. N., BILLINTON, R. & ABDEL-GAWAD, N. 1986. The IEEE reliability test system-extensions to and evaluation of the generating system. *IEEE Transactions on Power Systems. (86WM 0384); T-PWRSNov86 1-7.*

BILLINTON, R. & LAKHANPAL, D. 1996. Impacts of demand-side management on reliability cost/reliability worth analysis. *IEE Proceedings - Generation, Transmission and Distribution,* 143**,** 225-231.

BILLINTON, R. A., R.N. 2013. *Reliability evaluation of power systems,* Plenum: New York, NY, USA, 1984.

BROEER, T., TUFFNER, F. K., FRANCA, A. & DJILALI, N. 2018. A demand response system for wind power integration: greenhouse gas mitigation and

reduction of generator cycling. *CSEE Journal of Power and Energy Systems,* 4**,** 121-129.

DARVISH, H., DARVISHI, A. & HEJAZI, H. Integration of demand side management in security constrained energy and reserve market. Innovative Smart Grid Technologies Conference (ISGT), 2015 IEEE Power & Energy Society, 2015. IEEE, 1-5.

DEHNAVI, E. & ABDI, H. 2017. Determining optimal buses for implementing demand response as an effective congestion management method. *IEEE Transactions on Power Systems,* 32**,** 1537-1544.

FARMAD, H. S. & BIGLAR, S. 2012. Integration of demand side management, distributed generation, renewable energy sources and energy storages.

FREEMAN, R. 2005. Managing energy: Reducing peak load and managing risk with demand response and demand side management. *Refocus,* 6**,** 53-55.

GELLINGS, C. W. & SMITH, W. M. 1989. Integrating demand-side management into utility planning. *Proceedings of the IEEE,* 77**,** 908-918.

HU, Z., HAN, X. & WEN, Q. 2013. *Integrated resource strategic planning and power demand-side management,* Springer.

HUANG, D. & BILLINTON, R. Impacts of demand side management on bulk system reliability evaluation considering load forecast uncertainty. 2011 IEEE Electrical Power and Energy Conference, 3-5 Oct. 2011 2011. 272-277.

JOUNG, M. & KIM, J. 2013. Assessing demand response and smart metering impacts on long-term electricity market prices and system reliability. *Applied Energy,* 101**,** 441-448.

KANDASAMY, N. K., TSENG, K. J. & SOONG, B. 2017. A Virtual Storage Capacity Using Demand Response Management to Overcome Intermittency of Solar PV Generation. *IET Renewable Power Generation*.

KARUNANITHI, K., SARAVANAN, S., PRABAKAR, B., KANNAN, S. & THANGARAJ, C. 2017. Integration of Demand and Supply Side Management strategies in Generation Expansion Planning. *Renewable and Sustainable Energy Reviews,* 73**,** 966-982.

KOPSIDAS, K. & KAPETANAKI, A. 2016. Optimal Demand Response Scheduling with Real Time Thermal Ratings of Overhead Lines for Improved Network Reliability. *IEEE Transactions on Smart Grid*.

LI, W. 2013. *Reliability assessment of electric power systems using Monte Carlo methods*, Springer Science & Business Media.

MARTÍNEZ-LAO, J., MONTOYA, F. G., MONTOYA, M. G. & MANZANO-AGUGLIARO, F. 2017. Electric vehicles in Spain: An overview of charging systems. *Renewable and Sustainable Energy Reviews,* 77**,** 970-983.

MOSHARI, A., EBRAHIMI, A. & FOTUHI-FIRUZABAD, M. 2016. Short-term impacts of DR programs on reliability of wind integrated power systems considering demand-side uncertainties. *IEEE Transactions on Power Systems,* 31**,** 2481-2490.

MOURA, P. S. & DE ALMEIDA, A. T. 2010. The role of demand-side management in the grid integration of wind power. *Applied Energy,* 87**,** 2581-2588.

RAHMANI ANDEBILI, M. 2015. Risk and cost based generation scheduling smartly mixed with reliability driven and market driven demand response measures. *International Transactions on Electrical Energy Systems,* 25**,** 994-1007.

SAINI, S. 2004. Conservation v. generation: The significance of Demand-Side Management (DSM), its tools and techniques. *Refocus,* 5**,** 52-54.

SONI, J. & PANDA, S. K. 2017. Electric Spring for Voltage and Power Stability and Power Factor Correction. *IEEE Transactions on Industry Applications,* PP**,** 1-1.

SUBCOMMITTEE, P. M. 1979. IEEE Reliability Test System *IEEE Transactions on Power Apparatus and Systems,* pp. 2047-2054,.

TEH, J. 2018. Adequacy Assessment of Wind Integrated Generating Systems Incorporating Demand Response and Battery Energy Storage System. *Energies,* 11**,** 2649.

WIMMLER, C., HEJAZI, G., DE OLIVEIRA FERNANDES, E., MOREIRA, C. & CONNORS, S. 2017. Impacts of Load Shifting on Renewable Energy Integration. *Energy Procedia,* 107**,** 248-252.

YOUSEFI RAMANDI, M., AFSHAR, K., SHOKRI GAZAFROUDI, A. & BIGDELI, N. 2016. Reliability and economic evaluation of demand side management programming in wind integrated power systems. *International Journal of Electrical Power & Energy Systems,* 78**,** 258-268.

ZHOU, Y., MANCARELLA, P. & MUTALE, J. 2015. Modelling and assessment of the contribution of demand response and electrical energy storage to adequacy of supply. *Sustainable Energy, Grids and Networks,* 3**,** 12-23.

ZONG, Y., KULLMANN, D., THAVLOV, A., GEHRKE, O. & BINDNER, H. W. 2012. Application of model predictive control for active load management in a distributed power system with high wind penetration. *IEEE Transactions on Smart Grid,* 3**,** 1055-1062.

APPENDICES

APPENDIX A: Graphs

APPENDIX A: POWER SYSTEMS RELIABILITY INDICES

Table A. 1 Power systems reliability indices

<table>
<tr><td>Indices</td><td colspan="3">Details</td></tr>
<tr><td rowspan="5">HLI</td><td>Loss of Load</td><td colspan="2">Loss Of Load Expectation LOLE (days/yr or hr/yr)</td></tr>
<tr><td rowspan="4">Loss of Energy</td><td colspan="2">Loss Of Load Frequency LOLF (occ. / yr)</td></tr>
<tr><td colspan="2">Loss Of Load Duration LOLD (hr/disturbance)</td></tr>
<tr><td colspan="2">The Energy Index of Reliability EIR</td></tr>
<tr><td colspan="2">Loss of Energy Expectation, LOEE (MWh /yr)</td></tr>
<tr><td rowspan="15">HLII</td><td rowspan="15">Annualized load point</td><td rowspan="9">Basic values</td><td>Probability of failure (PLC-Probability of Load Curtailments)</td></tr>
<tr><td>Expected frequency of failure (EFF)</td></tr>
<tr><td>Expected Frequency of Load Curtailments (EFLC-occ. /yr)</td></tr>
<tr><td>Expected number of voltage violations</td></tr>
<tr><td>Expected number of load curtailments(ENLC)</td></tr>
<tr><td>Expected load curtailed (ELC-MW /yr)</td></tr>
<tr><td>Expected energy not supplied (EENS-MWh/yr)</td></tr>
<tr><td>Expected duration of load curtailments (EDLC-hr/yr)</td></tr>
<tr><td rowspan="3">Maximum values</td><td>Maximum energy curtailed</td></tr>
<tr><td>Maximum load curtailed</td></tr>
<tr><td>Maximum duration of load curtailment</td></tr>
<tr><td rowspan="3">Average values</td><td>Average energy not supplied</td></tr>
<tr><td>Average load curtailed</td></tr>
<tr><td>Average Duration of Load Curtailment (ADLC-hr/disturbance)</td></tr>
</table>

Table A.1 Continued

Indices	Details		
HLII	Annualized load point	Bus isolation values	Expected load curtailed
			Expected number of curtailments
			Expected energy not supplied (EENS-MWh/Yr)
			Expected duration of load curtailment
			Bulk power interruption index (BPII- MW /MW-yr)
	Annualized system	Basic values	Bulk Power-Supply Average MW Curtailment Index (BPACI-MW /disturbance)
			Bulk Power/Energy Curtailment Index (BPECI-MWh/MW-yr)
			Modified Bulk Power Curtailment Index (MBPCI- MW /MW)
		Average values	Average number of curtailments/load point
			Average load curtailed/load point
			Average energy curtailed/load point
			Average duration of load curtailed/load point
			Average number of voltage violations/load point
		Maximum values	Maximum system load curtailed under any contingency condition
Reliability Worth	EIC Expected Interruption Cost (k$/ yr)		
	lEAR Interrupted Energy Assessment Rate ($/ kWh)		
	VOLL: Value of Lost Load		

APPENDIX B: IEEE 24-BUS RELIABILITY TEST SYSTEM DATA

In this appendix, the data of the IEEE 24-bus reliability test system (RTS) used in this study are given.

Table B.1 Generator Reliability Data

Unit Group	Unit Size (MW)	Unit Type	FOR	MTTF(Hour)	MTTR(Hour)
U12	12	Oil/Steam	0.02	2940	60
U20	20	Oil/CT	0.10	450	50
U50	50	Hydro	0.01	1980	20
U76	76	Coal/Steam	0.02	1960	40
U100	100	Oil/Steam	0.04	1200	50
U155	155	Coal/Steam	0.04	960	40
U197	197	Oil/Steam	0.05	950	50
U350	350	Coal/Steam	0.08	1150	100
U400	400	Nuclear	0.12	1100	150

Table B.2 Daily load in Percentage of Weekly Peak

Day	Peak Load
Monday	93
Tuesday	100
Wednesday	98
Thursday	96
Friday	94
Saturday	77

Sunday	75

Table B.3 Weekly peak load as a percentage of annual peak

Week	Peak Load	Week	Peak Load
1	86.2	27	75.5
2	90.0	28	81.6
3	87.8	29	80.1
4	83.4	30	88.0
5	88.0	31	72.2
6	84.1	32	77.6
7	83.2	33	80.0
8	80.6	34	72.9
9	74.0	35	72.6
10	73.7	36	70.5
11	71.5	37	78.0
12	72.7	38	69.5
13	70.4	39	72.4
14	75.0	40	72.4
15	72.1	41	74.3
16	80.0	42	74.4
17	75.4	43	80.0
18	83.7	44	88.1
19	87.0	45	88.5

20	88.0	46	90.9
21	85.6	47	94.0
22	81.1	48	89.0
23	90.0	49	94.2
24	88.7	50	97.0
25	89.6	51	100.0
26	86.1	52	95.2

Table B.4 Hourly peak load in percent of daily peak

Hour	winter weeks		summer weeks		spring/fall weeks	
	1 -8 & 44 - 52		18 -30		9-17 & 31 - 43	
	Wkdy	Wknd	Wkdy	Wknd	Wkdy	Wknd
12-1 am	67	78	64	74	63	75
1-2	63	72	60	70	62	73
2-3	60	68	58	66	60	69
3-4	59	66	56	65	58	66
4-5	59	64	56	64	59	65
5-6	60	65	58	62	65	65
6-7	74	66	64	62	72	68
7-8	86	70	76	66	85	74

8-9	95	80	87	81	95	83
9-10	96	88	95	86	99	89
10-11	96	90	99	91	100	92
11-noon	95	91	100	93	99	94
Noon-1pm	95	90	99	93	93	91
1-2	95	88	100	92	92	90
2-3	93	87	100	91	90	90
3-4	94	87	97	91	88	86
4-5	99	91	96	92	90	85
5-6	100	100	96	94	92	88
6-7	100	99	93	95	96	92
7-8	96	97	92	95	98	100
8-9	91	94	92	100	96	97
9-10	83	92	93	93	90	95
10-11	73	87	87	88	80	90
11-12	63	81	72	80	70	85

Where Wkdy = Weekday, wknd Weekend

Table B.5 Hydro Capacity and Energy

Quarter	Capacity Available % (1)	Energy Distribution% (2)
1	100	35
2	100	35
3	90	10

4	90	20
Note:(1) 100% capacity = 50 MW, (2) 100% energy = 200 GWh		

Table B.6 Unit Derating Data for the IEEE RTS

Unit Derated (MW)	size capacity (MW)	Mean duration (hr)		
		Up	Derated	Down
350	175	1150	60	70
400	200	1100	100	100